AN ABSTRACT OF THE THESIS OF

David Hsien-Yu Lei for the degree of Doctor of Philosophy in Mechanical Engineering presented on January 8, 1988.

Title: An Experimental Study of Radiative and Total Heat Transfer Between a High Temperature Fluidized Bed and an Array of Immersed Tubes

Abstract approved: Redacted for privacy

James R. Welty

Experimental data are reported for the time-averaged local radiative and total heat transfer coefficients for both an array of horizontal tubes as well as a single horizontal tube immersed in a large-particle fluidized bed at elevated temperatures. Spatial-averaged heat transfer coefficients computed from the local values, using a simple trapezoidal rule integration, are reported.

An instrumented tube was used to measure both the radiative and total heat transfer rates simultaneously. Three different window materials, silicon, sapphire, and quartz, have been tested in order to examine some key design decisions made in the development of the radiation detector. It is concluded that the radiation detector employing silicon as the window material is most suitable to achieve accurate measurements of the radiative heat transfer between a fluidized bed and immersed surfaces.

Experiments were conducted at the Oregon State University high temperature fluidized bed facility employing

ione grain as the bed material. Measurements were made for two particle sizes (2.14 mm and 3.23 mm) and at three different bed temperatures (812 K, 925 K, and 1000 K).

The radiative heat transfer results for tube arrays are believed to be the first of their kind. In comparing these results with those for a single tube, it was found that the radiative heat transfer coefficient decreases with increases in both bed temperature and particle size due to the presence of neighboring "cool" tubes in a hot bed and the greater "see through" effect of the larger particles. Radiation contributions for a bubbling bed were calculated for various test conditions.

The effects of superficial velocity, bed temperature, particle size, and adjacent "cool" tubes on both the radiative and total heat transfer performance are described with comparisons made between the results of this study and available literature data or correlations.

An Experimental Study of Radiative and Total Heat Transfer Between a High Temperature Fluidized Bed and an Array of Immersed Tubes

by

David Hsien-Yu Lei

A THESIS

submitted to

Oregon State University

in partial fulfillment of
the requirements for the
Degree of

Doctor of Philosophy

Completed January 8,1988

Commencement June 1988

APPROVED:

Redacted for privacy

Professor of Mechanical Engineering in Charge of Major

Redacted for privacy

Head of Department of Mechanical Engineering

Redacted for privacy

Dean of Graduate School

Date thesis is presented January 8, 1988

Typed by David Hsien-Yu Lei

ACKNOWLEDGMENTS

I would like to express my grateful appreciation to Dr. James R. Welty, my major professor, who provided direction for my research and financial support during the course of my graduate studies at Oregon Stat University. His ingenuity was essential for the sucess of whole fluidized bed project, and this thesis as well. Working with him has been a pleasant and unforgettable experience.

My thanks also go to Dr. Adams for his valuable advise and suggestions on this project. It was a good feeling to know that there was someone who know answers to all your confusions. Dr. Sollitt, Dr. Guenther, and Dr. Davis, are appreciated for their reading and commenting on my thesis.

Many thanks are due to Dr. Nasser Alavizadeh and Ali Goshayeshi for their assistance and helpful hands in many occasions. I wish to express my thanks to Bea Bjornstad who was always there to help me in so many ways.

Finally, I come to my family. My greatest appreciation goes to my wife Vera for her patience, encouragement, and consideration. She has done such a good job to our precious little Oliver to whom I owe so much for not being a devoted father in the first few months of his life. This thesis is dedicated to my parents for their love and support. They have done more than their share. I love you, Mom and Dad.

TABLE OF CONTENTS

Chapter — Page

Chapter **Page**

LIST OF FIGURES

LIST OF TABLES

Table **Page**

NOTATION

Symbol	Description	Units
Ar	Archimedes number $\left[= \frac{gD_p^3(\rho_p-\rho_f)\rho_f}{\mu_f^2}\right]$	
C_c	Calibration constant of heat flux sensor [= $F(T_s)/C_s$]	$W/m^2 \cdot \mu V$
C_s	Heat flux sensor sensitivity constant [Eqn. (A.2)]	$\mu V.m^2/W$
c_{pf}	Gas specific heat at constant pressure	kJ/kg.K
c_{ps}	Particle specific heat at constant pressure [Table 3.1]	kJ/kg.K
D_o	Tube outside diameter	mm
D_p	Mean particle diameter	mm
D_{pj}	Mean diameter in particle size interval j [Eqn. (3.4)]	mm
e_{mf}	Heat flux sensor output voltage	μV
$F(T_s)$	Heat flux sensor multiplication factor [Eqn. (A.2)]	
f	Radiation contribution [= Q_{rb}/Q_t]	%
f_{ave}	Average radiation contribution at bubbly bed stage	%
f_o	Bubble contact fraction	
$1-f_o$	Emulsion contact fraction	
g	Gravity acceleration	m/s^2
Gr	Grashof number [= $gH^3\beta\Delta T\rho_f^2/\mu_f^2$]	
H	Cavity height	m
h	Heat transfer coefficient	$W/m^2.K$
h_b	Gas convective heat transfer coefficient in bubble phase	$W/m^2.K$
h_{gc}	Gas convective heat transfer coefficient in emulsion phase	$W/m^2.K$

Symbol	Description	Units
h_{mf}	Gas convective heat transfer coefficient at minimum fluidization	$W/m^2.K$
h_{max}	Maximum heat transfer coefficient	$W/m^2 \cdot K$
h_{pc}	Particle convective heat transfer coefficient in emulsion phase	$W/m^2.K$
h_r	Radiative heat transfer coefficient in emulsion and bubble phases	$W/m^2.K$
h_{rb}	Black tube local radiative heat transfer coefficient	$W/m^2.K$
h_t	Local total heat transfer coefficient	$W/m^2.K$
$h_{\alpha max}$	Maximum local total heat transfer coefficient	$W/m^2 \cdot K$
$\bar{h}$	Spatial-averaged heat transfer coefficient	$W/m^2.K$
$\bar{h}_{rb}$	Spatial-averaged black tube radiative heat transfer coefficient	$W/m^2.K$
$\bar{h}_t$	Spatial-averaged total heat transfer coefficient	$W/m^2.K$
$\bar{h}_{max}$	Spatial-averaged maximum total heat transfer coefficient	$W/m^2.K$
k	Thermal conductivity	W/m.K
k_f	Gas thermal conductivity	W/m.K
k_p	Particle thermal conductivity	W/m.K
M	Number of particle size intervals	
MF	Magnification factor of lens	
N	Number of data recorded	
Nu_p	Particle Nusselt number [= hD_p/k_f]	
$Nu_{p,mf}$	Particle Nusselt number at minimum fluidization [= $h_{mf}D_p/k_f$]	
$Nu_{t,b}$	Nusselt number in bubble phase based on tube diameter [= hD_o/k_f]	

Symbol	Description	Units
$\overline{Nu}_{max}$	Spatial-averaged maximum particle Nusselt number [= $\bar{h}_{max}D_p/k_f$]	
Pr	Prandtl number [= $\mu_f c_{pf}/k_f$]	
Q	Heat flux	W/m^2
Q_d	Detected heat flux	W/m^2
Q_{rb}	Black tube radiative heat flux	W/m^2
$Q_{rb,si}$	Black tube radiative heat flux employing silicon window	W/m^2
$Q_{rb,sa}$	Black tube radiative heat flux employing sapphire window	W/m^2
$Q_{rb,qz}$	Black tube radiative heat flux employing quartz window	W/m^2
Q_t	Total heat flux	W/m^2
$\bar{Q}_{rb}$	Spatial-averaged black tube radiative heat flux	W/m^2
$\bar{Q}_t$	Spatial-averaged total heat flux	W/m^2
Re_p	Particle Reynolds number [= $\rho_f U_o D_p/\mu_f$]	
Re_{tmf}	Reynolds number based on tub diameter and minimum fluidization [= $\rho_f U_{mf} D_o/\mu_f$]	
T_f	Bed temperature	K
T_{fi}	Film temperature [= $(T_f+T_{wi})/2$]	K
T_s	Heat flux sensor temperature	K
T_w	Tube wall temperature	K
T_{wi}	Average window temperature	K
U_{mf}	Minimum fluidization velocity	m/s
U_o	Gas superficial velocity	m/s
U_{op}	Optimum superficial velocity	m/s
V_d	Detected thermopile voltage	μV
V_{ref}	Thermopile reference voltage	V

Symbol	Description	Units
V_t	Thermocouple voltage	V
Y	Horizontal tube spacing	cm
Z	Vertical tube spacing	cm

Greek	Description	Units
α	Angle measured from lower stagnation point	Degrees
β	Coefficient of thermal expansion	1/K
δ	Bubble phase volume fraction	
$1-\delta$	Emulsion phase volume fraction	
ϵ_{ef}	Effective bed emissivity	
ϵ_p	Particle emissivity	
ϵ_w	Tube wall emissivity	
μ_f	Gas viscosity	kg/m.s
σ	Stefan-Boltzmann constant	W/m^2
ρ_f	Gas density	kg/m^3
ρ_p	Particle density	kg/m^3
Δ	Maximum value of uncertainty [Eqn. (B.2)]	

Subscripts

i	Heat flux and temperature index [Eqn. (3.5)]
j	Particle size interval index [Eqn. (3.4)]
1,2,3	Radiative detector index number
4,5,6	Total heat flux gauge index number
sa	Sapphire
si	Silicon
qz	Quartz

AN EXPERIMENTAL STUDY OF RADIATIVE AND TOTAL HEAT TRANSFER BETWEEN A HIGH TEMPERATURE FLUIDIZED BED AND AN ARRAY OF IMMERSED TUBES

I. INTRODUCTION

1.1 Background

Gas-solid fluidized bed technology has been used in various industrial processes since the first major large-scale commercial application in catalytic cracking process in 1942 (99,30). Most applications of this technique take advantage of its unusual characteristics, which include ease of handling of fluid-like solids, extremely large areas of contact between solid and fluid, nearly isothermal conditions throughout the bed, and high rates of heat transfer between the bed and immersed surfaces. In the latter case, there is considerable interest in fluidized bed combustion of high sulfur coal, wood chips, biomass, or industrial waste in the field of energy utilization. Other applications of fluidized bed heat transfer include heating of process fluids such as crude oil (49), combustion of radiative waste (145), metallurgical heat treatment, and hydrocarbon processing (30).

The most effective application of coal, which comprises over 80% of the earth's energy resource, is direct burning (124). Unfortunately, coal usually contains substantial amounts of sulfur and nitrogen compounds which are released in the exhaust gas as SO_x and NO_x during the course of combustion. Thus, the development of coal combustion

techniques should be concerned with minimizing these air pollution problems. A principal motivation for the interest in fluidized bed combustion is thus associated with the concept that the combustion of coal in fluidized beds will allow the adsorption of SO_x.

The advantages of fluidized bed combustors over conventional boilers are three-fold. First, the SO_2 produced during the combustion process is retained in the furnace by using bed materials such as limestone or dolomite. Thus, high sulfur coal can be utilized and the corrosion of the boiler system is also minimized (122). Secondly, the lower operating temperatures (T_f = 800-1000 ^oC) in a fluidized bed boiler, comparing with conventional ones (T_f > 1400 ^oC), reduce the emissions of NO_x so that low rank fuel such as oil shale or high ash coal can be used (95,100,124). Thirdly, and probably more important as far as design and thermal efficiencies are concerned, heat transfer rates between a gas-solid fluidized bed and immersed surfaces can be up to 20 times higher than with single phase flow (108). This suggests that fluidized bed combustion has particular appeal with its combined advantages of pollution control, fuel flexibility, and excellent heat transfer characteristics. It provides not only an optimum economic combustor system, but also essential features which are required for emission control (122).

The design aspects of different commercial or pilot-scale fluidized bed combustion systems can be found in Basu

(21,22), Howard (88), Goblirsch, et al. (73), and Leon, et al. (101). For a typical fluidized bed combustor, coal, which comprises about 1% to 2% of the bed material, is burned in the bed (40,116). The heat is transferred to in-bed tube arrays, and steam generated in the tubes then is sent to drive gas turbines for electricity generation or other uses. It has also been suggested that the hot gases be used along with steam to drive a combined cycle of both steam and gas turbines (30).

In order to make such concepts practical realities, a fundamental understanding of the hydrodynamics and heat transfer between a fluidized bed and immersed surfaces is of critical importance, particularly for large particles beds (D_p > 1 mm) at elevated temperatures (T_f > 800 K) because fluidized bed combustor design involves operation at such conditions. However, these phenomena are complicated due to the large number of bed parameters involved, which include particle size, shape, and physical properties; type of distributor; and the configuration of the immersed surfaces such as size, shape, spacing, and pitch (122,145).

The following two sections give a review of the fluidization phenomena and heat transfer mechanisms in a gas-solid fluidized bed with emphasis on large particle beds with immersed horizontal tubes. More general discussion can be found in the books by Botterill (30), Davidson and Harrison (51), Kunii and Levenspiel (99), and Zabrodsky (145).

1.2 Fluidization Phenomena

The hydrodynamics of fluidization is an essential factor in fluidized bed heat transfer processes. A typical fluidized bed consists of a tank partially filled with solid particles. When a fluid, either gas or liquid, is passed through it at a steadily increasing rate, the solid particles offer resistance to the fluid flow. Eventually a point is reached where the pressure drop across the bed is just equal to the weight of the bed particles. At this point the bed is said to become fluidized.

Beyond the onset of fluidization, the pressure drop across the bed remains the same as the fluid flow rate increases. In a liquid fluidized bed, the bed experiences a continuously uniform expansion. However, behavior of a gas fluidized bed is quite different. Expansion is not uniform as the gas flow rate goes up, except for fine particles (D_p < 0.1 mm), and a bubbling stage is reached. The phenomenon appears much like vapor bubbles in a boiling liquid. Gas, in excess of that needed for minimum fluidization, is channeled through the bed in forms of rising cavities containing few solids. As the gas flow rate further increases, the bubbles may coalesce and grow as they rise, probably leading to a slugging stage if operation is in a deep bed (2,99). Figure 1.1 displays a typical representation of different stages in a gas-fluidized bed of large particles.

Most fluidized beds operate in the bubbling stage because of the high rates of particle circulation and heat

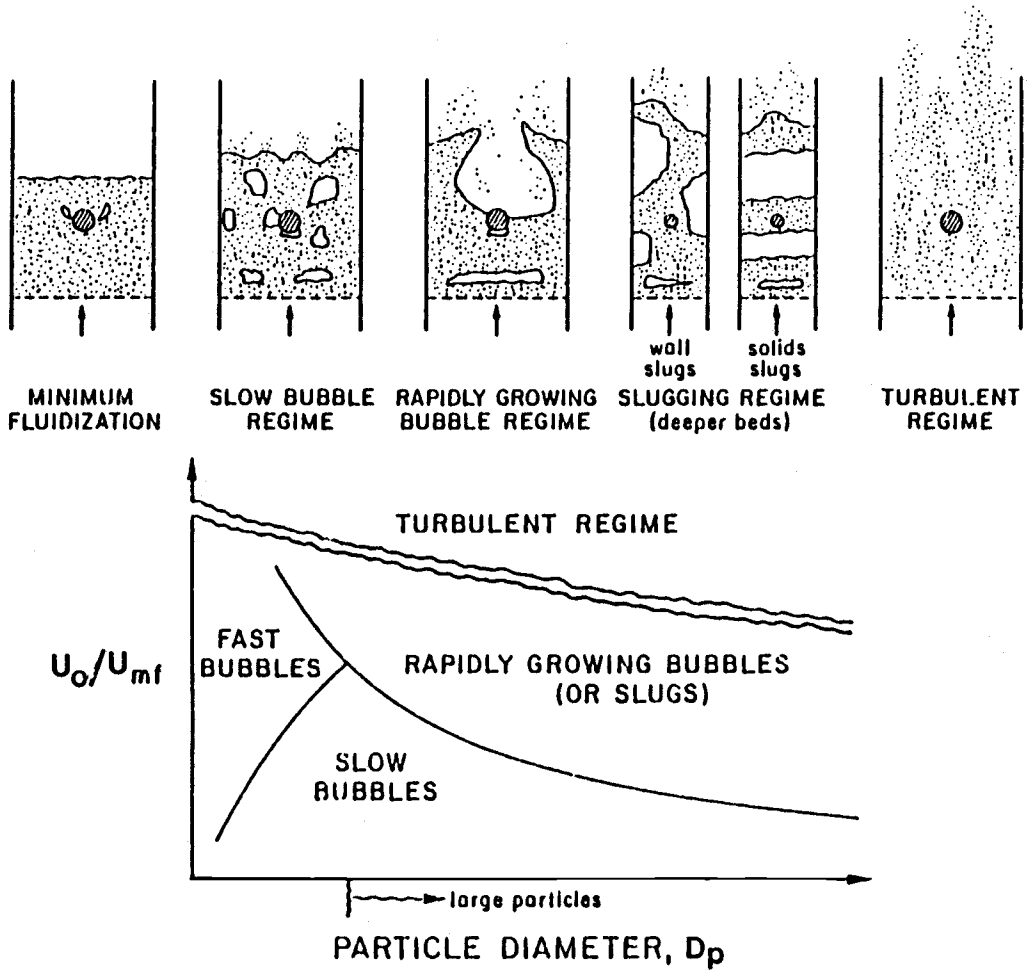

Figure 1.1 Fluidization phenomena and regimes in large particle bed. [Adapted from Catipovic, N. M. (40)]

transfer. The bubble behavior, such as rising velocity, size, and frequency, has been studied extensively in the world of fluidization. It was noted that the behavior varies for large and small particles (42,91,92). Catipovic, et al. (42) developed a slow-fast bubble criterion for fluidization of large particles, as shown in Figure 1.1. The conventional fluidized bed boilers (AFB) are operated in the slow bubble regime and circulating fluidized bed boilers (CFB) are operated at a higher gas velocity, which generally falls in the slugging or turbulent regime (107).

The bubble behavior and the bubble-induced particle circulation around immersed horizontal tubes is of major importance regarding bed-to-tube heat transfer study. Figure 1.2 shows a typical distribution of bubbles and particles around a horizontal tube in a bubbling bed. Jovanovic (91) indicated that bubble behavior for beds with immersed tubes exhibits smoother characteristics than for empty beds. There is a defluidized cap called a "lee stack" formed on top of the tube at velocities near U_{mf}. As the gas velocity increases, particles in the defluidized cap will eventually be swept back into the emulsion phase as a result of bulk circulation (69). Hager and Schrag (84) described this movement as in Figure 1.3. The rate of particle replacement increases dramatically as excess gas velocity goes up.

Gelperin, et al. (65) observed that the cap of defluidized particles tends to be less stable on tubes in an array than single tube due to the higher local gas velocity

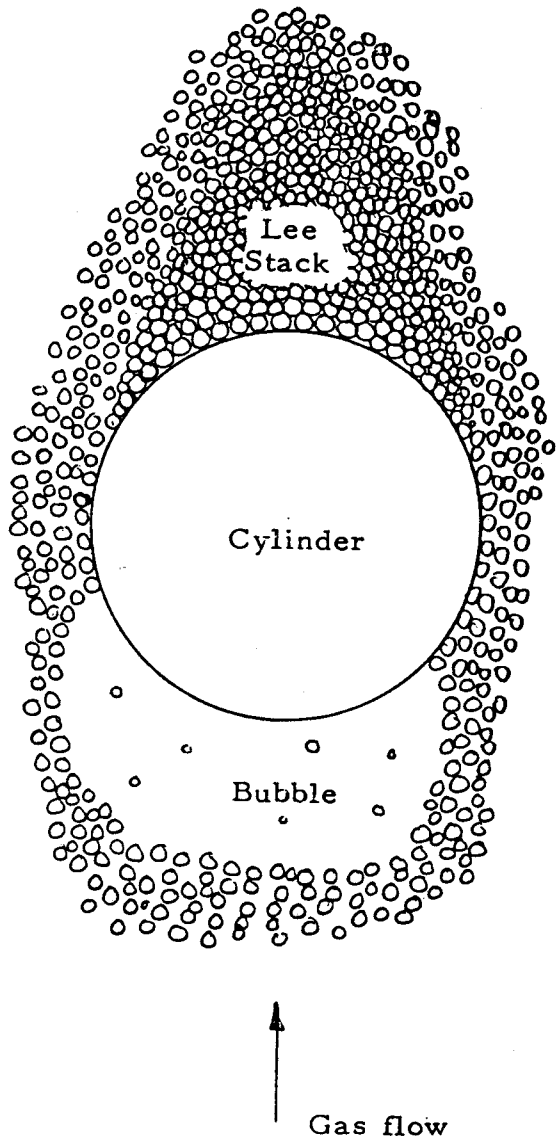

Figure 1.2 Particle packing around an immersed horizontal tube. [Adapted from Adams, R. L. (1)]

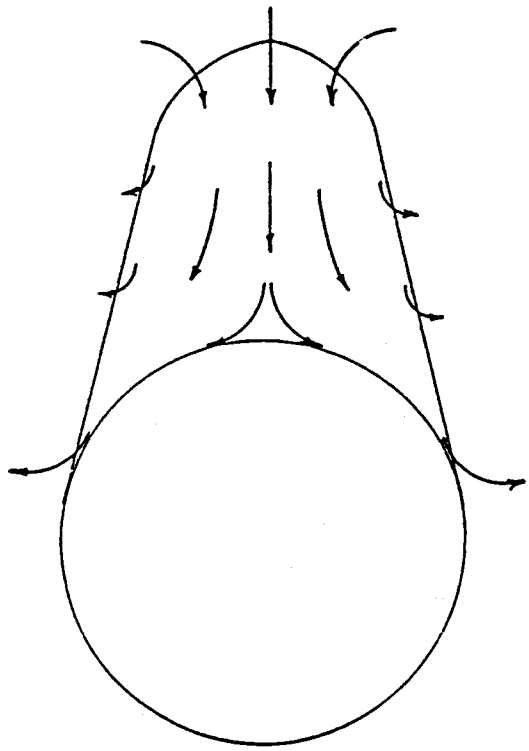

Figure 1.3 Pattern of particle circulation in the defluidized cap.

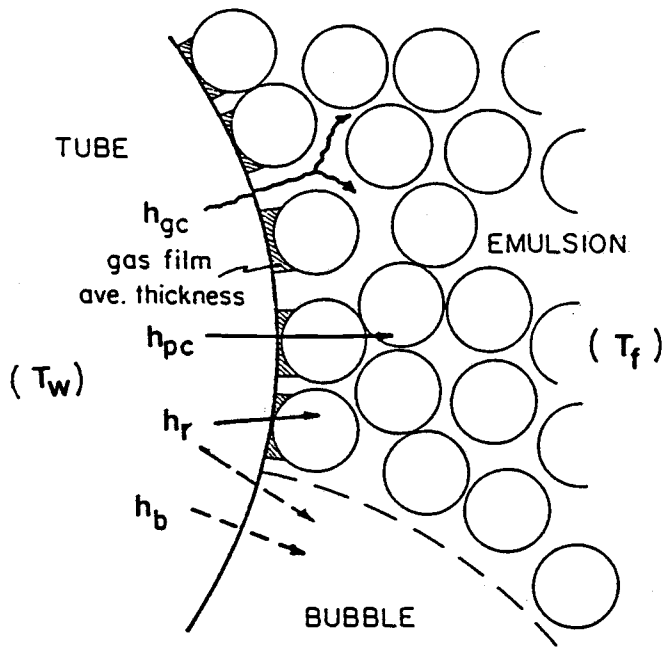

Figure 1.4 Different heat transfer mechanisms between a fluidized bed and a immersed tube.

between tubes. It has been noted that the lower portion of the tube is generally shrouded by gas bubbles, as shown in Figure 1.2 (85,120). However, for the case of an array of tubes, Keairns (94) found that there is an alternating character to bubble flow around a tube which results in a constant replacement of particles in the lower portion.

1.3 Heat Transfer Mechanisms

The analytical approach and derivation of predictive correlations for the heat transfer between a fluidized bed and immersed surfaces has been a fertile field, as summarized by Botterill (30), Saxena, et al. (122), Zabrodsky (145), and others (51,79,100). A qualitative description of the heat transfer between a bubbly bed and immersed surfaces follows. As bubbles contact a surface, an ongoing exchange of particles occurs. Fresh particles from the bulk of the bed come into contact with the surface, giving up heat, and remain for a finite time until they are displaced by the next coming bubble. Heat transfer is described by equation (1.1), proposed by Gelperin and Einshtein (63,64).

$$h_t = (1-f_o)\ h_{pc} + (1-f_o)\ h_{gc} + f_o\ h_b + h_r \qquad (1.1)$$

Where h_{pc} = particle convective component in emulsion phase

h_{gc} = gas convective component in emulsion phase

h_b = gas convective component in bubble phase

h_r = radiative component in both phase

f_o = bubble contact fraction

The four components occur in a parallel manner, as shown in Figure 1.4. The dominance of each component depends on the variation of system parameters, such as particle size, superficial velocity, and bed temperature. Generally speaking, the particle convective component becomes dominant when the particle Reynolds number (Re_p) is low, as for the case of small particles or at low temperatures (30,63). The gas convective components become important when Re_p is high, as for the case in which large particles or high pressures are encountered (42,63). Figure 1.5 shows the experimental results along with model predictions for the maximum heat transfer coefficients obtained by Catipovic (40) for a fluidized bed at ambient temperatures. It clearly displays the shift of dominance from one of particle convection to gas convection as the particle diameter increases. The radiation component also has a significant contribution at high temperatures.

1.3.1 Theoretical Models

Theoretical approaches differ in the way in which fluidized particles are treated and in the role each component plays in the heat transfer process. Most existing models incorporate the heat transfer behavior described

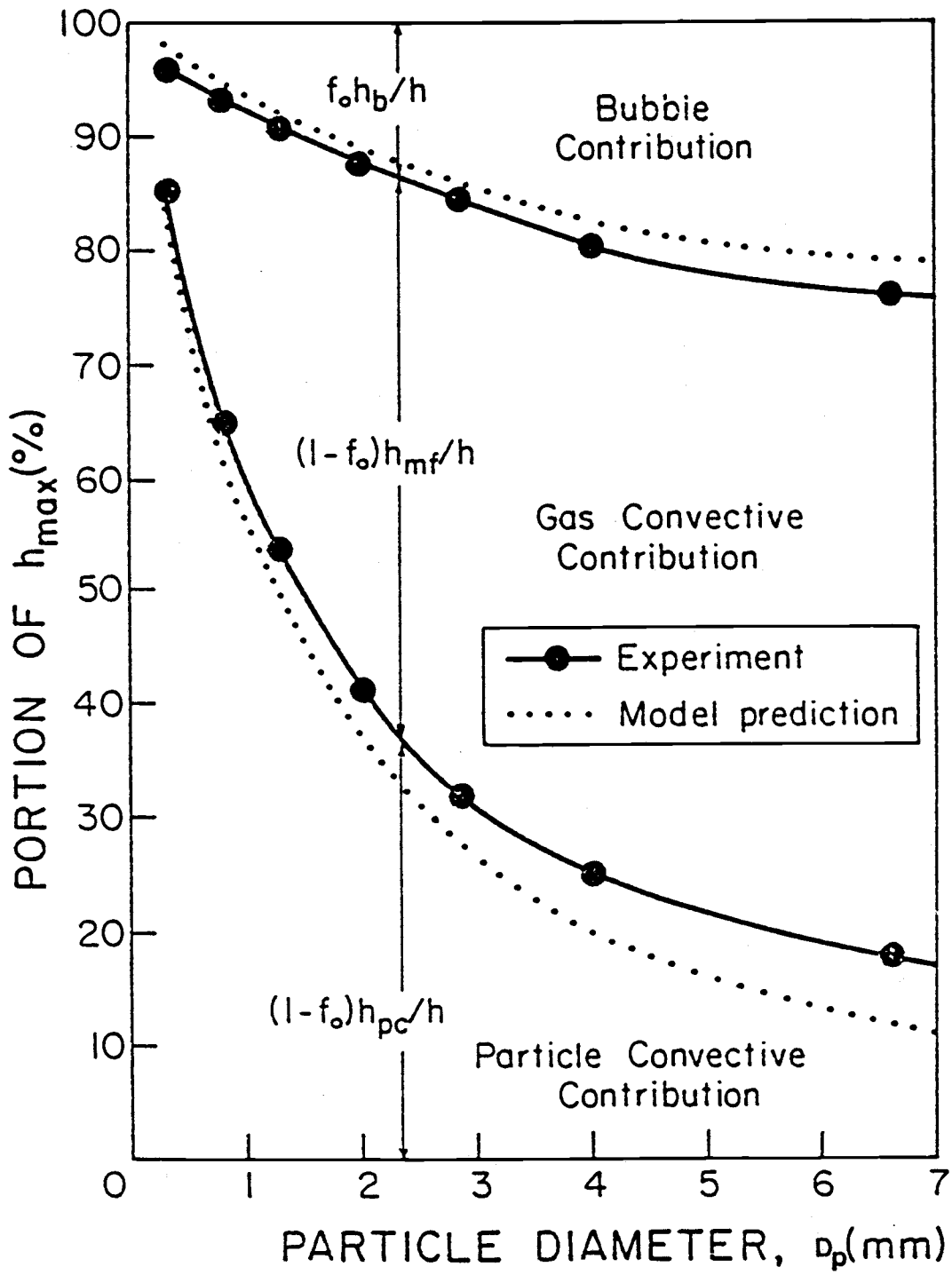

Figure 1.5 Contribution of different heat transfer mechanisms to the maximum time-averaged heat transfer coefficient in a cold bed. [Adapted from Catipovic, N. M. (40)]

above by considering emulsion residence time and bubble contact fraction into their analyses (9).

Fluid Film Model

Levenspiel and Walton (102) proposed a "fluid film" model as in a general convective heat transfer process. Bed particles were treated as obstacles to reduce fluid film resistance by the scouring action of particles in motion, and their thermal properties were assumed not to effect the heat transfer, which is not supported by experimental results of various investigators (132,149,150). However, this model was successful in some earlier studies (56,102,136).

Packet Model

The "packet" model, first proposed by Mickley and Fairbanks (111), considers that packets of particles are in contact with immersed surfaces, transferring energy by conduction during their residence times until they are swept away by the gas flow. The heat transfer rate is dependent upon the voidage and effective thermal properties of the bed materials. Packet models work reasonably well in dense beds in which packet residence time is long and/or bed particle diameter is small. Experimental evidence (60,86) indicates that they may overpredict heat transfer rates for short residence times since they predict rates which are inversely proportional to the square root of the residence time, which

is not physically reasonable. Schlunder (123) suggested a physically limiting value for the heat transfer coefficient for beds with short residence times. Several modifications were made by adding a contact resistance (18,79,98,116,143,144) attributed to various effects at the bed-surface interface. Kubie and Broughton (98) took into account the effect of immersed surfaces and bubbles on the thermal properties of the bed. More recently, Chandran and Chen (43) proposed a mechanistic model for local heat transfer coefficients with horizontal tubes immersed in small particle beds. This model was based on their previous information of bed-surface contact dynamics and transient conduction into the "packet" (45). Chen and Chen (48) obtained a numerical solution to the energy equation coupling the conduction terms and a two-flux radiation term. Pillai (119) added the radiative component to the "packet" model of Kubie and Broughton with an effective bed emissivity and an effective radiating cavity-type voidage, which are determined empirically. Vedamurthy and Sastri (134) obtained the radiation contributions from both emulsion and bubble phases. Yoshida, et al. (144) also considered the radiation contribution in their emulsion layer model. All "packet" models are restricted in application to particle sizes less than 0.5 mm.

Chain-of-Particle Model

This model is based on unsteady conduction to chains of particles and heat is transferred from distinct particles rather than packets of particles. Gabor (60) simplified this model into a series of alternating gas or solid slabs. Botterill and Denloye (32), considered a boundary layer across a few rows of particles at the heat transfer surface and developed a model including the gas convective component for both packed and fluidized beds. Kolar, et al. (96) and Fatani (58) added a radiative component to the alternating slab model. It was noted (79) that chain-of-particles model yields a good approximation in the intermediate range (D_p ~ 1 mm) and coincides with the Mickley-Fairbanks model for long particle residence times.

Single-Particle Model

In the fluidized bed combustion of coal, operations involve large particles at elevated temperatures. In such cases, all components in equation (1.1) are expected to affect on the total heat transfer when operating in the bubbling regime. Hence, recent analytical developments have been directed toward large particle beds in the bubbly regime --- a single-particle approach.

These types of models are based on the assumption that transient conduction is confined to the first row of particles. Botterill and Williams (34) obtained a heat transfer solution and temperature distribution for a single

particle contacting immersed surfaces. Ziegler, et al. (149) and Chung, et al. (50) developed a penetration type model using a statistical distribution of particle residence time and assuming particles receive heat by gas convection. Based on the results of Ziegler, et al. (149), Basu (20) provided a theoretical prediction to examine the effect of coal combustion on the heat transfer rate to an immersed surface. Decker and Glicksman (53), applied a steady state particle-to-surface conductive heat transfer solution obtained in their earlier work (40), and proposed an over-all heat transfer equation valid for particles with thermal contact times much larger than particle residence times. Ganzha, et al. (62) and Staub (126) developed mechanistic theories to predict heat transfer at very high gas velocities (rapidly growing bubbles or the turbulent regime, Figure 1.1). Szekely and Fisher (128), using the single-particle model of Botterill and Williams (34), obtained a simple expression for the radiation contribution for small particles with long residence times. Brewster (35) and Brewster and Tien (36) proposed purely analytical models for radiative heat transfer in a fluidized bed by treating the particles as independent media for thermal radiation. Borodulya and Kovensky (28) and Borodulya, et al. (29), taking into account the effects of multiple particle reflections and the bed structure, developed a radiative heat transfer model for a surface immersed in fluidized beds; the emissivity of a bubbly bed was calculated using their model.

For heat transfer to horizontal tubes immersed in large particle fluidized beds, particularly the local heat transfer around tubes, none of the models mentioned is considered adequate since they do not include the effect of particle packing, as shown in Figure 1.2. Adams and Welty (2), analyzing gas flow between particles, developed a steady gas convection model including the influence of bubbles, particle packing, and adjacent horizontal tubes. This was the first effort to provide a detailed physical description of heat transfer between a large particle fluidized bed and an immersed horizontal tube. Adams (3,4,5,7), further suggested simplified formulae and extended them to packed and bubbly fluidized beds. A coupled gas-convection and transient conduction model including numerical solutions of the particle convective component was also developed by Adams (6). Experimental data (39,40,138) show that the Adams-Welty model works well for particle sizes larger than 2 mm in the slow bubble regime. Based on the Adams-Welty model (2,6), Mahbod (104) and Mahbod, et al. (105,106) developed a radiative heat transfer model by the net radiation method applied to an enclosure formed by spherical particles and a gray cylinder. Bakke (15) proposed a simplified version of the particle convective component of the Adams-Welty model by assuming one dimensional heat conduction with linearized particle surface boundary conditions.

Each of the approaches described above has been successful in modeling heat transfer mechanisms for certain ranges of operation conditions in fluidized beds. A universal and easy-to-apply model has yet to be developed. Such a model requires a thorough understanding of bed hydrodynamics, particle residence time, and the effects of particle configuration and thermal properties.

1.3.2 Predictive Correlations

A complete analytical model for predicting heat transfer between a fluidized bed and immersed surfaces seems unrealistic in view of the complexity of the heat transfer mechanisms. Thus, most design work relies on empirical correlations. A great number of empirical correlations have been proposed (30,79,122,145). These correlations are generally restricted to specific test conditions because they were developed on the basis of observed data in laboratory-scale fluidized beds with limited variation in parameters (122). Interested readers may refer to Grewal (79) and Saxena, et al. (122) for more detailed discussions.

Several correlations, regarding total heat transfer to immersed horizontal tubes in large particle fluidized beds at low temperatures, have been presented. Catipovic (40) first suggested a semi-empirical correlation based on bubble contact fraction (f_o). In terms of particle and tube Nusselt numbers (Nu_p and Nu_t), his correlation is

$$Nu_p = 6(1-f_o) + (1-f_o)Nu_{p,mf} + \left(\frac{f_o D_p}{D_t}\right)Nu_{t,b} \qquad (1.2)$$

where

$$Nu_{p,mf} = 0.0175\ Ar^{0.46}\ Pr^{0.33} \qquad (1.3)$$

$$Nu_{t,b} = (0.88\ Re_{tmf}^{0.5} + 0.0042\ Re_{tmf})Pr^{0.33} \qquad (1.4)$$

On the right-hand-side of equation (1.2), the first term represents particle convection, the second term is gas convection in the emulsion phase, and the last term is gas convection in the bubble phase. All properties involved are evaluated at the bed temperature and the values of $1-f_o$ are calculated using the following equations:

for a single tube

$$1-f_o = 0.48 + \frac{0.065}{(U_o - U_{mf}) + 0.125} \qquad (1.5)$$

for a tube array

$$1-f_o = 0.45 + \frac{0.061}{(U_o - U_{mf}) + 0.125} \qquad (1.6)$$

Glicksman and Decker (71) proposed a correlation based on bubble volume fraction (δ) and, in terms of particle Nusselt number, their expression is

$$Nu_p = (1-\delta)\ (9.42 + 0.042\ Re_p\ Pr) \qquad (1.7)$$

The values of $1-\delta$ can be obtained from the following correlation proposed by Babu, et al. (14)

$$1 - \delta = 1 + \frac{10.978\ (U_o - U_{mf})^{0.783}\ \rho_p^{0.376}}{U_{mf}^{0.937}\ \rho_f^{0.126}\ D_p^{1.006}} \qquad (1.8)$$

All properties in equations (1.7) and (1.8) are to be evaluated at the film temperature [$T_{fi} = (T_f+T_w)/2$]. More recently, Glicksman (70) has suggested more sophisticated correlations by treating the emulsion and bubble phases separately.

Zabrodsky, et al. (148) developed a semi-empirical correlation by using a theoretical model (145) combined with a modified gas convection term. Other correlations, Staub (126), Ganzha, et al (62), and Martin (108) are available. Grewal (79) found that the correlations by Catipovic, Glicksman and Decker, and Zabrodsky, et al., are in good agreement with most existing experimental data (25,26,38,39,40,46,75,80,81).

Glicksman and Decker (72) discussed the role of radiation and later, Glicksman (70) suggested the following well-known equation to estimate the upper limit of the radiative component in the emulsion phase for fluidized beds with large particles.

$$h_r = \frac{\sigma\ (T_f^4 - T_w^4)}{[(1/\epsilon_{ef}) + (1/\epsilon_w) - 1]} \qquad (1.9)$$

Based on the experimental data of Pikashov, et al. (117), Grewal (79) suggested the following equation to evaluate ϵ_{ef}

$$\epsilon_{ef} = (1 + \epsilon_p)/2 \qquad (1.10)$$

The effective bed emissivity (ϵ_{ef}) is higher than the particle emissivity (ϵ_p) due to the re-entrant geometry characteristic of particles in the emulsion phase (70). Borodulya and Kovensky (28) also proposed a theoretical model to calculate the value of ϵ_{ef} used in equation (1.9).

1.4 Experimental Studies

A large number of experimental studies have been reported which deal with the effect of various bed parameters on the heat transfer to immersed surfaces in fluidized beds (2.3). Most of these studies were conducted in small-particle beds and at low temperatures. Some efforts, however, have been directed toward the combustion application of fluidized bed --- large particle beds at high temperatures. Section 1.4.1 provides a brief review of heat transfer measurements with horizontal tubes immersed in large-particle beds. Previous radiative heat transfer studies in high-temperature beds are reviewed in section 1.4.2.

1.4.1 Total Heat Transfer

Most spatial-averaged total heat transfer studies have involved measuring inlet and outlet coolant temperatures and estimating tube surface temperatures (9). Wright, et al. (141,142) was the first to obtain spatial-averaged total heat transfer data for a horizontal tube array immersed in a large particle bed. Several more recent studies involving similar measurements were performed by Grewal and Goblirsch (80), Golan, et al. (75), Leon, et al.(101), and several others (25,27,74,81,129,148). Ku, et al. (97) obtained data at very high superficial velocities, the turbulent regime (Figure 1.1), which are of value in the design of circulating fluidized beds (22). Experimental data in large particle beds show similar trends as for small particles beds. Heat transfer rates increase sharply as a result of the transformation from packed to fluidized bed conditions with a maximum value occurring at a certain optimum superficial velocity (U_{op}), followed by a slight decrease with a further increase in superficial velocity. It has been observed that the heat transfer rate for large particles is much lower than for small particles.

A number of different techniques have been applied in obtaining local heat transfer measurements. Berg and Baskakov (23) measured the surface temperature difference across a heated tube immersed in a small particle bed. Local data were obtained by solving a one-dimensional heat conduction equation across the tube wall. Similar

experiments were performed by Samson (121) and Gelperin, et al. (8). Heating elements attached to the tube surface were employed in some later studies, as performed by Cherrington, et al.(49) and Chandran, et al.(46) in beds of intermediate-sized particles. Applying a similar technique but with fast-response measuring elements made of platinum, Catipovic (40) obtained instantaneous and local heat transfer data for a wide range of particle sizes (.37 mm $\leq D_p \leq$ 6.6 mm) in a cold bed. George (94) first obtained local heat transfer data for a single tube, and Goshayeshi, et al. (78) for an array of tubes, in a large-particle bed at elevated temperatures. Thermopile heat flux sensors, covered with a thin foil for protection against bed abrasion, were used in their experiments.

1.4.2 Radiative Heat Transfer

An understanding of radiative heat transfer to immersed tubes is of interest in the design of fluidized bed combustors. It is generally accepted that this component increases with bed temperature, particle size, and particle or tube surface emissivity. A number of models, as described in section 1.3, have been developed to evaluate the radiation contribution for both small- (20,96,128,134,144) and large- (70,104) particle fluidized beds. The quantitative influence of these parameters, however, is hard to ascertain and a consensus has not been obtained. The wide variation between different models has been discussed by

Zabrodsky (146), Saxena, et al. (122), and Basu (20). Grewal (79) also indicated that most models are difficult to apply since they require the knowledge of particle/packet residence times and/or bubble contact fraction which are generally not provided. Furthermore, the predictive correlation proposed by Glicksman (70), equation (1.9), only gives an upper limit for the radiative component in the emulsion phase (fixed bed condition). Thus, design information remains reliant on experimental data.

There are relatively few experimental studies of radiative heat transfer. The data reported in different studies are summarized in Table 1.1, which also lists the test conditions and the radiation contribution (f_{ave}). A description of the conclusions of the various studies is presented. The methods employed and possible errors in different investigations will be discussed in section 2.1.

Kharchenko and Makhorin (95) investigated total heat transfer to a spherical alpha-calorimeter immersed in a bed. They concluded that radiant heat transfer is insignificant for bed temperatures up to 1273 K, a conclusion supported by Gelperin and Einshtein (79) and Dunsky and Tamarin (57). Yoshida, et al. (144) and Szekely and Fisher (128), based on their experimentally tested models, reached the same conclusion for small particles or long-particle residence times. Experiments made by Yoshida, et al. also showed the effect of tube surface emissivity on radiative heat flux. Results of Ilchenko, et al. (90) showed that the radiation

Investigator(s)	D_p (mm)	T_f (K)	f_{ave} (%)
Kharchenko & Makhorin (95)	0.34-1.66	433-1273	negligible
Szekely & Fisher (128)	0.1-0.15	600-650	negligible
Yoshida, et al. (144)	0.18	823-1273	negligible
Ilchenko, et al. (90)	0.57-1.75	703-1703	18-50
	0.57	1223	20
	1.75	1223	24
Botterill & Sealy (33)	0.2-3.0	773-1673	5-60
Wright, et al (142)	0.5-6.4	1123-1173	30-50
Baskakov, et al. (18)	0.35-1.25	1123	6-32
	0.35	1123	9
	1.25	1123	32
Vedamurthy & Sastri (135)	<3.15	1173	20-40
	<6.3	1173	50-60
Basu (20)	0.325-0.5	1073-1173	5-10
Ozkaynak, et al. (114)	1.03	523-1033	7-35
Vadivel & Vedamurthy (131)	0-6	1023	35
Alavizadeh, et al. (11,12)	0.52	812	6
	1.00	812	8
	2.14	812,1050	12,20
	3.23	812,1050	14,22

Table 1.1 Measurements of radiation contribution in different studies.

contribution was about 20% for zirconium oxide particles (D_p = 0.57 mm) and 24% for corundum particles (D_p = 1.75 mm) at T_f = 1223 K. Botterill and Sealey (33) analyzed the data of Pikashov, et al. (118) and found that the radiation contribution varied from 5% to 10% at T_f = 773 K and 50% to 60% at T_f = 1673 K for D_p = .2-3 mm.

Wright, et al. (142) calculated the radiation to be between 30% and 50% for mixed particle sizes and T_f = 1123-1173 K. Calculations were based on the assumption that thermal radiation to surfaces immersed in a well-agitated bed can be treated as if it were black. Baskakov, et al. (18) measured the radiative heat transfer to surfaces at various temperatures and immersed in a bed consisting of chamotte particles. An increase of the radiation contribution with surface temperature was observed. Calculations from Bhattacharya and Harrison (24) show a similar dependence for an air-sand system with D_p = .35 mm.

Vedamurthy and Sastri (135) first measured spatial-averaged radiative heat transfer to a horizontal tube immersed in a large particle bed at T_f = 1023-1323 K. Their data indicated that the radiation contribution at T_f = 1173 K for different superficial velocities (U_o = .25-.45 m/s) varied between 20% and 40% for D_p < 3.15 mm, and between 50% and 60% for D_p < 6.3 mm. From both their experimental investigations (135) and analytical studies (134), they found the radiation contribution to be 20% to 40% for T_f = 1073-1273 K.

Basu (20) has also observed the role of radiation in fluidized bed combustors. Results of his studies indicate the radiation contribution to be about 5% to 10% of the total heat transfer for sand particles. More recent measurements by Ozkaynak, et al. (114) have shown the fraction of the radiative component to increase from approximately 7% at T_f = 523K to almost 35% at T_f = 1033 K. Silica sand was used as a bed material and the superficial velocity was varied from 1.5 to 4.83 m/s in this work.

Vadivel and Vedamurthy (131) pioneered the investigation of local radiative heat transfer to a horizontal tube immersed in a fluidized-bed coal combustor. Tests were conducted at a bed temperature of 1023 K and different superficial velocities (U_o = 0.87-1.7 m/s) for D_p = 0-4 mm and 0-6 mm. A radiation contribution of about 35% was found for D_p = 0-6 mm. The variation of local radiative and total heat transfer coefficient with superficial velocity and particle size was examined.

Alavizadeh (9) and Alavizadeh, et al. (11,12) measured local radiative heat transfer for a horizontal tube immersed in small and large particle beds with superficial velocities up to 3.3 U_{mf}. The radiative heat transfer was determined using a specially designed instrumented tube which will be discussed in detail in chapter II. The relative contribution due to radiation for a black tube was found to increase from 6% to 14% with D_p from 0.52 mm to 3.23 mm at T_f = 812 K, and

to increase from 14% to 22% with T_f from 812 K to 1050 K for D_p = 3.23 mm.

1.5 Present Work

The majority of both analytical and empirical efforts have been directed toward heat transfer studies of small particles (D_p < 1 mm) and/or low temperatures (T_f < 800 K) where unsteady particle conduction is to be considered. Some experimental studies have been reported which involve total heat transfer measurements in large-particle beds. Only limited attempts have been made to measure the radiative component separately and published data show considerable variation in the role of radiation as shown in Table 1.1. No published data have been found dealing with radiative heat transfer measurements to in-bed tube arrays.

The objective of the present study was to measure the local bed-to-tube radiative and total heat transfer rates for a horizontal tube array immersed in a large-particle, high-temperature fluidized bed. A well designed instrumented tube, developed by Alavizadeh, et al. (11) and proved in this study, was employed to evaluate the effects of different bed parameters. The results are also of use in estimating the radiation contributions for tubes with different emissivities.

Chapter II provides a description of the design, assembly, calibration, and experimental verification of the radiation detectors employed in this study, as a supplement

to the analysis done by Alavizadeh, et al. (11). Three different window materials, silicon, sapphire, and fused quartz, were employed and their performance was tested. This experimental program yielded properly-designed, well-calibrated, and direct-measuring devices capable of measuring local bed-to-tube radiative heat transfer.

Chapter III is devoted to describing the apparatus and experimental set-up, including a description of the instrumented tube, tube-array design, the data acquisition system, and the high-temperature fluidized bed test facility. Also described are the test conditions and procedures, data collection, and the methods of conversion of voltage signals to heat flux and heat transfer coefficients.

Chapter IV is a presentation of experimental results and discussion. Spatial-averaged and time-averaged local heat transfer coefficients with respect to superficial velocity are shown for two particle sizes (D_p = 2.14 mm and 3.23 mm) and three different bed temperatures (T_f = 812 K, 925 K, and 1000 K). The effect of superficial velocity, bed temperature, particle size and, most importantly, neighboring "cool" tubes in a hot bed, are discussed. Comparisons are made between the results of this present study and others.

Chapter V gives conclusions of present study and recommendations are made for possible future work.

II. RADIATION DETECTOR

Accurate and reliable instruments are essential for measuring the radiative heat transfer rates to surfaces immersed in a hot fluidized bed. The radiation detectors, originally developed by Alavizadeh, et al. (11) were used in this work. This chapter includes the experimental verification of some key design decisions made by Alavizadeh, et al. in the development of the radiation detector. Some modifications were made in the configuration and calibration procedure to improve the detector operation.

2.1 Comments on Previous Investigations

Methods employed and possible sources of error in some radiative heat transfer observations in a fluidized bed have been discussed by Saxena, et al. (122), Basu (20), Ozkaynak, et al. (114), and Alavizadeh, et al. (9,11).

Kharchenko and Makhorin (95) based their conclusion of an insignificant radiation contribution on an observed linear relationship between the total heat transfer coefficient and bed temperature. Basu (20), and Saxena, et al. (122) indicated that this is somewhat questionable because the variation of the conductive and radiative components with bed temperature are both nonlinear. These nonlinearities were thought to compensate and result in a linear relationship when the two are added together; this being caused by the change of particle density and residence

time with bed temperature. Experiments of Szekely and Fisher (128) were carried out by transmitting heat from a source through a transparent wall. No data at bed temperatures higher than 650 K were obtained due to the limitations of power input and cooling air capacity.

In investigations by Yoshida, et al. (144) and Baskakov, et al. (18), radiative heat transfer was measured indirectly by specially designed calorimetric metal probes with different surface emissivities. Yoshida, et al. compared the total heat transfer between an oxidized pipe and a polished stainless steel pipe immersed in a bed. Total heat flux was obtained by measuring the temperature change of the coolant. Surface emissivities of the pipe surfaces were calculated using the net radiation method. Baskakov, et al. recorded the transient temperatures of two low Biot number spheres immersed in a bed, one with an oxidized surface (ϵ_w = 0.8) and the other with a silver-plated surface (ϵ_w = 0.1). Ozkaynak, et al. (114) indicated that uncertainties in surface emissivity values and the effects of varying surface temperatures could lead to underestimating radiative heat flux. The higher figure recorded by Baskakov, et al., as shown in Table 1.1, can be explained by neglecting the cooling of particles on the heat transfer wall (18,20). The same explanation is applied to the overprediction by Wright, et al. (142).

Basu (20) used two identical copper tubes of 6.5 mm outside diameter. One of the tubes was covered with a

coaxial transparent silica tube to reduce thermal conduction to the copper tube and a correction was made for its conduction error. Heat transfer rates were calculated by measuring the inlet and outlet coolant temperatures. The radiative component was obtained by comparing the heat transfer rates between these two tubes.

Quartz glass has been widely employed as the transparent window material in direct measurement of radiative heat transfer to surfaces immersed in fluidized beds, as performed by Ilchenko, et al. (90), Botterill and Sealey (33), Vedamurthy and Sastri (135), and Vadivel and Vedamurthy (131). The function of the transparent quartz window, which was mounted on the top of a cavity within the probe, was to eliminate incident convection and transmit radiant energy. Transmitted radiant energy was detected by a thermoelectric device mounted on the bottom of the cavity. Calibration of the probes, employing a hohlraum as the standard source of heat, was made in the studies of Vedamurthy and Sastri and Vadivel and Vedamurthy. All data obtained in the above studies are comparatively high relative to the others, as shown in Table 1.1. This is because the bed particle/gas convective heat transfer produces near bed temperature on quartz window due to its low thermal conductivity ($k = 1.7$ W/m.K), which results in a conduction error through the gas gap in the cavity (11,114).

Ozkaynak, et al. (114) utilized a two-layer flat window of zinc selenide mounted on the flat end of a 60 mm

cylindrical brass body covered with a copper plate. Zinc selenide has a relatively high thermal conductivity (k = 13 W/m.K) and an effective transmittance band of 0.5 μm to 20 μm. Cooling air was circulated through the gap between windows to eliminate the conduction error. The radiometer probe was calibrated using a black body source.

Table 2.1 summarizes the methods employed and possible sources of error among different studies. The radiative heat transfer rates were obtained either indirectly by using a transparent wall (20,128), emissivity differences (18,144), and simplified calculations (113,142), or directly by a specially-designed radiative probe using quartz (33,90,131,135) or zinc selenide (114) as transmitting media to detect radiation. In the latter case, a high conduction error was introduced when using quartz as explained earlier. Quartz is opaque to incident radiation with wavelength longer than 4.8 μm (83,139), as shown in Figure 2.2 (8), while the actual radiation from a high temperature fluidized bed could involve wavelengths from 2.7 μm to 8.7 μm (125). Calibration of the radiation instrument was not addressed in most of these investigations. The emissivity of the heat transfer surface, a decisive factor in determining the actual radiative heat transfer, was also not reported in all of the reports cited.

Investigator(s)	Method	Source of error
Kharchenko & Makhorin (95)	Spherical calorimeter	Based on $h_t \propto T_f$
Szekely & Fisher (128)	Transparent bed wall	insufficient data
Yoshida, et al. (144)	Emissivity difference	Experimental uncertainties
Baskakov, et al. (18)	Emissivity difference	Experimental uncertainties
Wright, et al. (142)	Black body calculations	Wrong assumption
Basu (20)	Transparent heater wall	———
Ilchenko, et al. (90)	Radiative probe	Conduction through gas gap
Botterill & Sealey (33)	Radiative probe	Conduction through gas gap
Vedamurthy & Sastri (135)	Radiative probe	Conduction through gas gap
Vadivel & Vedamurthy (131)	Radiative probe	Conduction through gas gap
Ozkaynak, et al. (114)	Radiometer probe	———

Table 2.1 Methods and possible sources of error among different studies.

2.2 Design Analysis

The basic design concept of the radiative detector employed in this study is illustrated in Figure 2.1. It is similar to that of Ilchenko, et al. (90) and Vedamurthy and Sastri (135). Thermal radiation from the bed is transmitted through a transparent window mounted on the top of a cavity within the instrumented tube, and is detected by a heat flow sensor bonded to the base of the cavity.

2.2.1 Window Materials

The choice of window materials plays a dominant role regarding the accuracy of direct measurements of radiative heat transfer in fluidized beds (9,11,139). Generally speaking, windows with the following properties are preferred:

a) Windows should have high thermal conductivity in order to minimize conduction through the window into the cavity.

b) Windows should transmit over the widest possible range of wavelengths.

c) Window materials should be as hard as possible to withstand the abrasion of particle motion in the bed environment.

Alavizadeh, et al. (11) analyzed four different window materials, silicon, sapphire, crystal quartz, and fused quartz, as potential candidates for transmitting medium. A summary of his analysis is described in section 2.2.3.

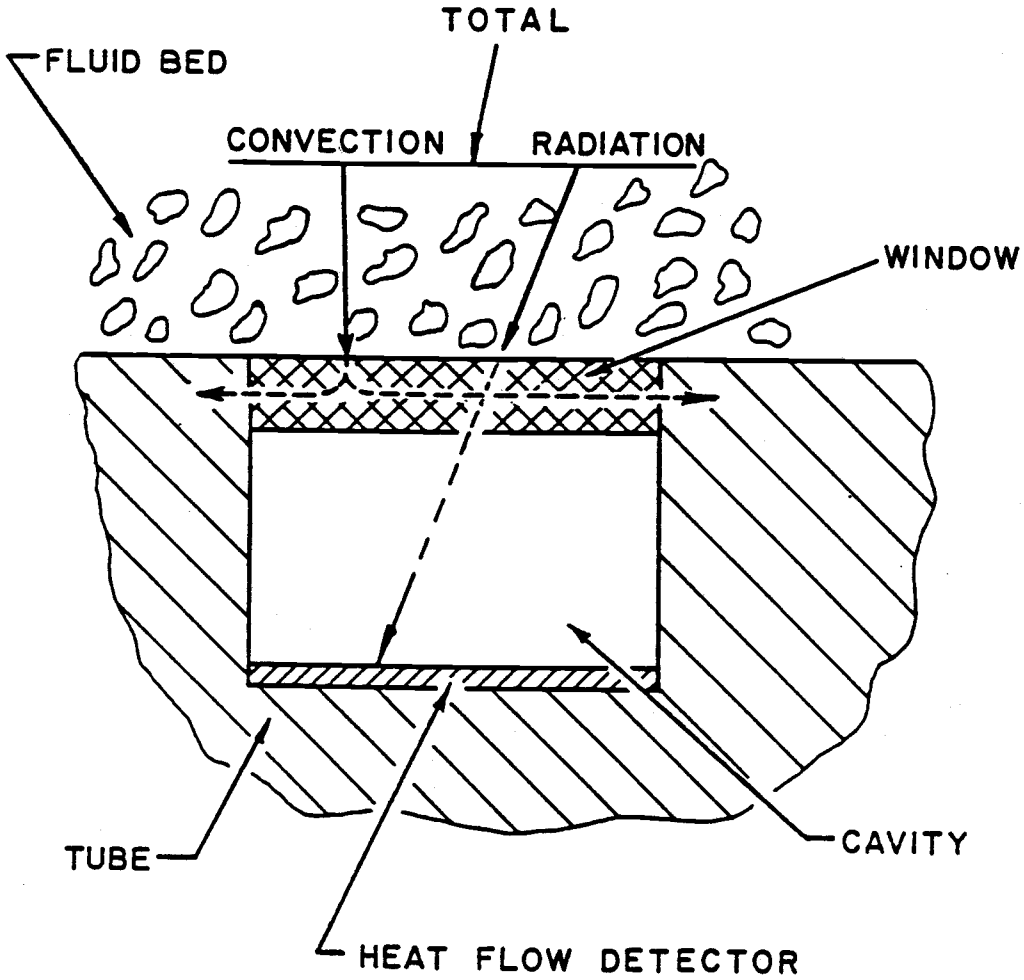

Figure 2.1 Basic design concept of radiation detector.

Silicon was found to be the superior choice and was selected as the window material in their study. Three different window materials, silicon, sapphire, and fused quartz, were employed in the experimental verification of the analysis done by Alavizadeh, et al. The transmission characteristics of the three windows are shown in Figure 2.2 (8).

2.2.2 Heat Flux Sensor

The first layer of particles contacting the window surface has a nonuniform temperature distribution due to the cooling effect of the tube, which results in a nonuniform heat flux. This suggests the application of an averaging device such as a thermopile-type heat flux sensor in the design of radiative detectors. Hager (83) first used a thin foil heat meter, formed by a thin, low thermal conductivity film with a thermopile on each side, in heat transfer measurements of fluidized beds. Similar devices have been discussed by Brown, et al. (37).

Figure 2.3 illustrates the geometry of the selected heat flux sensor (No. 20455-1, RdF Inc., Hudson, NH) with dimensions of 0.76 mm x 12.7 mm x 28.5 mm and a maximum service temperature up to 523 K. A type T thermocouple is utilized in the sensor to monitor its surface temperature. The small fraction of the sensing area is an advantage of this type of sensor over others used for local heat transfer measurement.

A. SILICON

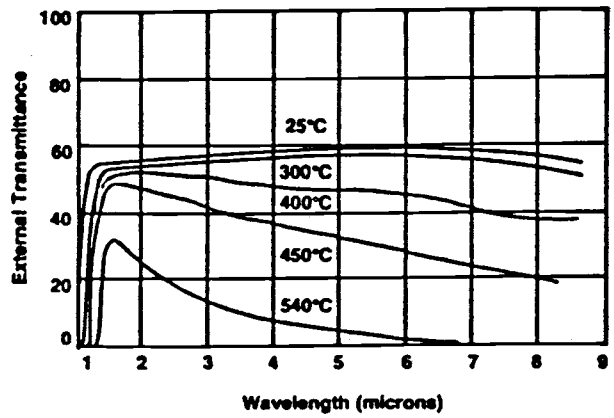

B. SAPPHIRE

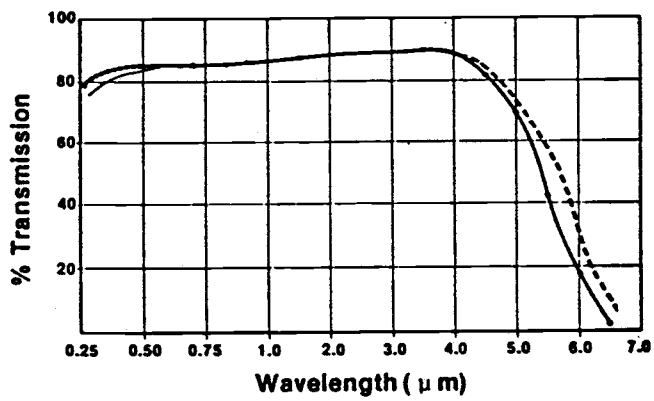

C. FUSED QUARTZ

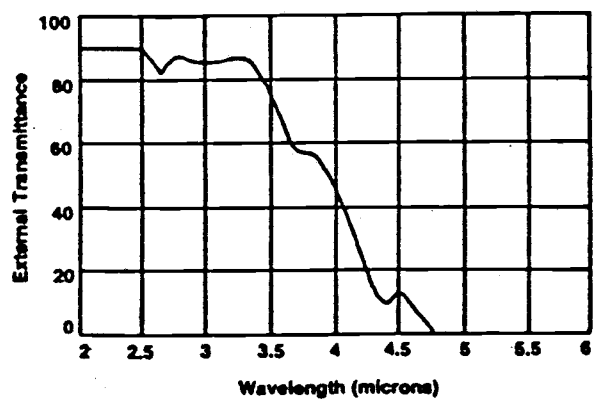

Figure 2.2 Transmission characteristics of silicon, sapphire, and fused quartz.

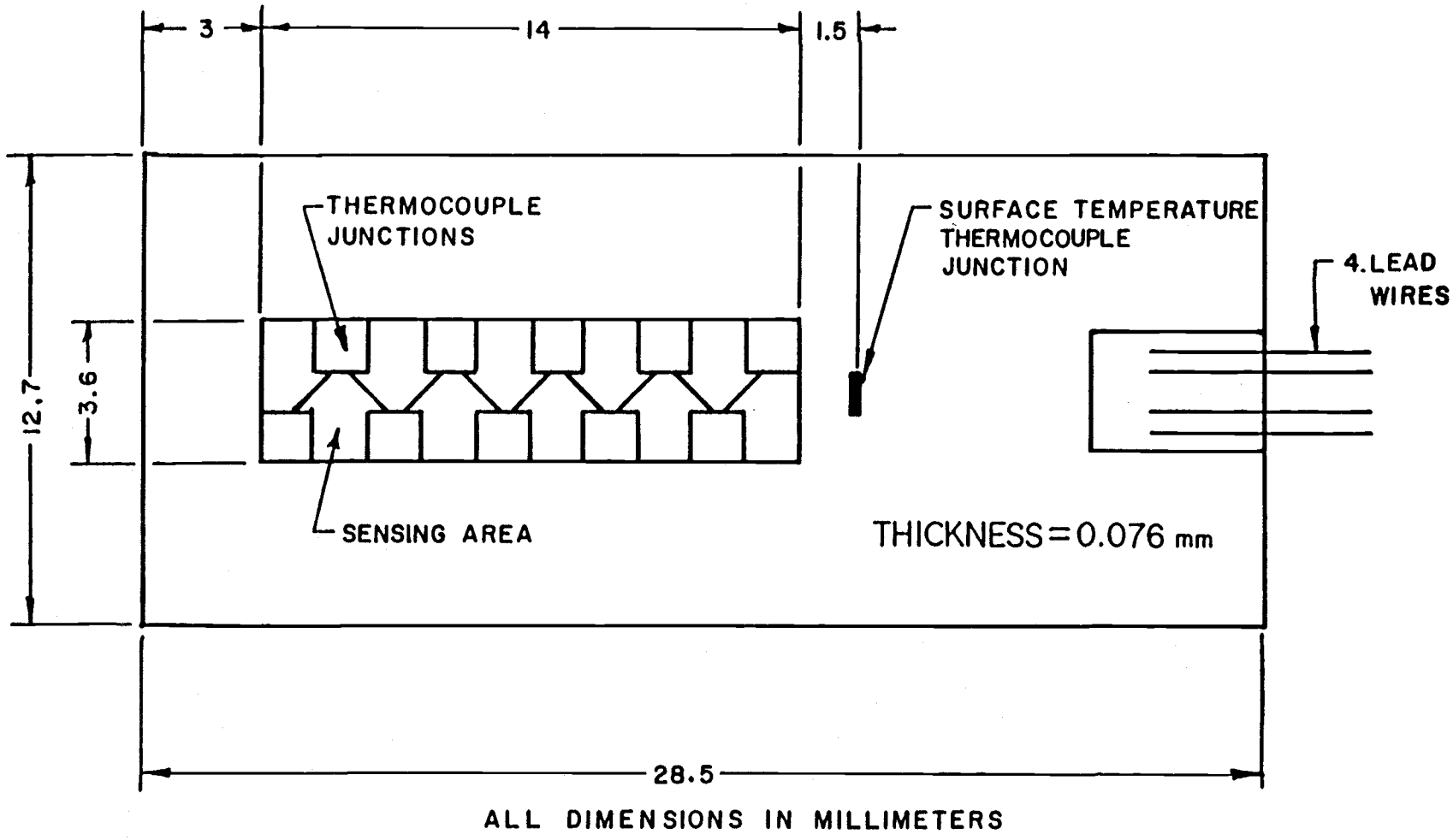

Figure 2.3 Geometry of the selected heat flux sensor.

A description of the principle and function of this type of heat flux sensor is the following. As heat conducts through the low conductivity thin film of the sensor, a temperature difference is established across it. The heat transfer rate is then calculated from the calibration data, and the output voltage signal (e_{mf}). The calibration data were provided by RdF Inc. as a function of sensor surface temperature. The e_{mf} is actually a reading of temperature difference across the sensor and it is independent of the type of the heat flux source. It can thus be applied in complicated measurements involving combined heat transfer modes. The same heat flux sensors were employed in the total heat transfer gauges without any correction. Information and heat flux conversions for these sensors can be found in Appendix A.

2.2.3 Theoretical Analysis

Alavizadeh, et al. (11) studied the effect of different design parameters and the performance of different window materials. This section summarizes the methods, results and conclusions of their investigation.

A three-dimensional steady-state conduction analysis was conducted to investigate the effect of nonuniform heat flux on the heat flux sensor performance. Two cases were compared, one with a uniform heat flux over the entire area of the sensors, and the very unlikely case of a uniform heat flux over the sensing area and zero over the rest of sensor

area. Using the calibration data provided by RdF Inc., it was found that the heat flux would be about 2.5% lower for the second case. The manufacture's calibrations are, thus, applicable to the nonuniform heat flux measurements involved in this study.

A two-dimensional heat conduction analysis was performed to assess the magnitude of the conduction error produced by the gas and the particle-convective heat transfer. The outside surface of the window was exposed to bed convection and the inside surface transferred heat, via one-dimensional heat conduction across the air-filled cavity, to the sensor. The magnitude of the conduction from the window to the sensing area was then calculated by averaging the heat conduction to it. The radiative heat transfer to the sensing area was estimated by the net radiation method for an enclosure including the window, heat flux sensor, and cavity walls. The relative conduction error was obtained from these two heat fluxes. An estimate of the average window temperature (T_{wi}) was calculated from the solutions for a two-dimensional heat conduction for different windows. It was used to examine the error in using T_{wi} as an approximation of T_w in the calculation of the radiative heat transfer coefficient, $h_r = Q/(T_f-T_{wi})$.

The outside window surface should conform to the tube contour to avoid any disturbance of the bed. This results in a plano-convex cylindrical lens and magnifies the transmitted radiant energy. A magnification factor, MF, was

calculated as "area of the window facing the bed/area of the focal plane on the sensor". The Grashof number (Gr) based on T_{wi}, T_w, and cavity height, was also calculated to investigate the effect of natural convection in the cavity.

Results of this analysis associated with the properties of the four potential candidates as window material are shown in Table 2.2. Two sets of data corresponding to the local maximum heat transfer rates at T_f = 812 K and 1050 K were considered with the larger error listed in Table 2.2. The table shows that silicon produces the smallest relative error in conduction (1%) and in the h_r calculation (2%). The larger MF of silicon (2.0) will further reduce its conduction error. It was found that the average window temperature, T_{wi}, is the largest for quartz, due to its low conductivity, and hence results in a further increase in the error in h_r, from 28% to 53%. The Grashof number is sufficiently small (Gr μ 1700) to allow natural convection in the cavity to be neglected for all the window materials considered. Based on the wide transmission band, high thermal conductivity and hardness, negligible conduction error, and no loss of accuracy using T_{wi} as an approximation for T_w, silicon was selected as the window material in their study.

2.3 Assembly

A schematic illustration of the radiative detectors is shown in Figure 2.4. Each detector was mounted within the

Window Materials	Transmission (Wave Band, μm)	Thermal Conductivity at T_{wi} (W/m•K)	Hardness (Knoop)	MF	Conduction Error (%)	Gr	T_{wi} (K)	h_{rb} Error (%)
Silicon (Si)	0.50 (1.3-7.0) 0.35 (7.0-12.0)	117.0	1150	2.0	1	91	354	2
Sapphire (Al_2O_3)	0.84 (0.30-5.0)	35.0	1370	1.2	3	213	374	5
Quartz, Crystal (SiO_2)	0.92 (0.30-2.2) 0.50 (2.2-3.6)	6.7	741	1.2	23	555	446	17
Quartz, Fused (SiO_2)	0.91 (0.30-3.4) 0.40 (3.4-4.7)	1.7	461	1.1	28	961	589	53

Table 2.2 Window materials with results of theoretical analysis. [Adapted from Alavizadeh, N. (9)]

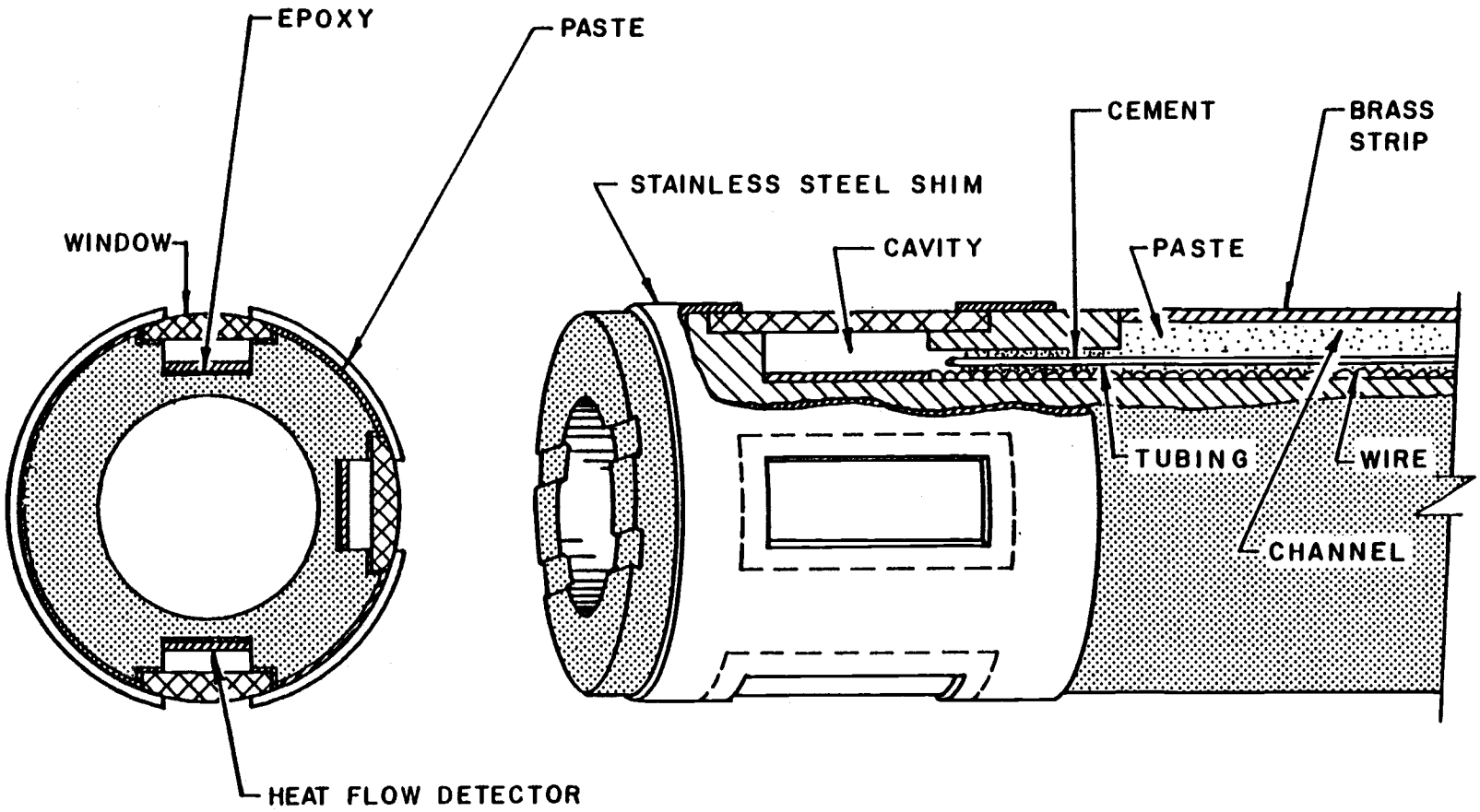

Figure 2.4 Assembly of radiation detectors in the instrumentation tube.

walls of the cavity in the instrumented tube. It has been modified to produce a wider view angle between the bed and the heat flux sensor by wrapping two stainless steel strips (0.127 mm in thickness), overlapping the window, to hold the window in position. A 17.5 mm x 30 mm window area is then exposed to the bed, instead of the original 14 mm x 30 mm area. Three instrumented ports were machined, each 90 degrees apart, to the size of the heat flux sensor (12.7 mm x 28.5 mm) with a depth of 4.8 mm. The larger upper portion was milled to house the window (17.5 mm x 41.4 mm) with a maximum depth of 3.2 mm. The three windows, made of silicon, sapphire, and fused quartz respectively were mounted on the ports by applying a high thermal conductivity paste (Omegatherm 201, k = 2.3 W/m.K and stable up to 478 K, Omega Engineering, Inc., Connecticut) to reduce thermal contact resistance. The silicon and sapphire windows were machined to have the same curvature as the outside of the tube (D_o = 51 mm). The quartz window was machined to have a flat surface (1.6 mm in thickness) in order to study the effects of the disturbance of gas-solid flow around the tube due to the flat section of its surface.

Three new microfoil thermo-pile type heat flux sensors were replaced and bonded to the bottom of the cavity by applying a high thermal conductivity epoxy adhesive (Omegabond 200, k = 1.4 W/m.K and stable up to 533 K). The sensors were coated with a new type of high absorptivity paint (3M ECP-2200, absorptivity = 0.96), instead of the

original 3M Nextle paint, to increase the absorption of transmitted radiation and thus reduce the uncertainties in the radiative heat flux measurement. The 3.2 mm hole connecting the cavity and wire channel was sealed with Omega CC cement and the channel was filled with Omegatherm 201. All cavities were connected to the atmosphere by 2.4 mm-diameter stainless steel tubes running through the wire channel for ventilation, which further reduced the window temperature, conduction error, and natural convection. Damage to the original heat flux sensors in the radiative detectors was probably due to the relatively poor ventilation of the original 1.6 mm tubing (9) or the operation in small particle beds which have much higher heat transfer rates.

2.4 Calibration

Calibration of the heat flux sensor was done prior to delivery by the manufacture, RdF Inc. The purpose of additional calibration was to relate the heat flux detected by the sensor to the actual radiation absorbed by the tube wall. Calibration was carried out locally using a narrow-angle black body source, Barnes 11-210 Radiation Reference Source (16). Details of the calibration techniques and procedures can be found in references (11) and (9). Some changes were made in order to enlarge the viewing angle of the heat flux sensor by moving the black body source to

about 1 mm (instead of the original 3 mm) away from the instrumented tube.

The total heat transfer gauges were painted with high emissivity lampblack (89), with a spectral emissivity of 0.96 from 0.2 μm to 20 μm wavelength, in order to generalize the results of the experiments as the radiation absorbed by a black tube. The incident radiation (Q_{rb}) absorbed by the black total gauges were used for reference, where Q_{rb} was taken as the average of the measurements on two total gauges. The correlation between the detected heat flux (Q_d) from the radiation detector, and Q_{rb} represents the calibration for the device. A well-designed alignment device (11) was employed to align the black body source and radiation detector to make the results (Q_d vs. Q_{rb}) comparable. No significant change in the calibration data was found due to the change of tube wall temperature and the effect of natural convection in the laboratory environment (9,11). Calibration could then be conducted at room temperature without a loss of accuracy.

Data were recorded employing a high precision data logger (HP-3497A) with a maximum sensitivity of 0.001 microvolt. The black body source temperature was controlled in the range from 400 ^{o}C to 1000 ^{o}C. The methods used in the conversion of recorded data from voltage to heat flux are discussed in Appendix A. Calibrations were made before and after each exposure to the bed in order to examine the possible changes of window transmissivity caused by particle

abrasion. No significant change in Q_d was noted following the first exposure to the bed, for all three window materials. The silicon window used by Alavizadeh, et al. (9,11,12) experienced approximately 20% drop in Q_d after its first exposure to the bed; no changes were observed thereafter (9,11).

Results of the calibration for these windows are shown in Figure 2.5. Data for the silicon window show a linear relationship due to the wide wavelength of transmission. This is an essential feature for accurate measurements of radiation heat transfer. The calibration relationship was determined by linear regression (112) to be

$$Q_{rb,si} = 1.72\ Q_d \qquad (2.1)$$

The maximum deviation for this expression is 6% at low heat fluxes (400-600 ^oC) and 1.5% in the high heat flux region (600-1000 ^oC) where the actual application is made. The relationship between Q_d and Q_{rb} was nonlinear for both the sapphire and quartz windows. Third and fourth order polynomial regression fits were performed for sapphire and quartz respectively. Results of these regressions are

$$Q_{rb,sa} = 0.035 + 2.74\ Q_d - 0.08\ Q_d^2 + 0.0018\ Q_d^3 \qquad (2.2)$$

$$Q_{rb,qz} = 0.658 + 4.48\ Q_d - 0.305\ Q_d^2 + 0.0162\ Q_d^3 - 0.00033\ Q_d^4 \qquad (2.3)$$

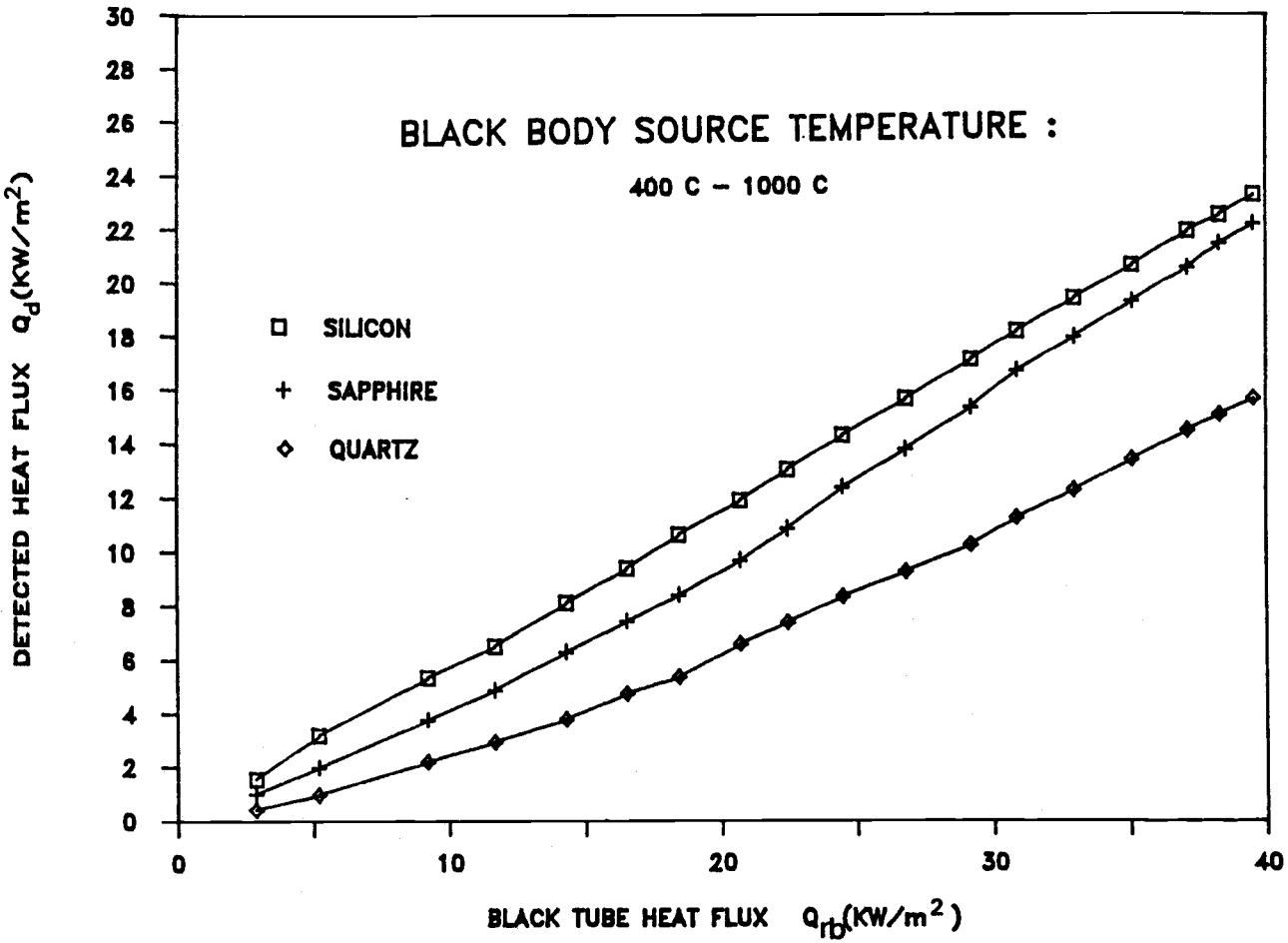

Figure 2.5 Calibration results for different window materials.

Errors of the polynomial regression expression for sapphire is within 1%, and within 2% for quartz. The nonlinear behavior of the calibration curve for quartz is more obvious than for sapphire. This can be explained by their different transmission characteristics with respect to wavelength, as shown in Figure 2.2. Note that the range of wavelengths at which the maximum emissive power occurs is from 2.3 μm to 9.5 μm for the calibration (83). The more concave downward tendency of the quartz curve is due to its lower and varied transmittance with respect to wavelength.

The emissivity of the stainless steel shim covering the total gauge was found to be 0.37. This is the ratio of the heat flux absorbed by a bare tube with that of a black tube.

2.5 Experimental Verification

The experimental apparatus is described in chapter III. Tests were conducted at bed temperatures of 900 K and 1080 K employing ione grain as bed particles with nominal diameters of 2.14 mm and 3.23 mm (9,99). The instrumented tube was placed horizontally 30 cm above the distributor plate and the packed bed height was 45 cm. Measurements were made at 0 and 90 degrees from the lower stagnation point on the tube with superficial velocities (U_o) ranging from well below U_{mf} to about twice this value. A total of 12 channels, 6 for radiative and total heat fluxes and 6 for surface temperatures, were employed for data collection. A total of 50 scans of all channels was made for each run. Values of

the total heat flux measured during this test had no significant use other than to aid in identifying whether the bed was packed or fluidized. At each superficial velocity, time-averaged radiative heat transfer coefficients for a black tube (h_{rb}) were computed from the average of 50 readings of both heat flux and tube temperature over a period of 95 seconds. Detailed procedures for data and heat flux conversions are discussed in section 3.6.3 and Appendix A.

Tabulated results of the experiments are listed in Table C.11 and C.12. The local radiative heat transfer coefficient is calculated as $h_{rb} = Q_{rb} / (T_f - T_w)$. Figures 2.6 through 2.13 display the values of h_{rb} associated with a range of superficial velocities for two bed temperatures and two particles sizes. The local radiative data measured with the radiative detector, employing a silicon window, and the total heat transfer data are found to compare well the results of Alavizadeh (9).

Different results for each window material are evident. Values of h_{rb} for sapphire are 1.056 times the average, ranging from 0.96 to 1.16 of that for silicon, while the quartz data show values 1.93 times the average, ranging from a minimum factor of 1.33 to a maximum of 5.08. The slightly higher values of the sapphire data compared with those of silicon are believed to be due to its slightly higher conduction error as described in section 2.2.3 and listed in

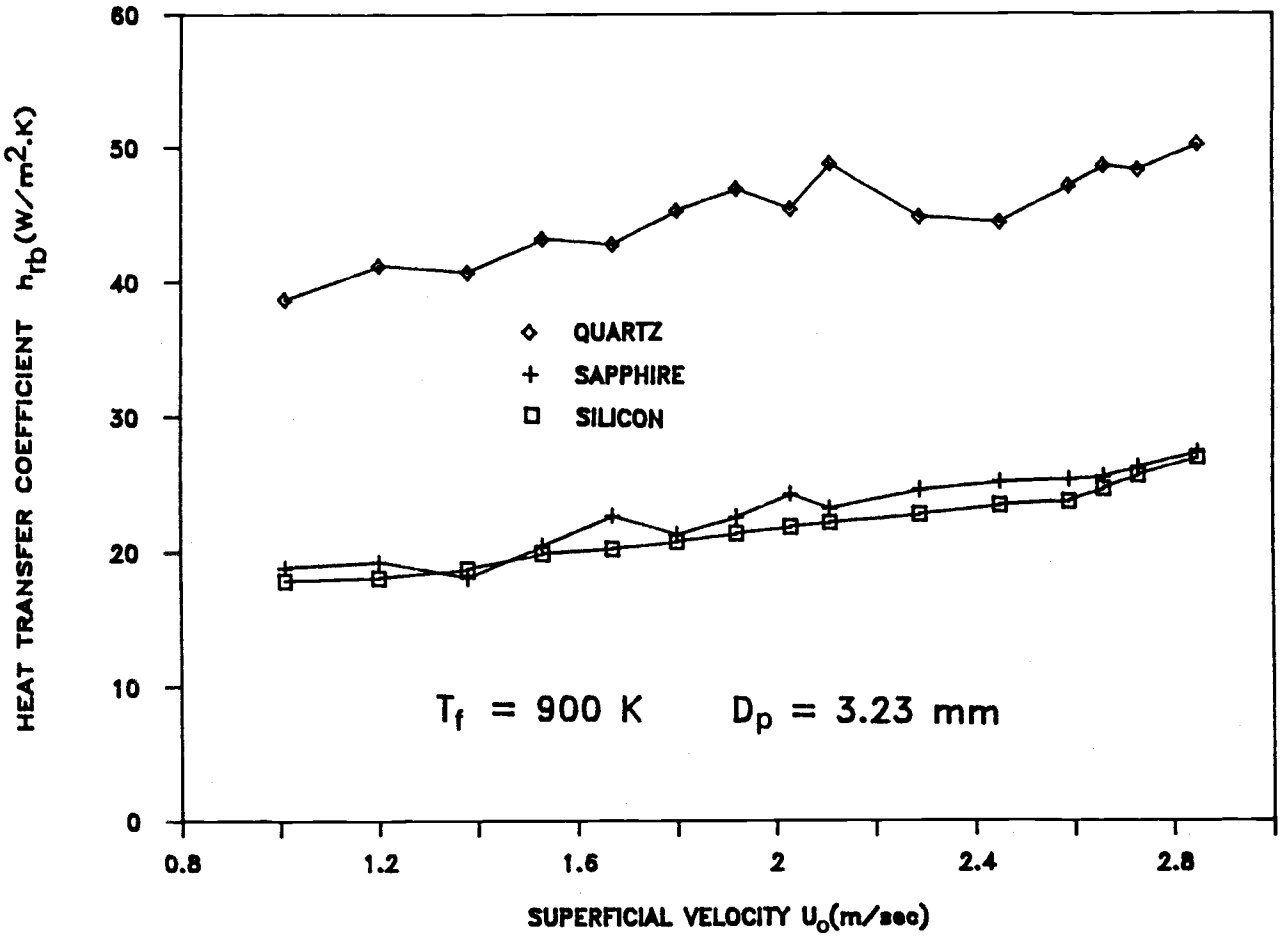

Figure 2.6 h_{rb} vs. U_o at stagnation point for T_f = 900 K, D_p = 3.23 mm.

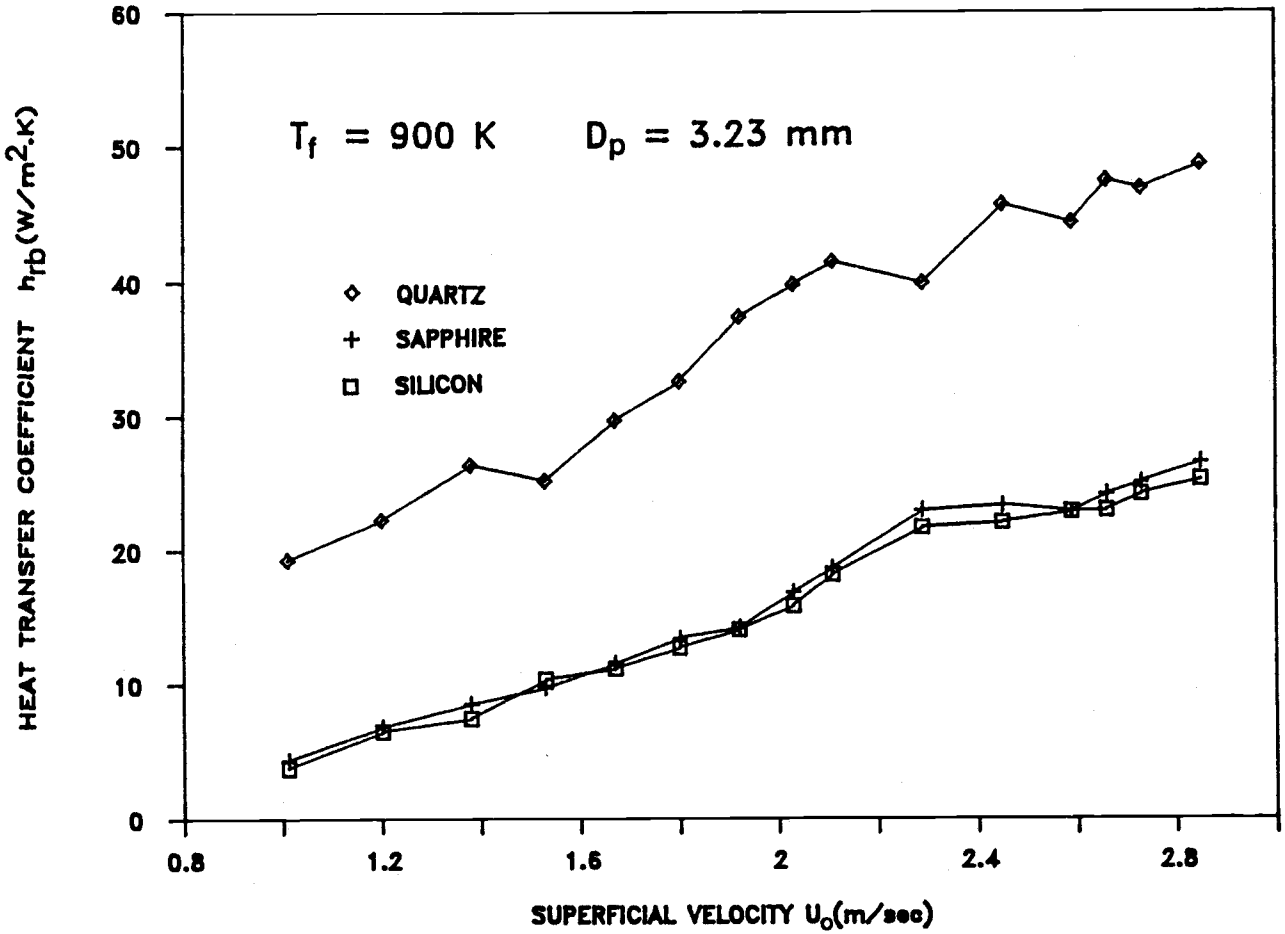

Figure 2.7 h_{rb} vs. U_o at 90 degrees from stagnation point for T_f = 900 K, D_p = 3.23 mm.

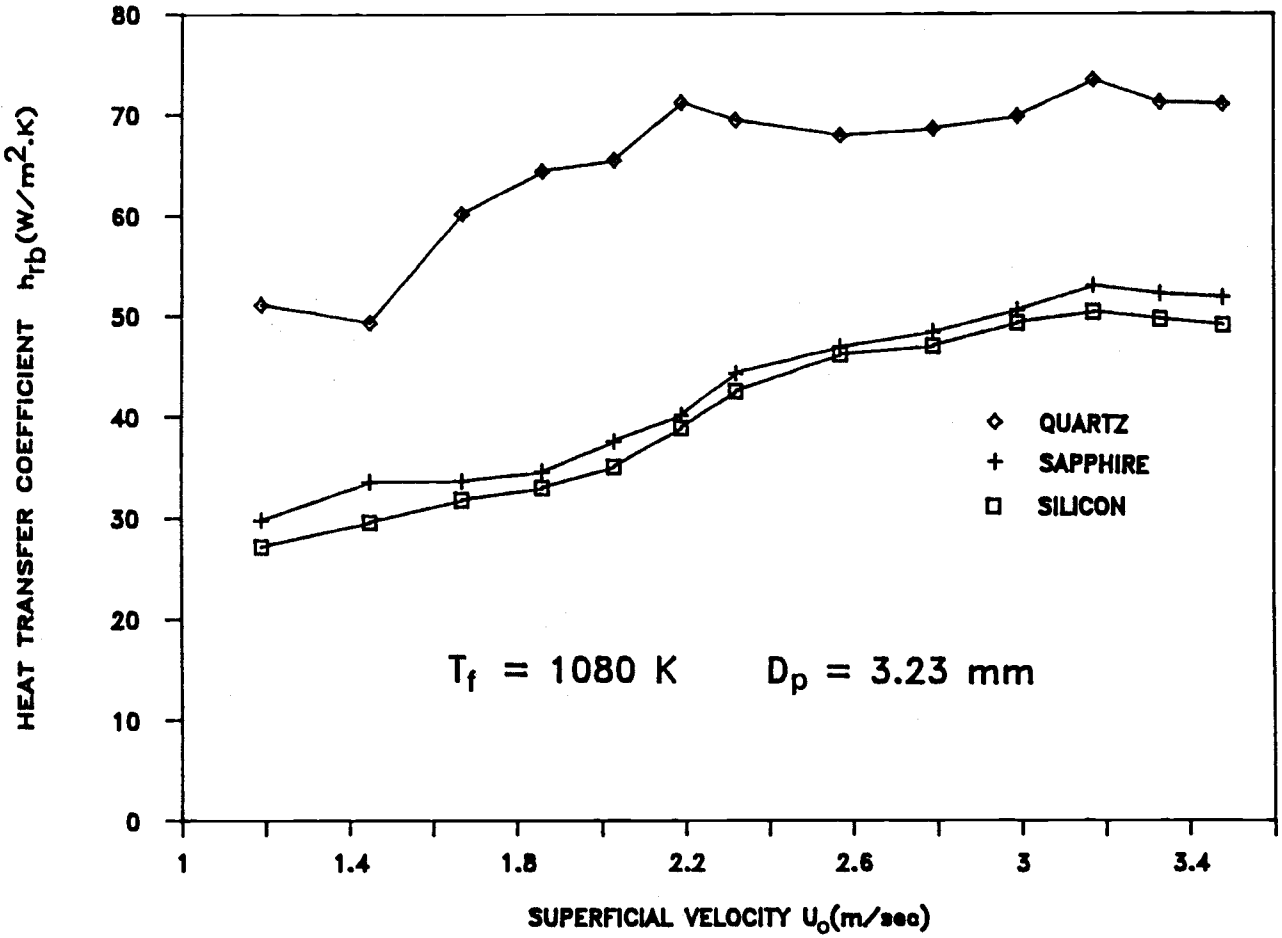

Figure 2.8 h_{rb} vs. U_o at stagnation point for T_f = 1080 K, D_p = 3.23 mm.

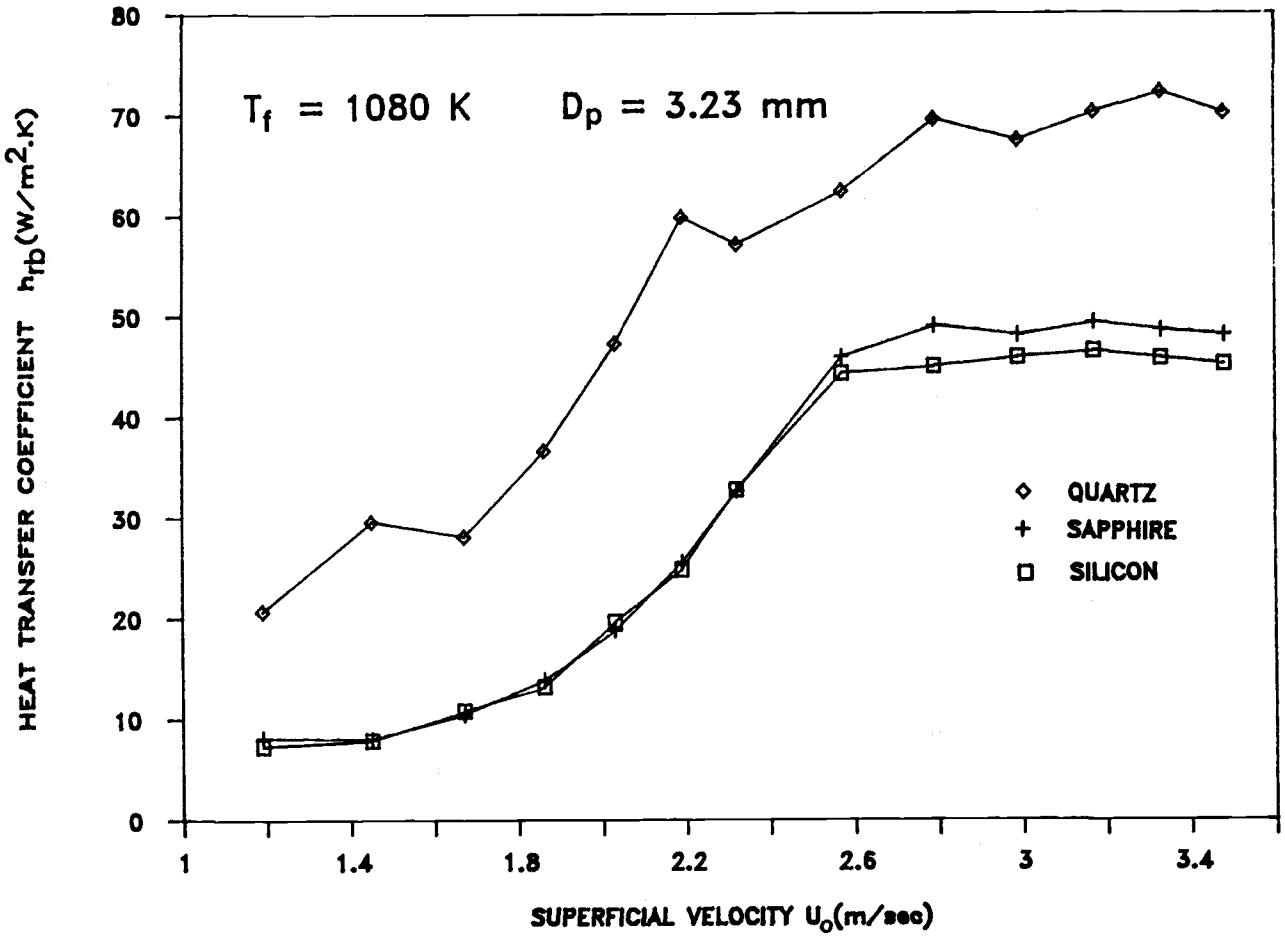

Figure 2.9 h_{rb} vs. U_o at 90 degrees from stagnation point for T_f = 1080K, D_p = 3.23 mm.

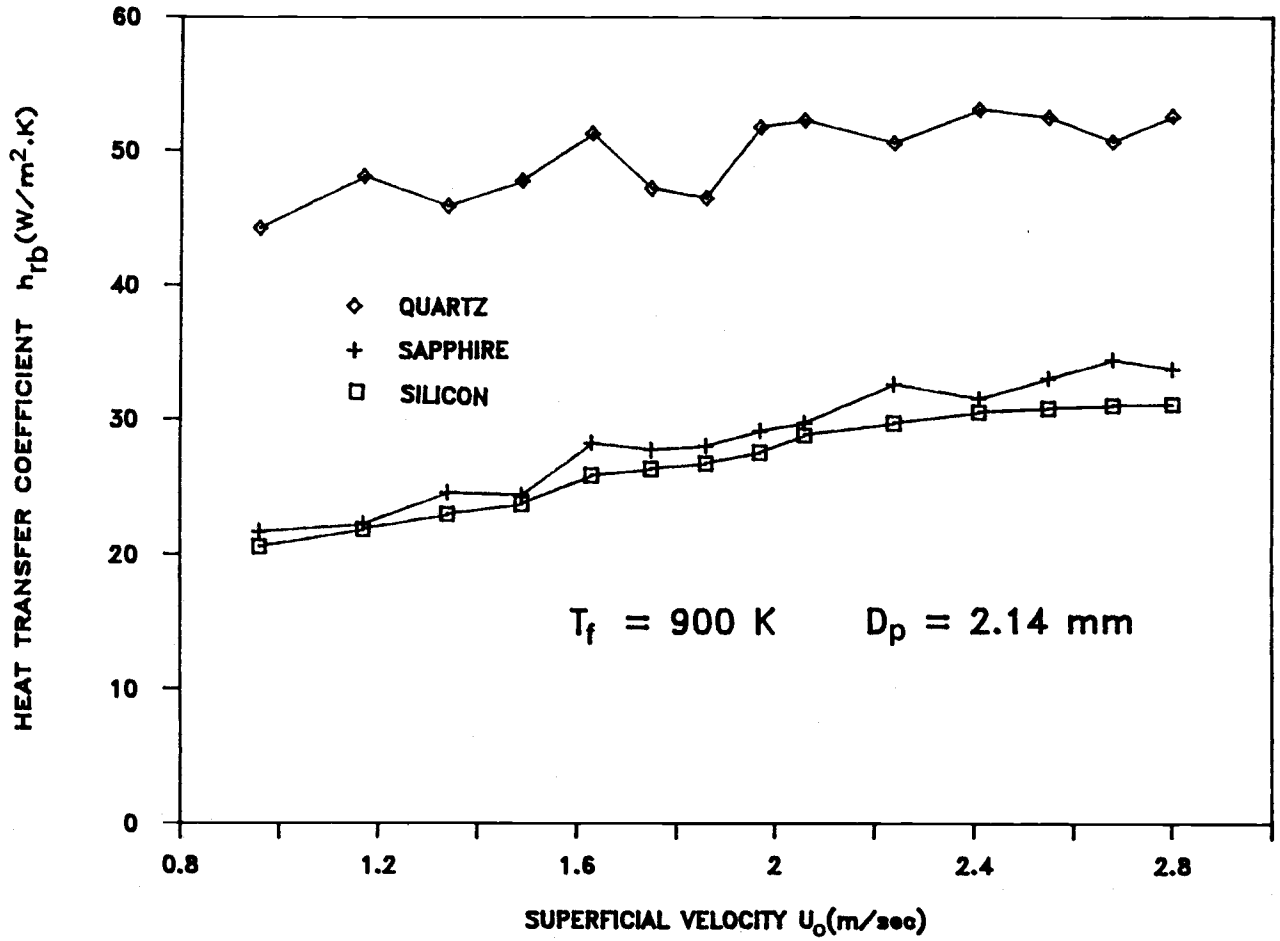

Figure 2.10 h_{rb} vs. U_o at stagnation point for T_f = 900 K, D_p = 2.14 mm.

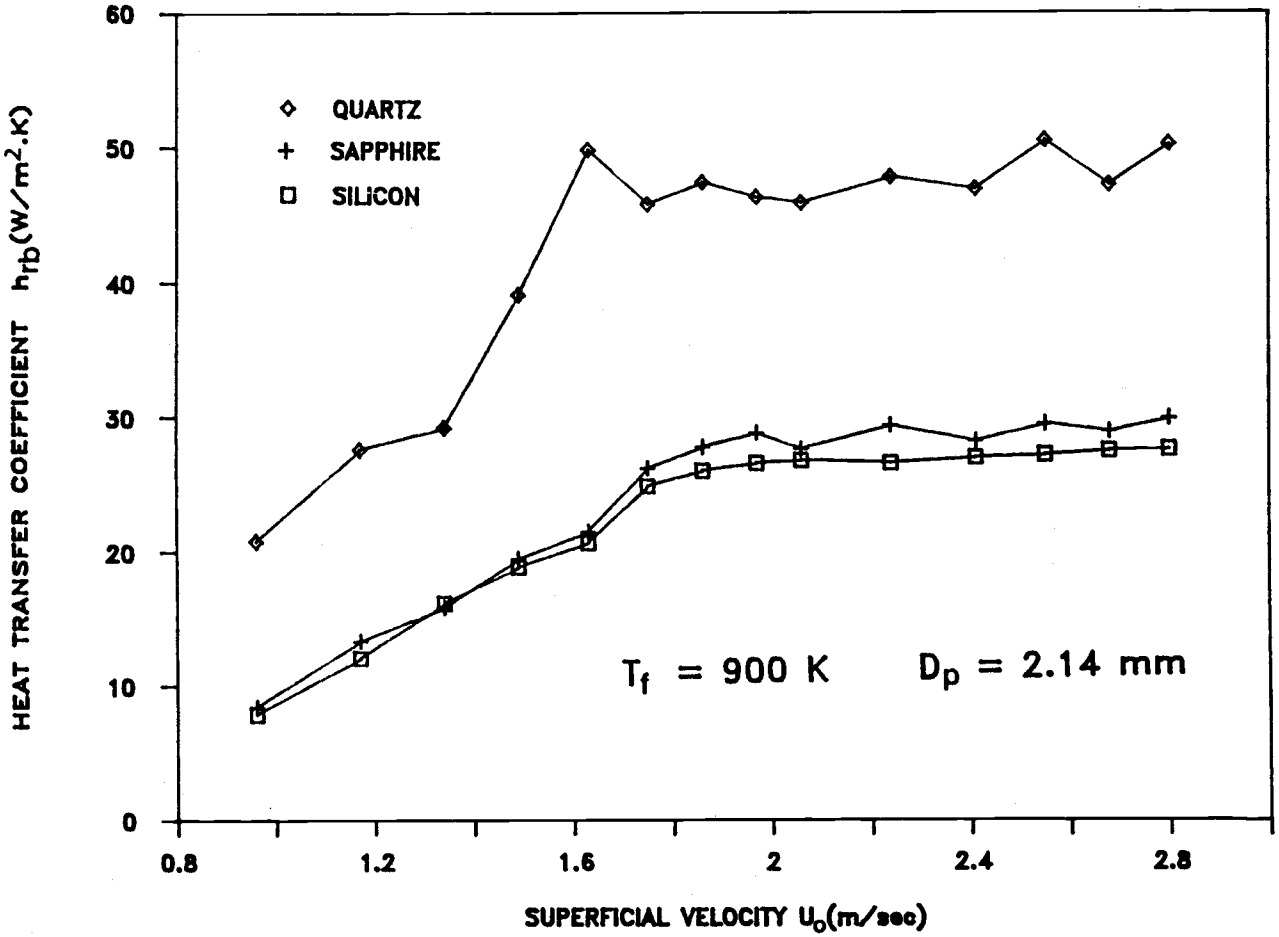

Figure 2.11 h_{rb} vs. U_o at 90 degrees from stagnation point for T_f = 900 K, D_p = 2.14 mm.

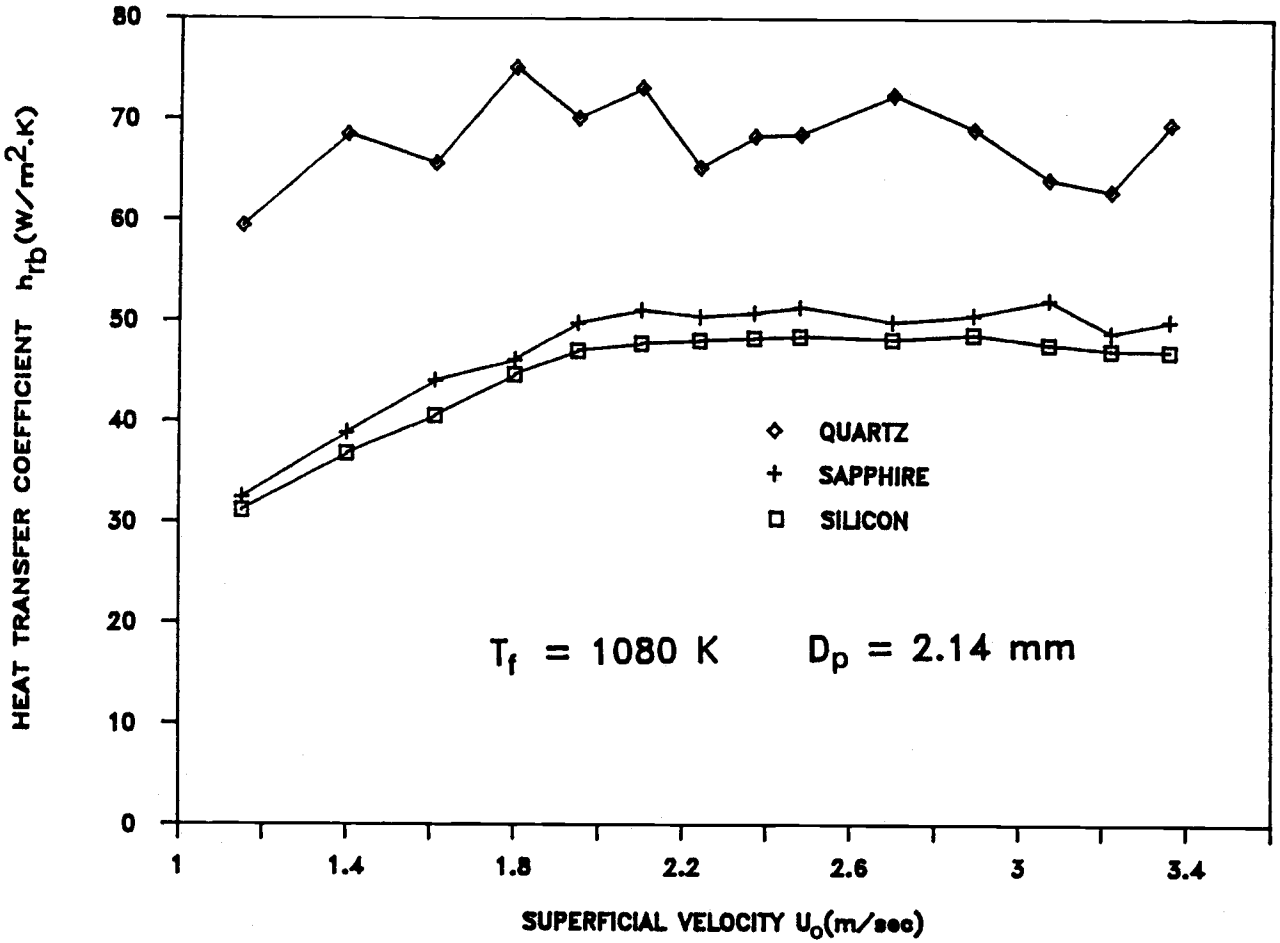

Figure 2.12 h_{rb} vs. U_o at stagnation point for T_f = 1080 K, D_p = 2.14 mm.

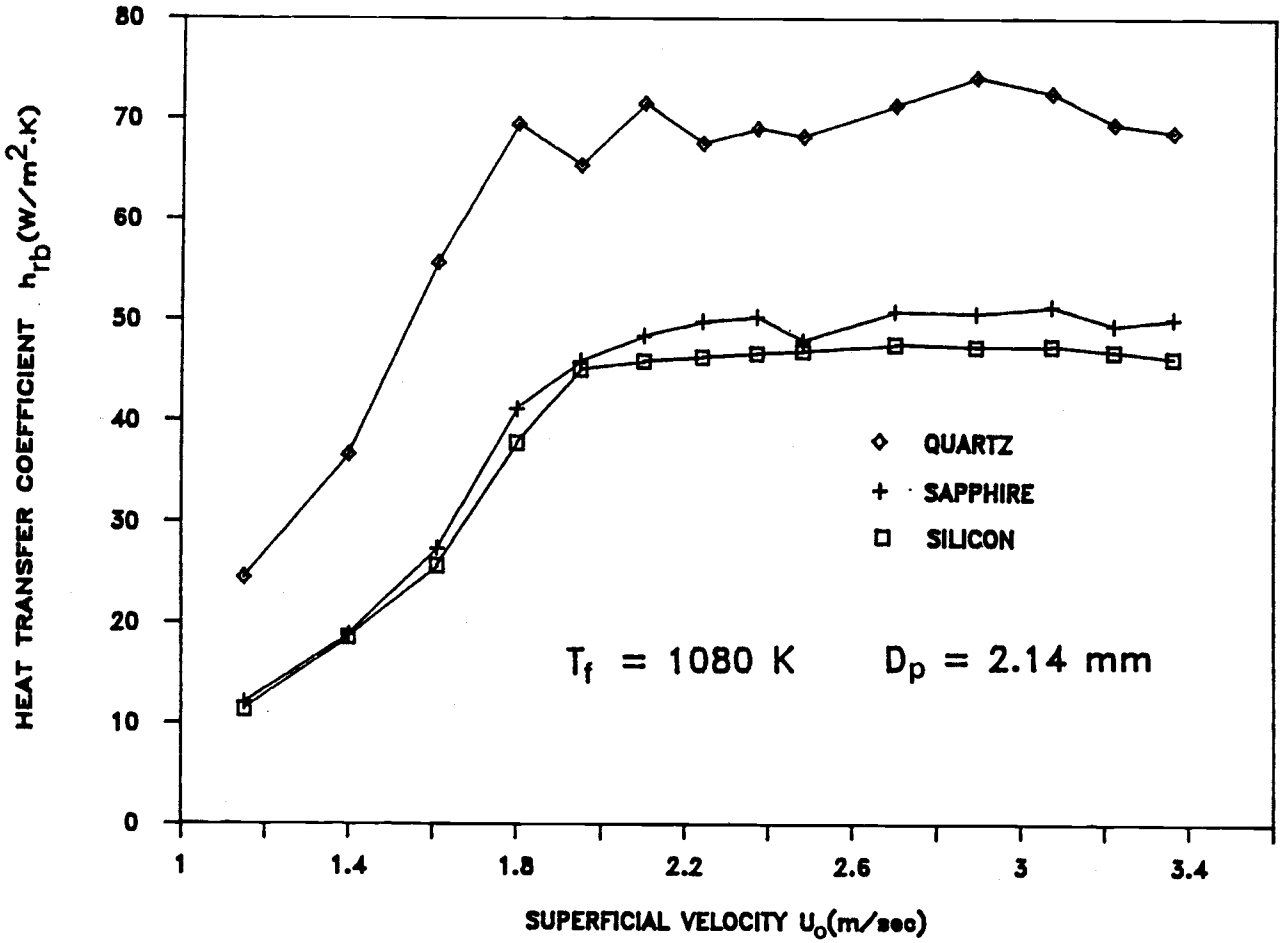

Figure 2.13 h_{rb} vs. U_o at 90 degrees from stagnation point for T_f = 1080 K, D_p = 2.14 mm.

Table 2.2. The extraordinarily high values for quartz are caused by its much higher conduction error, higher window temperature, and flat configuration. The flat configuration resulted in a reduced window thickness of 1/3 and hence, a higher view factor.

For a fused quartz window, the much higher conduction error of these experiments (93%), compared with that obtained by Alavizadeh (28%, Table 2.2), is primarily a result of the assumption of negligible contact resistance between the window and the bronze tube wall in Alavizadeh's analysis. The actual quartz window temperature should be higher than his prediction (9,11); this would, in turn, result in an increase in the conduction error and in the sensor surface temperature. The use of the higher sensor surface temperature, as an approximation of wall temperature, further increases the values of h_{rb} [= $Q_{rb}/(T_f - T_w)$]. The same explanation applies for the small differences (5.6.% to 3%) in the conduction error of sapphire. However, for the window materials with high thermal conductivity, such as silicon (k = 117 W/m.K), the assumption of negligible thermal resistance between the window and tube wall is reasonably valid.

The data for sapphire and quartz also show a fluctuating behavior, as shown in Figures 2.6 to 2.13. These fluctuations are due in part to their nonlinear calibration relationship. The larger fluctuation exhibited by quartz can be explained by its varied and lower transmittance.

It is concluded that the use of silicon as the transmitting medium in the radiative detector instrumentation will lead to accurate and reliable measurements of local radiative heat transfer in high temperature fluidized beds. The small conduction and h_{rb} errors of silicon analyzed by Alavizadeh (9) is confirmed by comparing the silicon data with those of sapphire and quartz.

III. APPARATUS AND EXPERIMENTS

3.1 Instrumented Tube

The instrumented tube, with outside and inside diameters of 51 mm and 32 mm, was made of bronze and equipped with three total and three radiative heat transfer measurement devices. They were mounted side-by-side, each 90 degrees apart, along the axis of the tube. Figure 3.1 shows a schematic illustration of the instrumented tube. The radiation detector, employing silicon as the window material, has been discussed in chapter II. A discussion of the total heat flux gauge and calibration of the radiation detector is presented in this chapter.

3.1.1 Total Heat Flux Gauge

The same type of heat flux sensors as used in the radiation detector were employed and bonded to the tube surface with a Omegabond 200 epoxy. They were then covered by a 0.127 mm thick stainless steel shim to protect them from bed abrasion due to particle motion. The shim was pulled tightly over the sensors and connected to the tube by a clamp, as shown in Figure 3.1. A thin film of Omegatherm 201 was deposited between the sensors and the shim to reduce thermal contact resistance. Similar total gauges were earlier employed by George (66) and Goshayeshi (78).

George (66) analyzed the following effects on the total gauge performance: (a) heat conduction along the shim

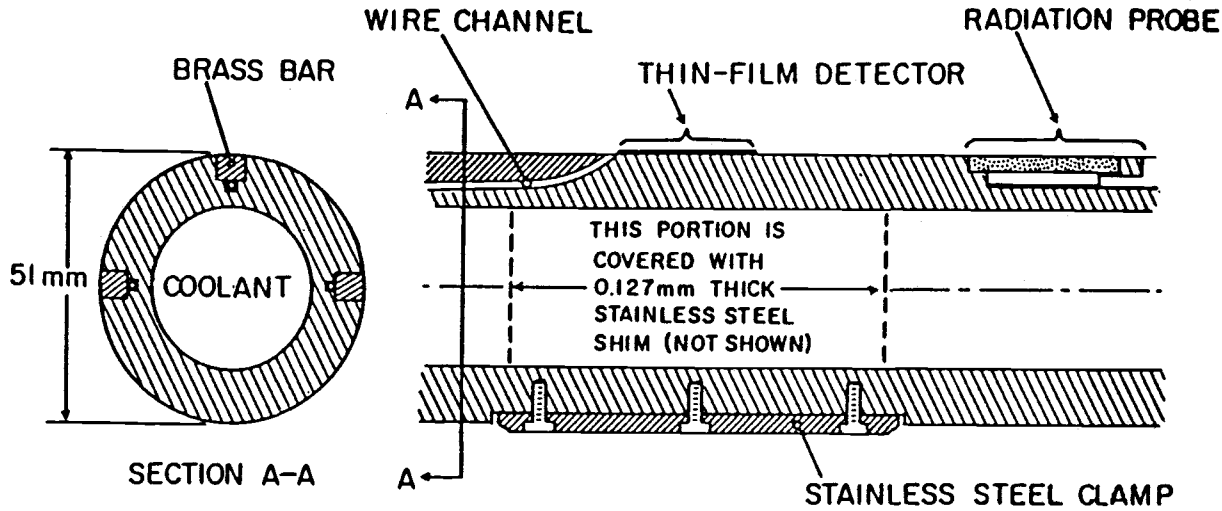

Figure 3.1 Total heat transfer gauges.

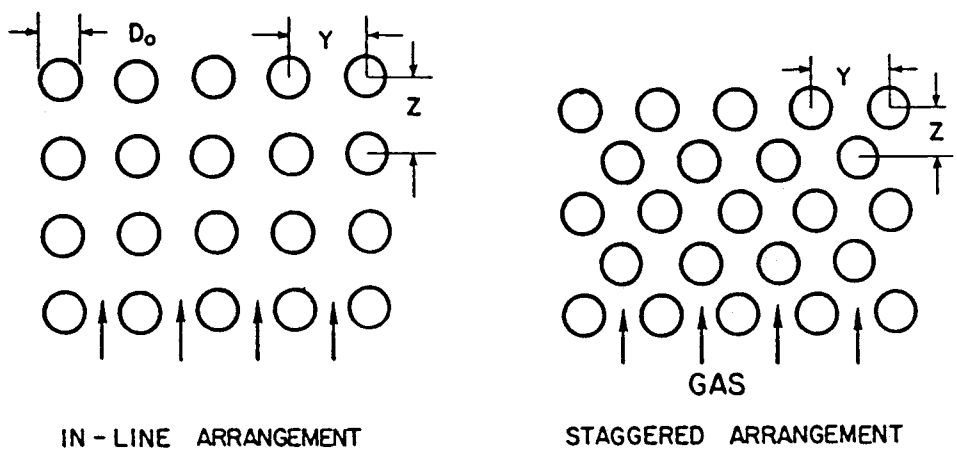

Figure 3.2 Arrangements of tube array design.

surface, (b) disturbance of the thermal boundary layer in the bubble contact region due to nonuniform surface temperature. The reduction in total heat flux measurement was found to be 2% due to the presence of the stainless steel shim, and 4% due to the nonuniform surface temperature. Interested readers may consults George (66) and Appendix B.1 for a detailed discussion. Instantaneous measurement of the total heat flux are not possible due to the gauge's large response time, 0.24 second (66).

3.1.2 Calibration of Radiation Detector

The calibration procedure and setup were described in section 2.4. Calibrations were carried out before and after each exposure to the bed. No significant changes were observed between these times or from the results associated with the first exposure, as reported by Alavizadeh (9). The constants in the linear relationship (Q_d vs. Q_{rb}) are, however, different due to the change of coating material (3M ECP-2200) on the heat flux sensors. Calibration results for the three radiative detectors are:

$$Q_{rb1} = 2.22\ Q_d \qquad (3.1)$$

$$Q_{rb2} = 1.80\ Q_d \qquad (3.2)$$

$$Q_{rb3} = 1.94\ Q_d \qquad (3.3)$$

The quantity, Q_d, was taken as the average of the measurements on all three total gauges. The maximum deviation was 3% at low temperatures (400-600 ^{o}C) and within

1.2% in high temperatures (600-1000 ^{o}C) where the actual interest lies.

3.2 Tube Array Design

In the horizontal tube array design, the tube bundles are generally arranged in either in-line or staggered arrays, as shown in Figure 3.2. Extensive studies have been made regarding the influence of tube spacing on the heat transfer in fluidized beds, as reviewed by Saxena, et al. (122). A P/D_o (pitch/tube diameter) ratio is used in the evaluation of tube spacing. For tube arrays with the in-line arrangement, P is taken equal to the horizontal pitch (Y). For staggered arrays, P is taken as the minimum distance between centers of the adjacent tubes.

The following considerations were made in the tube array design: (a) comparisons of performance of in-line and staggered arrays, (b) influence of P/D_o ratio, and (c) minimum height required between the bottom of tube array and the distributor plate. Theoretically, adjacent tubes were found to increase the heat transfer due to increases in the local interstitial gas velocity. Welty (138) investigated the effect of tube spacing on the heat transfer performance of the Adams-Welty model in large particle (D_p = 4 mm) fluidized beds. A horizontal spacing of 1.5 diameter and a vertical spacing of 3 diameters were determined to provide the most effective heat transfer characteristics. Peeler and Whitehead (115) studied the solids motion around horizontal

tubes immersed in large particle fluidized beds. A P/D_o ratio of larger than 2 is recommended. Borodulya and Ganzha (25) suggested staggered arrays on the basis of their experimental results.

A staggered, equilateral triangular tube array arrangement was selected due to its superior fluidization and heat transfer characteristics (64,127,138). A P/D_o ratio of 3 was chosen in order to allow sufficient particle motion and avoid the decrease in heat transfer performance for cases with P/D_o much lower than 2 (8,25,82,110). The distance from the distributor plate to the bottom of tube array was chosen as 30 cm for the purpose of preventing irregular fluidization at the bottom row (110,127,141).

An array of 9 tubes, made of bronze each with a diameter of 51 mm, arranged in three horizontal rows, was used. This arrangement, as shown in Figure 3.3, is the most common in-bed tube design in industrial fluidized bed combustors (78). Studies (17,38,110) have shown that the heat transfer coefficient to individual tubes inside such an array does not vary significantly with their position. The instrumented tube was, thus, placed in the center of the 9 tubes, to present a typical tube in an actual, large-bed array.

3.3 Data Acquisition System

A high precision digital data acquisition system (HP-3497A) with a maximum sensitivity of 0.001 microvolt was

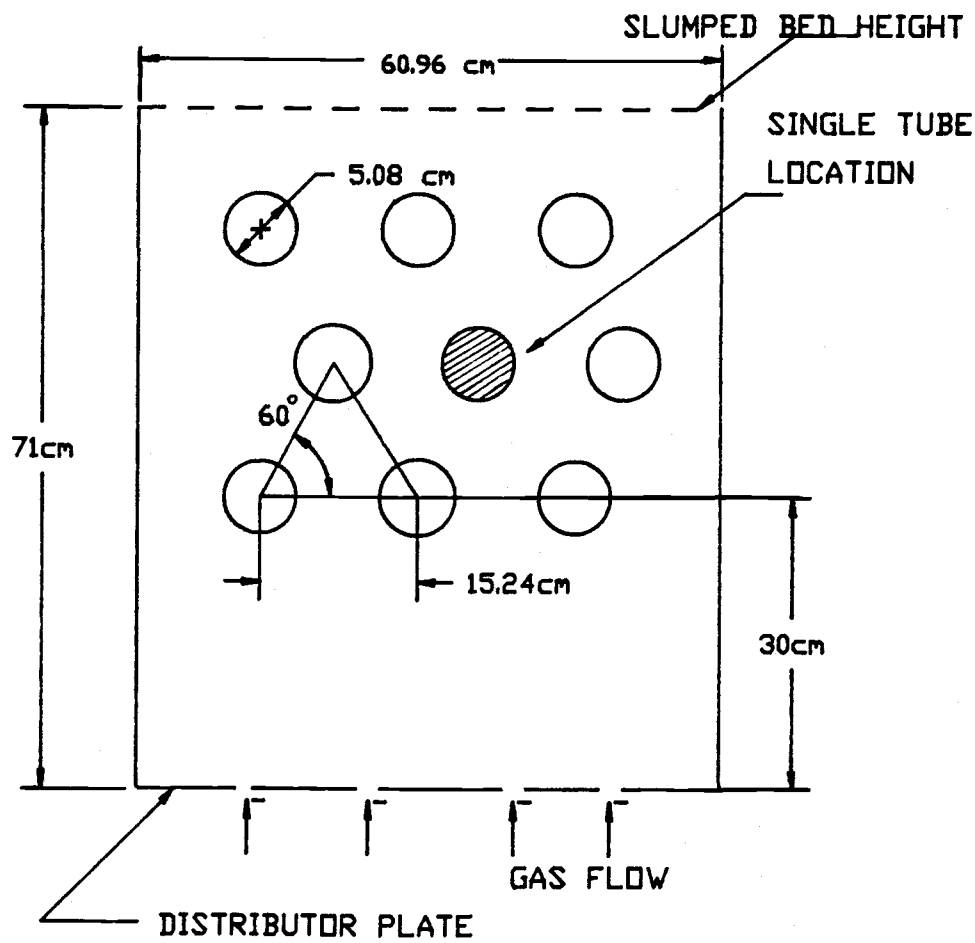

Figure 3.3 Tube array geometry.

used to measure the signals from the heat flux sensors. By using an HP-85 microcomputer connected with an HP-IB interface card and a dual disk drive (HP-83901M) as the control unit, the raw data in microvolts were taken with an HP-3497A data logger and transferred to diskettes by commands resulting from locally-developed software. Figure 3.4 is a schematic diagram of the data acquisition system used in this study. A quick user's manual for the application of the data logger employed in the present study is provided by Alavizadeh (10). A total of 12 channels, 6 for local radiative and total heat flux, and 6 for surface temperature, were employed during the experiments. The software allows for the scan time of all 12 channels to be a minimum of 1.2 seconds.

The time-averaged local surface temperatures and heat transfer coefficients were computed from the raw data. Several programs, written in BASIC language, were developed and employed in data collection, data reduction, and computation of the superficial velocity.

3.4 Fluidized Bed Facility

All experiments were conducted in the Oregon State University high-temperature fluidized bed facility. A detailed design, construction, and operation information of the facility is covered by Junge (93) and Welty (137). A discussion of different components and operating procedure is provided by Alavizadeh (9), George (66,67), and Gosmeyer

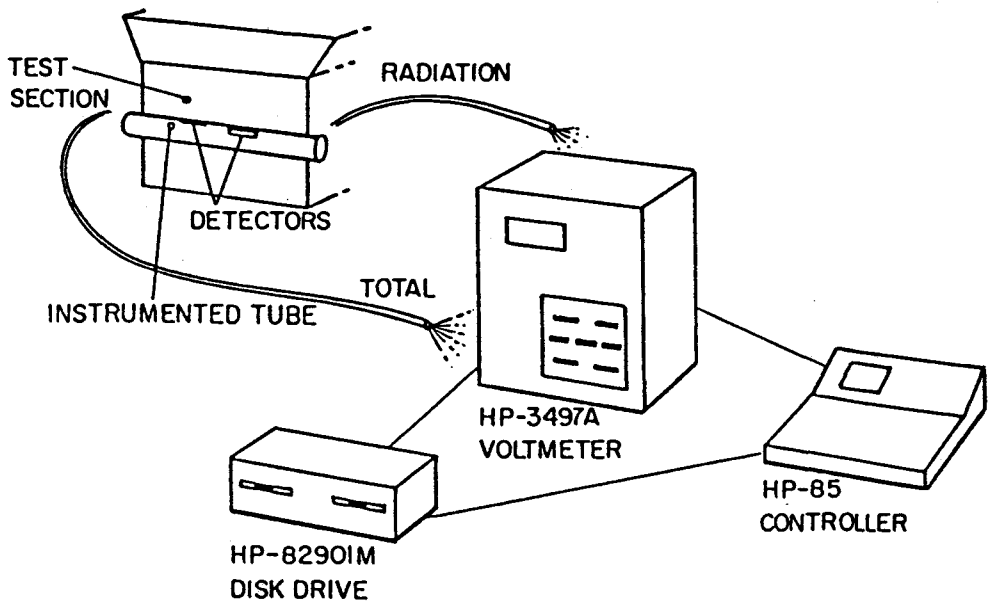

Figure 3.4 Data acquisition system.

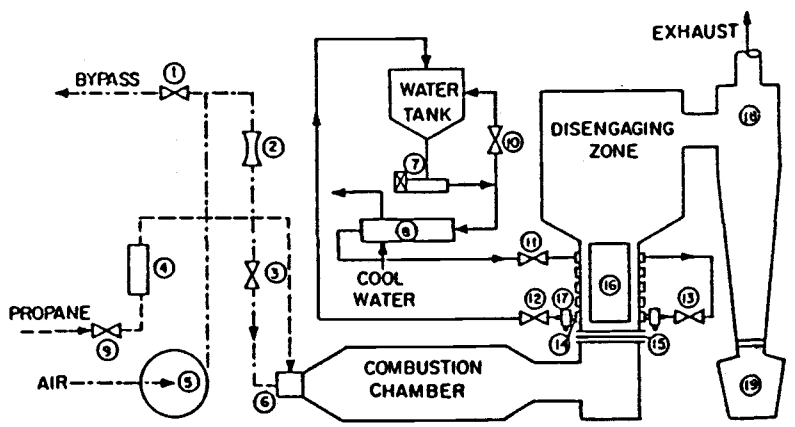

Figure 3.5 Oregon State University high temperature fluidized bed facility.

(76). A schematic of this facility is included as Figure 3.5. The following discussion gives a brief description of the principal components and their functions. The numbers in the brackets stand for the components shown in Figure 3.5.

3.4.1 Air and Fuel

Combustion air was compressed and introduced into the system using an air blower [5] driven by a 30 Hp electric motor. The flow rate and pressure of the inlet air were controlled by an air inlet valve [3] and a by-pass valve [1]. The venturi meter [2] was used to measure the flow rate of inlet air. Calibration of the venturi meter was provided by Gosmeyer (76). Propane was fed into the burner [6] by the main fuel valve [9] and burned in the refractory-lined combustion chamber. The products of combustion were then directed to the bed test section through the inconel gas distributor [15]. No combustion occurred in the bed itself.

3.4.2 Test Section

The test section [16], as previously described by Goshayeshi, et al. (78), has a 30 cm x 60 cm interior with 15.2-cm-thick refractory-lined walls. A total of 15 mounting ports were built in the test section (3 columns x 5 rows) to accommodate both tube arrays and a single tube. This arrangement also provided the ability to investigate the effect of bed height on the heat transfer performance. The gas distributor consisted of 2 inconel 601 plates with a

stainless steel (ASTM 316) 16-mesh screen in between. The upper plate contains 171 (19 x 9) holes, with a diameter of 6.35 mm, in an in-line array pattern (57.15 mm x 25.4 mm in area). The lower plate is identical to the upper one except it has 9.53-mm-diameter holes. A rotary union [17] was used to adjust the instrumented tube [14] to a desired angular position for data collection. Particles were prevented from leaving the bed through the disengaging zone and the cyclone [18]. A view port located on top of the disengaging zone was used to monitor the bed's operation condition.

3.4.3 Temperature Control

Bed temperature was monitored and automatically controlled to the set temperature by two type K (chromel-alumel) thermocouples and an electronic fuel flow rate controller. A manual by-pass fuel valve and a fuel flow rotameter [4] were provided to assist in establishing the desired bed temperature at higher superficial velocities.

All tubes were cooled and maintained at the desired temperature by adjusting the flow rate of water, circulating through the tubes in a closed loop by a 2.2 kW centrifugal pump [7]. The instrumented tube temperature, which was monitored by the data acquisition system with software control, was held below 450 K to prevent damage to the heat flux sensors. The temperature of the circulating water was adjusted either by the water flow valve [7] or by the shell

and tube heat exchanger [8] with city water as a secondary coolant.

3.5 Bed Particles

The range of nominal particle diameters for fluidized bed combustors is generally between 0.37 mm and 4.1 mm (40). A commercialized granular refractory material, ione grain, with mean diameters of 2.14 mm and 3.23 mm, was used as the bed material. The mean particle diameter was calculated by Alavizadeh (9) from the equation suggested by Kunii and Levenspiel (99).

$$D_p = 1 \; / \; \sum_{j=1}^{M} (x_j / D_{pj}) \qquad (3.4)$$

In this expression, x_j is the mass fraction of ione grain particles in size interval j, as shown in Table 3.1. Also shown is the particle material chemical composition given by the supplier (Intepace Corp., Portland, OR) and its thermal properties measured by Ghafourian (68). The size distribution of bed particles remained stable after many hours of operation (9).

3.6 Experiments

3.6.1 Test conditions and Procedure

For 2.14mm particles, experiments were conducted at bed temperatures of 812 K, 925 K, and 1000 K, also at 812 K and 925 K for 3.23 mm particles. Both tube arrays and the single

Screen Number	Opening Diameter (mm)	Mass Fraction (x_i) D_p = 2.14 mm (%)	Mass Fraction (x_i) D_p = 3.23 mm (%)
4	4.76	0.16	-
5	4.00	0.28	8.8
6	3.36	0.61	36.8
8	2.38	36.5	54.4
10	2.00	36.92	-
12	1.68	19.33	-
16	1.19	4.66	-
pan	0.00	1.54	-

ρ_p (Particle Density) : 2700 kg/m^3

Chemical Composition : 53.5% silica
43.8% alumina
2.3% titania
0.4% other

Thermal Properties :

C_{ps} = .853 - .982 kJ/kg.K (for 470 - 900 K)

k_p = 1.1 - 1.41 W/m.K (for 494 - 833 K)

ϵ_p = .855 - .874 (for 279 - 452 K)

Table 3.1 Size distribution, chemical compositions, and thermal properties of ione grain.

tube cases were included with exception of the single tube case at 812 K, which had been performed by Alavizadeh (9). The single tube results represent a reference to investigate the effects of adjacent "cool" tubes on the heat transfer performance of the tube arrays case. A summary of the test conditions is shown in first two columns of Table 4.1.

An array of 9 tubes with the instrumented tube in the middle was placed at the lowest position in the test section. The bottom row of the tube array was located 30 cm above the distributor plate and the slumped (packed) bed height was 71 cm, as shown in Figure 3.2. Also shown is the single (instrumented) tube location.

The start up sequence of the fluidized bed facility and test procedures were previously described by Junge (93) and Alavizadeh (9) respectively. The minimum fluidization condition was estimated by visual observation of the bed and verified by later analysis of total heat transfer data.

3.6.2 Data Collection

Data were collected first at the maximum possible superficial velocity, then at other different velocities in a descending sequence. The bed temperature was controlled within ±12 K of the set temperature by adjusting the fuel by-pass valve during each data collection period.

Data were taken at 0^{o}, 45^{o}, 90^{o}, 135^{o}, and 180^{o} from the lower stagnation point on the tube with superficial velocities ranging from below U_{mf} to approximately twice

this value; thus, most of the data were in the bubbly-bed regime. Twelve pieces of data, 3 for radiation, 3 for total heat flux, and 6 for tube surface temperatures, were collected in each scan. The minimum scanning time of 1.2 seconds was employed and a total of 150 scans with approximate total time of 180 seconds were made for each superficial velocity. This made full use of the computer-controlled data acquisition system.

Recorded data also included particle diameter, air inlet pressure and temperature, pressure drop across the venturi meter, and bed temperature for the purpose of computing gas flow rate as shown by Gosmeyer (76) and Alavizadeh (9). The gas superficial velocity is equal to the gas flow rate divided by the cross section area of the test section.

3.6.3 Data Reduction

Heat Flux

Conversion of raw data to time-averaged local radiative flux and total heat flux was carried out first by converting raw signals in microvolts to sensor surface temperatures using equation (A.1). The detected heat flux was then computed using equation (A.2). A detailed discussion of the conversion procedure is presented in Appendix A.

The time-averaged local heat transfer rates (Q_{rb} and Q_t) and tube temperature (T_w) were obtained according to:

$$Q \text{ (or } T_w) = \frac{1}{N} \sum_{i=1}^{N} Q_i \text{ [or } (T_w)_i] \qquad (3.5)$$

Where N = 50 for the experiments in chapter 2.

N = 150 for the experiments in chapter 4.

i = refer to each reading.

The spatial-averaged heat transfer rates ($\bar{Q}_{rb}$ and $\bar{Q}_t$) were calculated using the trapezoidal rule in the form

$$\bar{Q} = \frac{1}{8} [Q(\alpha=0^o) + 2Q(\alpha=45^o) + 2Q(\alpha=90^o) + 2\,Q(\alpha=135^o) + Q(\alpha=180^o)] \qquad (3.6)$$

The black tube radiative heat flux (Q_{rb}) was obtained from the detected heat flux employing the calibration data, equations (3.1) to (3.3). The actual radiative heat transfer rate, Q_r, could then be evaluated from the measured tube wall emissivity with the grey body assumption

$$Q_r = \epsilon_w Q_{rb} \qquad (3.7)$$

Heat Transfer Coefficient

Local heat transfer coefficients (h_{rb} and h_t) were computed by

$$h = \frac{Q}{T_f - T_w} \qquad (3.8)$$

The temperatures obtained from the total heat flux gauges and radiation detectors were used as approximations

for tube wall temperature (T_w) in equation (3.8). George (66) computed the temperature drop across the stainless steel shim on the total gauge to be less than 1.8 K, which represented 0.3% of the bed-to-tube surface temperature difference. Also from the conduction analysis and experiments of Alavizadeh (9), it was determined that these approximations introduce negligible error.

The spatial-averaged heat transfer coefficients ($\bar{h}_{rb}$ and $\bar{h}_t$) were calculated from local values as

$$\bar{h} = \frac{1}{8}\left[h(\alpha=0^o) + 2h(\alpha=45^o) + 2h(\alpha=90^o) + 2h(\alpha=135) + h(\alpha=180^o)\right] \qquad (3.9)$$

Radiation Contribution

The black tube radiation contribution (f) to total heat transfer is determined by;

$$f\ (\%) = \frac{\bar{Q}_{rb}}{\bar{Q}_t + (1-\epsilon_w)\bar{Q}_{rb}} \qquad (3.10)$$

Where $(1-\epsilon_w)Q_{rb}$ compensates for the spatial averaged total heat flux (Q_t) which was obtained on the nonblack tube with an emissivity of ϵ_w. The value of ϵ_w was found to be 0.37 for the stainless steel shim which covered the total heat flux gauge, and a value of 0.64 was used by Alavizadeh (9). The reason for this difference is that the stainless steel shims were polished by sand paper in the present study, reducing its emissivity (125,140). This change will

have no effect on the calculation of black tube radiative heat transfer.

Errors

A RSS (Root-Sum-Square) random error of ±8%, due to calibration of the heat flux sensor and experimental data acquisition, was calculated for the local total heat flux (Q_t) measurements. The error in local radiative heat flux (Q_{rb}) measurements was ±9%. The larger error for the radiation measurements was a result of the additional local calibration procedure with the radiation detector.

The overall errors estimated in the local total and radiative heat transfer coefficients (h_{rb} and h_t) reported in this study were found to be +8%, -14% and +12.5%, -11.5% respectively. Detailed calculations and a discussion of the error estimation can be found in Appendix B. Note that both actual RSS random and overall errors are always below the estimated values which are obtained by the maximum values of all possible variations combined.

IV RESULTS AND DISCUSSION

Experimental results for all test conditions are tabulated in Appendix C (Table C.1 through C.10). The radiative heat transfer results ($\bar{h}_{rb}$ and h_{rb}) for tube arrays immersed in a large-particle bed are believed to be the first of their kind. Note that all radiative heat transfer coefficients and radiation contribution in percentage (f) reported in this study were calculated for a black tube wall ($\epsilon_w = 1.0$). The actual radiative values can be obtained from equation (3.7).

Table 4.1 summarizes the test conditions and highlights some of the findings of the present work. The minimum fluidization velocity (U_{mf}) corresponds to the transformation of a packed to a bubbly bed. The optimum superficial velocity (U_{op}) is the fluidizing velocity at which the total heat transfer coefficient approaches a maximum ($\bar{h}_{max}$). This is of great importance in designing fluidized bed combustors since they are expected to have a maximum heat transfer rate under normal operation condition. Also shown in Table 4.1 are the corresponding radiative values, $\bar{h}_{rb}$ and f at $\bar{h}_{max}$, where f is the radiation contribution, in percentage, calculated from equation (3.10).

D_p (mm)	T_f (K)	U_{mf} (m/s)	U_{op} (m/s)	At $\bar{h}_{max}$: $\bar{h}_{max}$ (W/m^2.K)	At $\bar{h}_{max}$: $\bar{h}_{rb}$ (W/m^2.K)	At $\bar{h}_{max}$: $f(\epsilon_w=1)$ (%)
2.14	812(A*)	1.60	2.09	181	21	11.8
	812+(S#)	1.62	1.85	189	21.9	12.3
	925(A)	1.64	2.15	193	27.5	13.5
	925(S)	1.65	2.15	205	32.1	15.5
	1000(A)	1.73	2.17	200	28.4	14.3
	1000(S)	1.71	2.02	217	37.3	17.2
3.23	812(A)	2.30	2.68	178	20.7	11.9
	812+(S)	2.31	2.62	184	24.0	13.8
	925(A)	2.32	2.68	183	24.6	13.5
	925(S)	2.33	2.61	196	31.5	16.4

* Stands for tube array # Stands for single tube
\+ Data from Alavizadeh (9)

Table 4.1 Test conditions and results at optimum superficial velocity.

Test Conditions		Reductions (%)		f_{ave} (%)	
D_p (mm)	T_f (K)	$\bar{h}_t$	$\bar{h}_{rb}$	Array	Single
2.14	812	6	9	12.2	13.1*
	925	7	14	14.1	16.1
	1000	8	22	14.8	18.0
3.23	812	6	15	12.0	13.5*
	925	6	21	13.8	16.9

* Data from Alavizadeh (9)

Table 4.2 Overall radiation contribution and heat transfer coefficient reduction in the bubbly-bed state.

4.1 Spatial Average Heat Transfer

Results of the spatial-averaged radiative and total heat transfer coefficients with respect to superficial velocity are presented for both tube arrays and a single tube case. The discussion will include the effects of superficial velocity, bed temperature, particle size, and adjacent "cool" tubes on both the radiative and total heat transfer performance. Also discussed in section 4.1.1 are the radiation contributions under different test conditions. Comparisons are made between the results of the present study and those reported in the literature.

4.1.1 Radiative Heat Transfer

The variations in the spatial-averaged radiative heat transfer coefficient ($\bar{h}_{rb}$) as a function of superficial velocity (U_o) are shown in Figures 4.1 and 4.2, for both the tube array and the single tube cases respectively, with a particle diameter of 2.14 mm, at three different bed temperatures (812 K, 925 K, and 1000 K). Results for the 3.23 mm particle at two different bed temperatures (812 K and 925 K) are shown in Figures 4.3 and 4.4. Comparisons of the radiative values between the tube arrays and the single tube at different bed temperatures are illustrated in Figures 4.5 and 4.6, for 2.14 mm and 3.23 mm particles respectively.

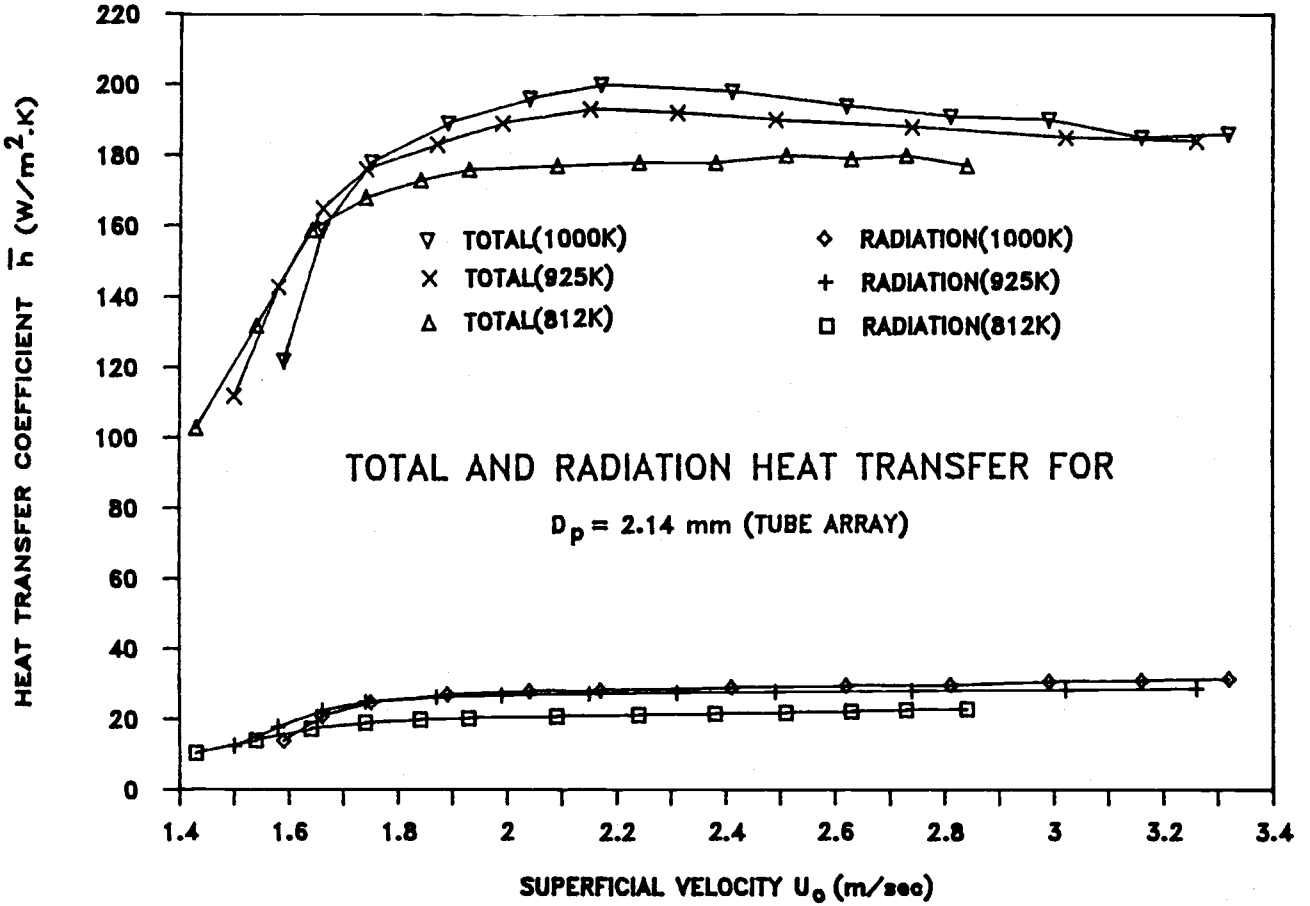

Figure 4.1 $\bar{h}_{rb}$ and $\bar{h}_t$ vs. U_o for D_p = 2.14 mm (Tube Array).

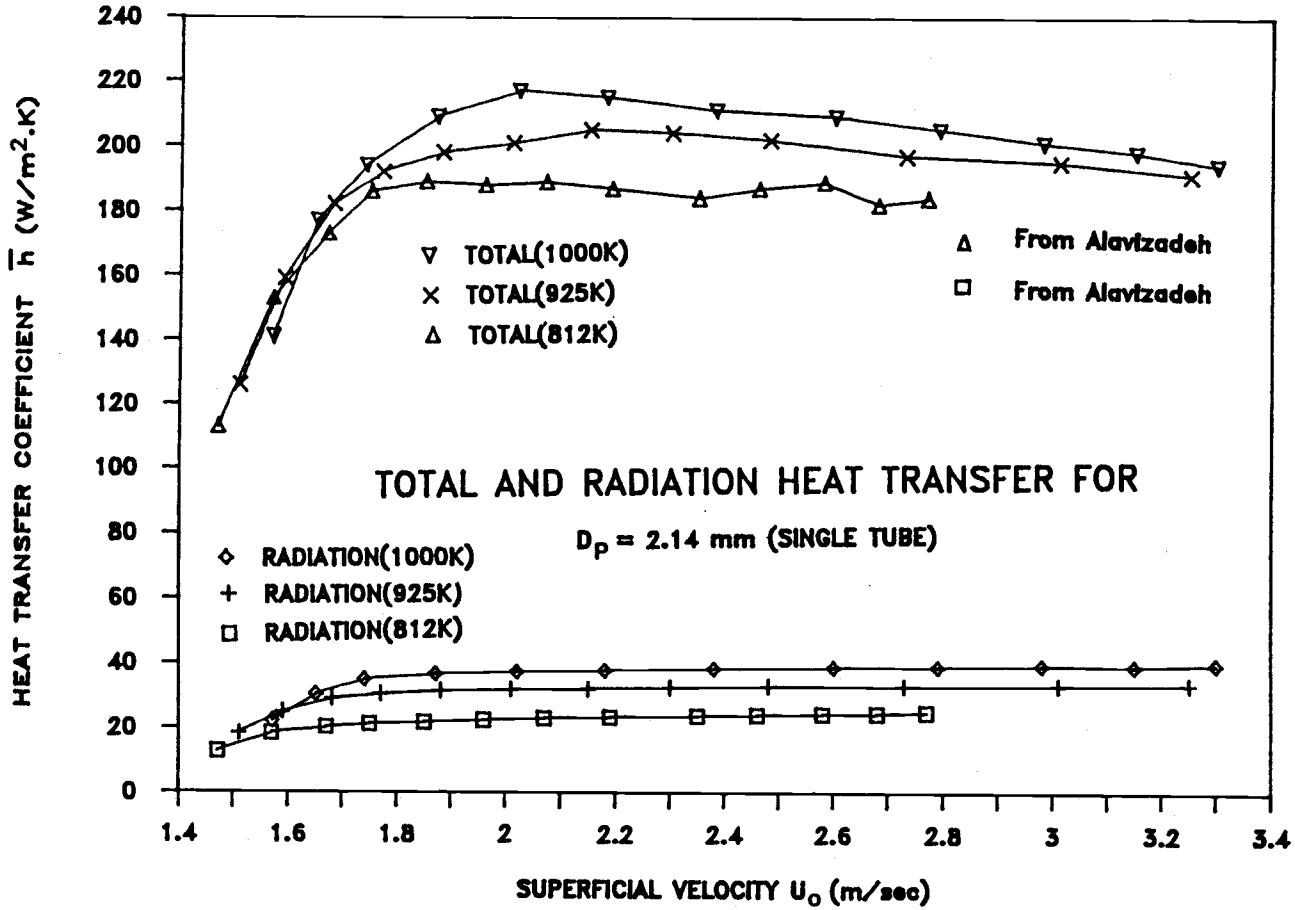

Figure 4.2 $\bar{h}_{rb}$ and $\bar{h}_t$ vs. U_o for D_p = 2.14 mm (Single Tube).

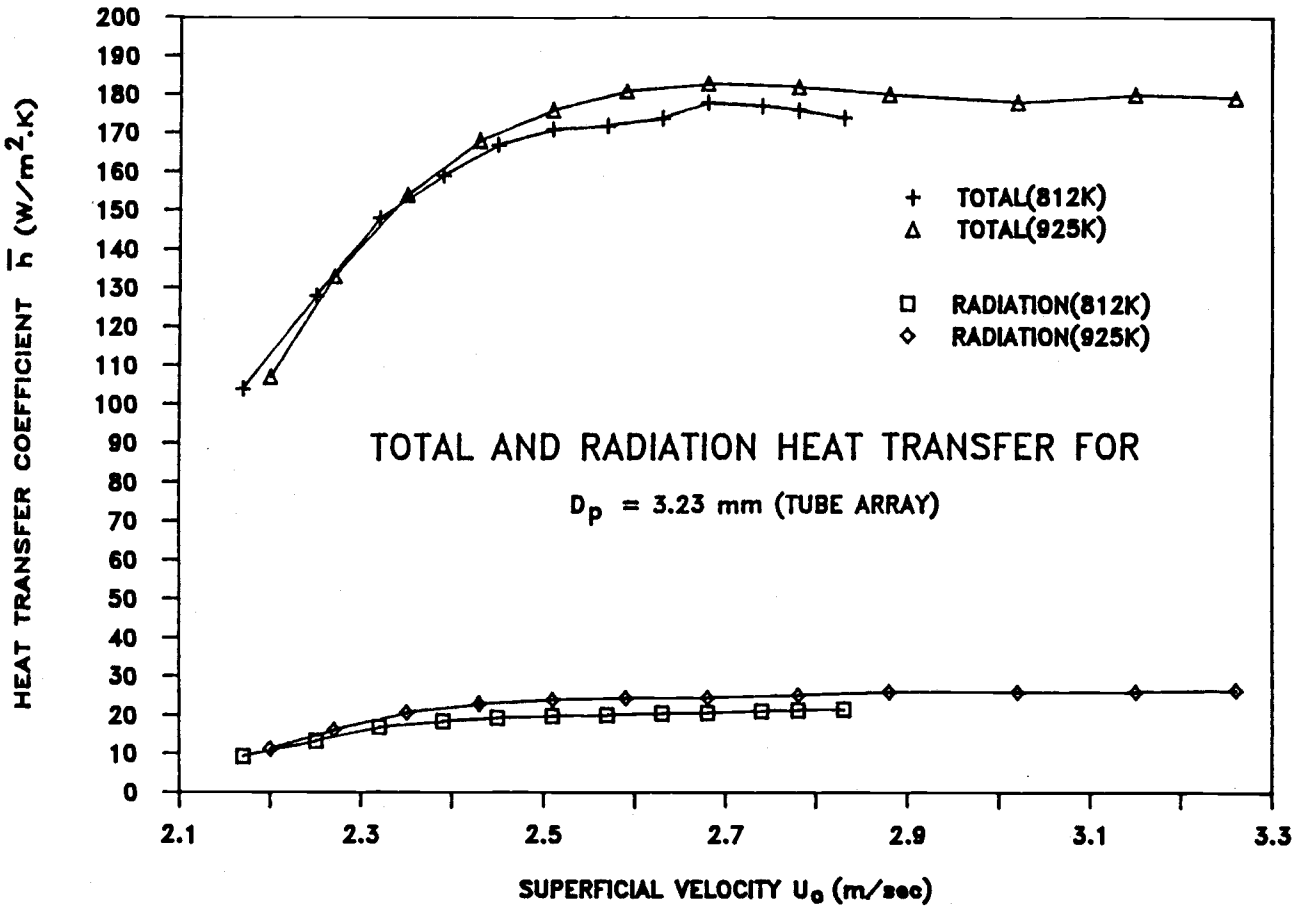

Figure 4.3 $\bar{h}_{rb}$ and $\bar{h}_t$ vs. U_o for D_p = 3.23 mm (Tube Array).

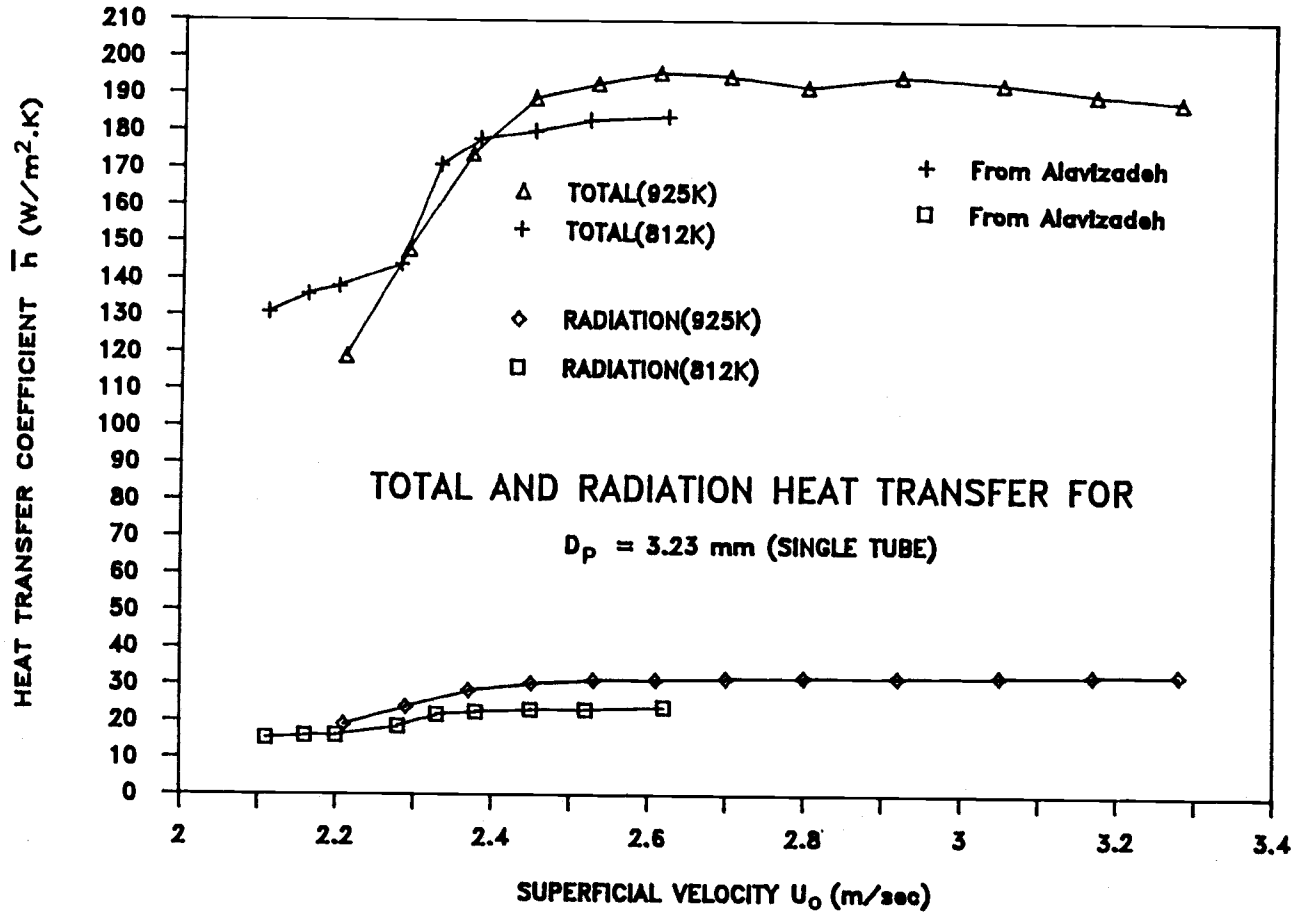

Figure 4.4 $\bar{h}_{rb}$ and $\bar{h}_t$ vs. U_o for D_p = 3.23 mm (Single Tube).

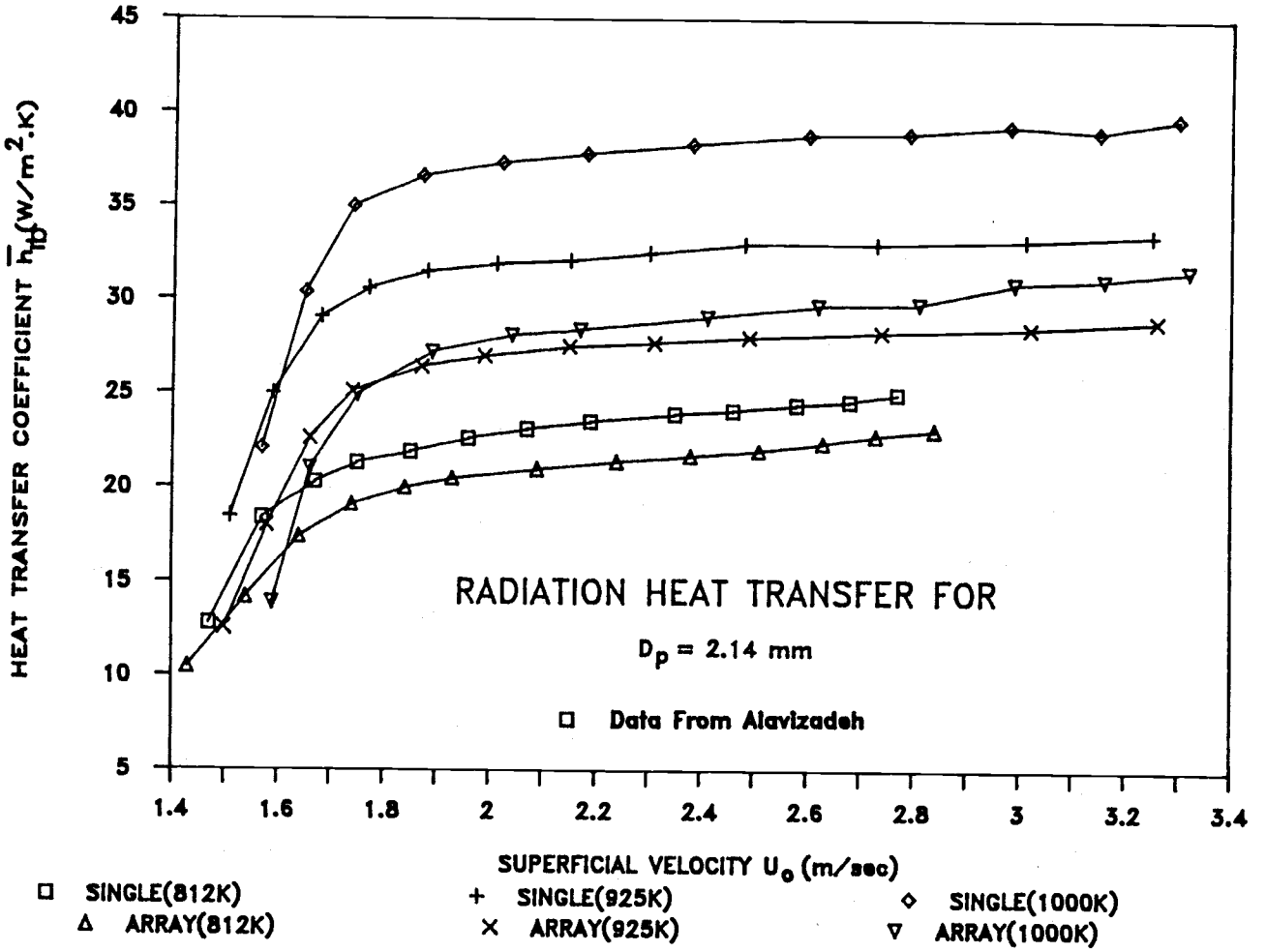

Figure 4.5 $\bar{h}_{rb}$ vs. U_o for D_p = 2.14 mm.

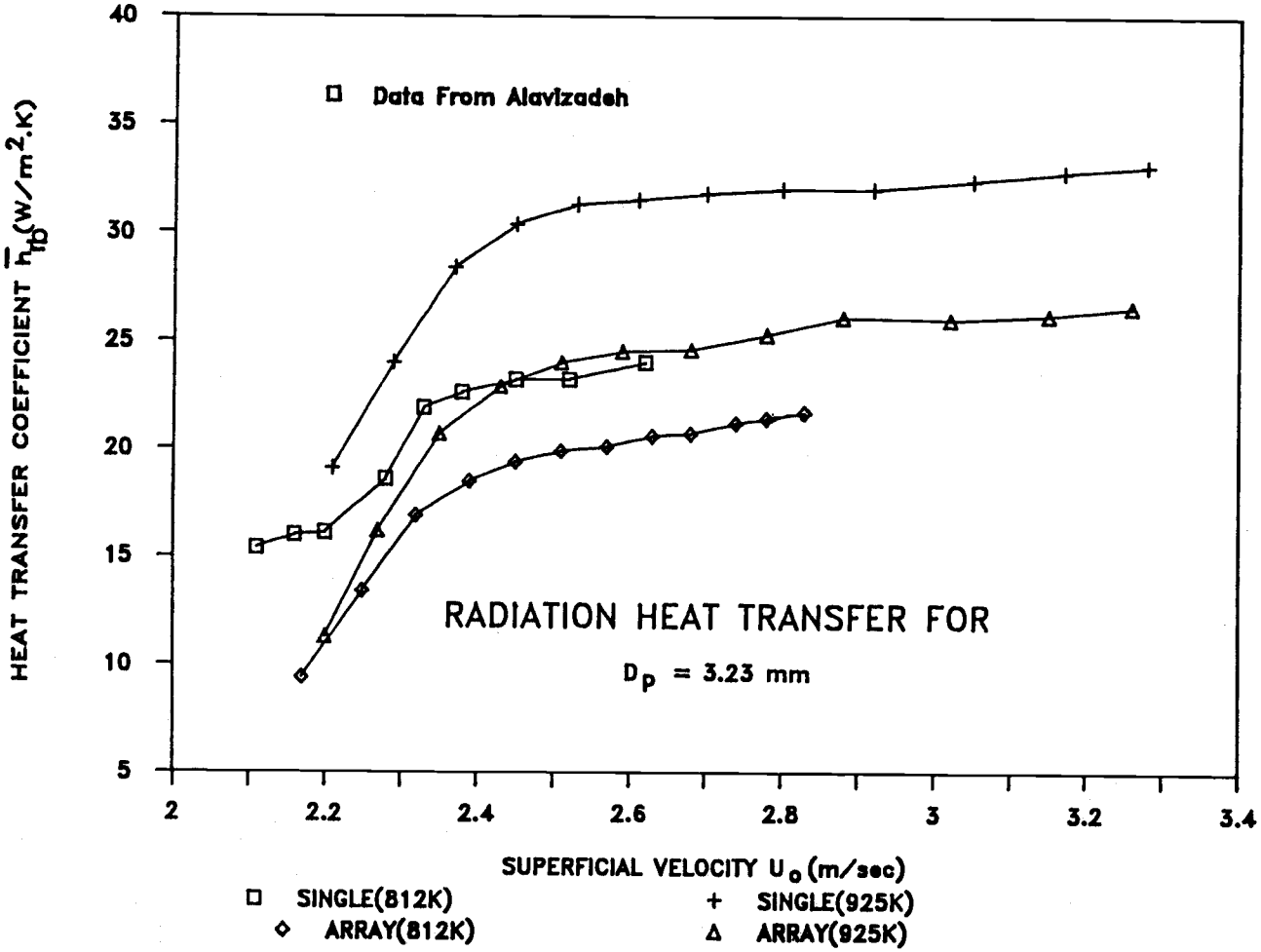

Figure 4.6 $\bar{h}_{rb}$ vs. U_o for D_p = 3.23 mm.

Effect of Superficial Velocity

A sharp increase in $\bar{h}_{rb}$ under all test conditions is noted as U_o reaches U_{mf}. The same behavior was observed by Alavizadeh (9) and Alavizadeh, et al. (12) for a single tube. This behavior is primary due to the bubble-induced particle motion which replaces the cold particles near the tube wall, particularly in the "lee stack" region on the upper half of the tube, as shown in Figure 1.3. A detailed discussion of this influence is presented in section 4.2.1. As U_o is increased well beyond U_{mf}, $\bar{h}_{rb}$ increases very slowly eventually approaching an asymptotic value, which implies that radiation transfer is relatively insensitive to the changes of bed density. The higher bubble contact fraction, f_o, at higher U_o results in larger radiation contributions in the bubble phase, which also compensates for the loss of radiation in the emulsion phase. Data of Alavizadeh (9), Alavizadeh, et al. (12), and Vadivel and Vedamurthy (131) shows similar trends except that Vadivel and Vedamurthy observed a slight decrease in $\bar{h}_{rb}$ past a maximum in their experiments for D_p = 0-6 mm, T_f = 1023 K.

Effect of Bed Temperature

Bed temperature has a pronounced effect on $\bar{h}_{rb}$ for all test conditions as shown in Figures 4.5 and 4.6. Specifically $\bar{h}_{rb}$ increased approximately 70% for the single tube case with D_p = 2.14 mm when the bed temperature was increased from 812 K to 1000 K, and it is approximately 55%

for the tube array case with D_p = 2.14 mm. It was found that $\bar{h}_{rb}$ increased more sharply at higher T_f as U_o approached U_{mf}. This behavior is directly attributable to the fourth-power temperature dependence in the Stefan-Boltzmann law of thermal radiation.

Effect of Particle Size

The effect of particle size was not found to be significant for the two particle sizes chosen (2.14 mm and 3.23 mm) in this study, except that the radiative heat transfer rate for the smaller particles was more sensitive to a change in U_o as U_o approached U_{mf}. It was noted, however, that large particles in a bubbly bed experienced a smaller temperature drop, and thus, had a higher average temperature as they came into contact with immersed surfaces. Accordingly, there is a higher radiation contribution than with small particles at the same bed temperature. Investigations of Alavizadeh, et al. (12) for D_p = 0.5 mm - 3.23 mm, Vedamurthy and Sastri (135) for D_p = 3.15 mm and 6.3 mm, and Vadivel and Vedamurthy (131) for D_p = 0-6 mm clearly demonstrated these effects. Results of Alavizadeh, et al. suggested that, from the standpoint of radiation contribution, particles with a mean diameter in the range of 1 mm to 2 mm could be classified as "intermediate" rather than "large" in high temperature fluidized bed applications.

Effect of Adjacent Cool Tubes

The data obtained with a single tube provide a basis for studying the effects of neighboring "cool" tubes on radiative heat transfer performance. Values for the radiative heat transfer coefficients as a function of superficial velocity for both tube arrays and a single tube are shown in Figures 4.7 through 4.11.

Radiative heat transfer coefficients for tube arrays are lower than for a single tube under all test conditions, as indicated in Figures 4.7 and 4.11, as well as in Figures 4.5 and 4.6. The average reductions in $\bar{h}_{rb}$ under bubbly bed conditions were calculated by comparing these two cases. Values for the percent decrease under different test conditions are tabulated in Table 4.2. It was found that the decrease in $\bar{h}_{rb}$ is greater for larger particles and at higher temperatures. This is due to the effect of the presence of neighboring "cool" tubes in the hot bed which absorb heat from the particles and reduce the effective bulk bed temperature.

A calculation, using an effective bed emissivity, $\epsilon_{ef} = Q_{rb}/\sigma T_f^4$, indicates the effective bed temperatures for tube arrays to be 804 K, 890 K, and 934 K for 2.14 mm particles at bed temperatures of 812 K, 925 K, and 1000 K, respectively. The corresponding effective temperatures are 783 K and 870 K for 3.23 mm particles at bed temperatures of 812 K and 925 K.

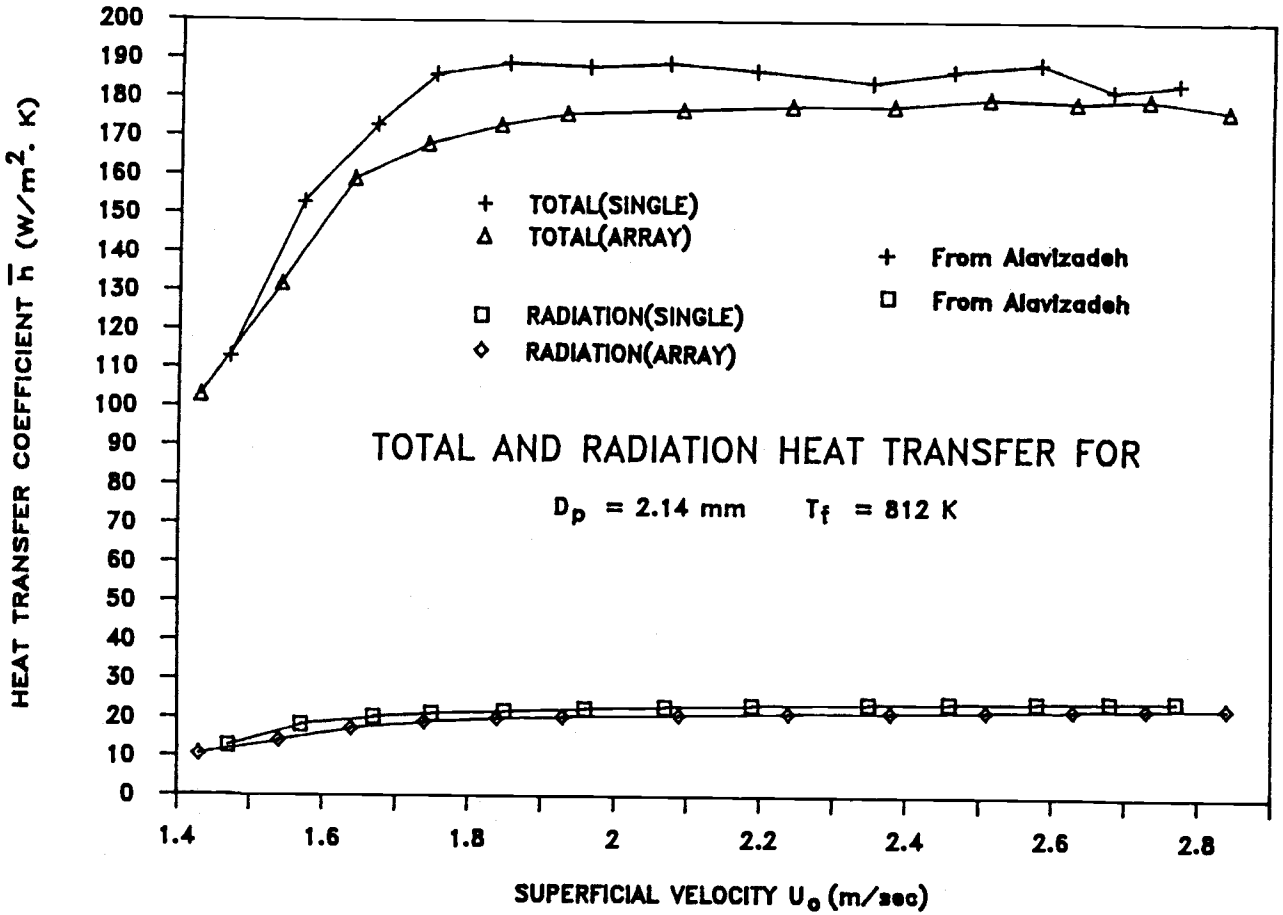

Figure 4.7 $\bar{h}_{rb}$ and $\bar{h}_t$ vs. U_o for D_p = 2.14 mm, T_f = 812 K.

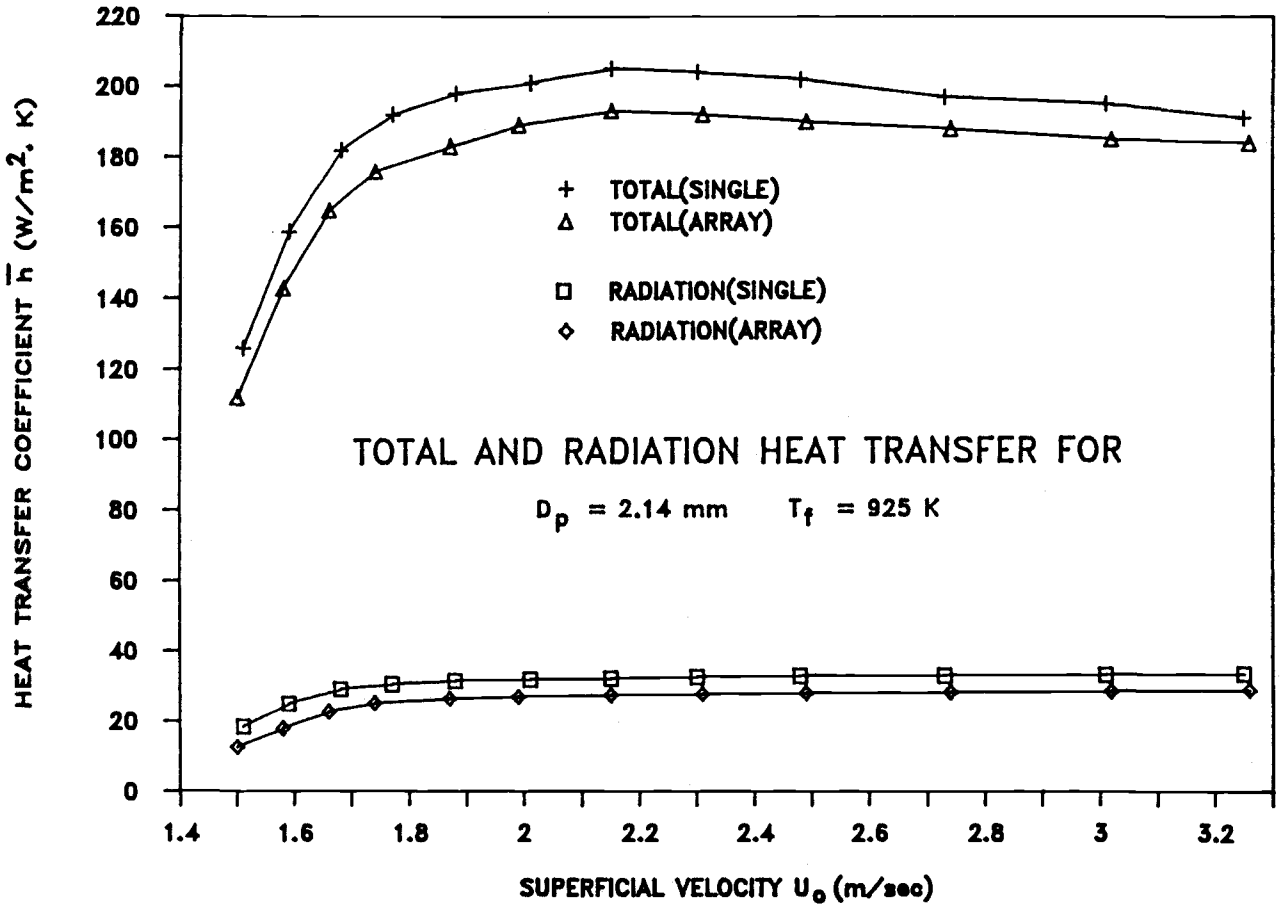

Figure 4.8 $\bar{h}_{rb}$ and $\bar{h}_t$ vs. U_o for D_p = 2.14 mm, T_f = 925 K.

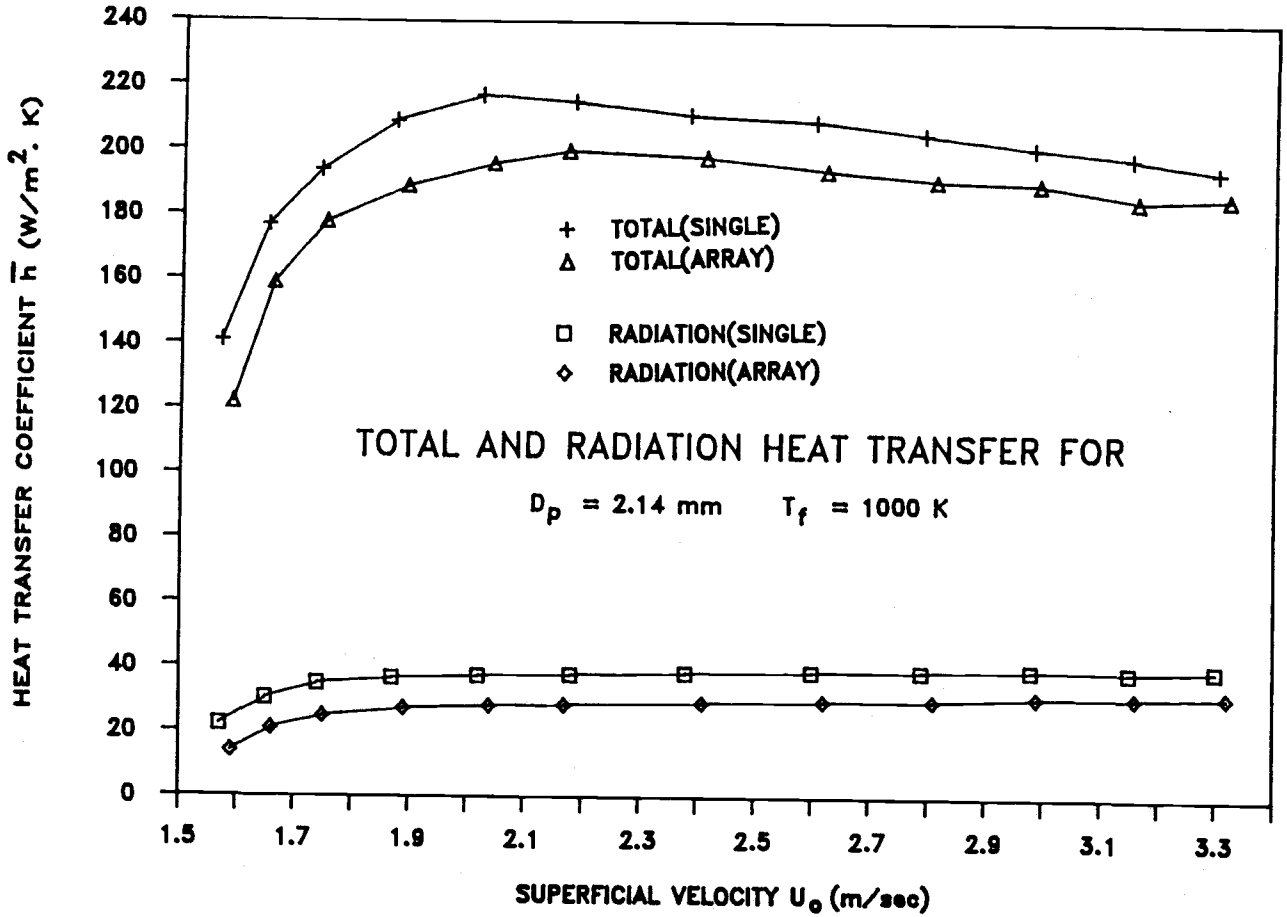

Figure 4.9 $\bar{h}_{rb}$ and $\bar{h}_t$ vs. U_o for D_p = 2.14 mm, T_f = 1000 K.

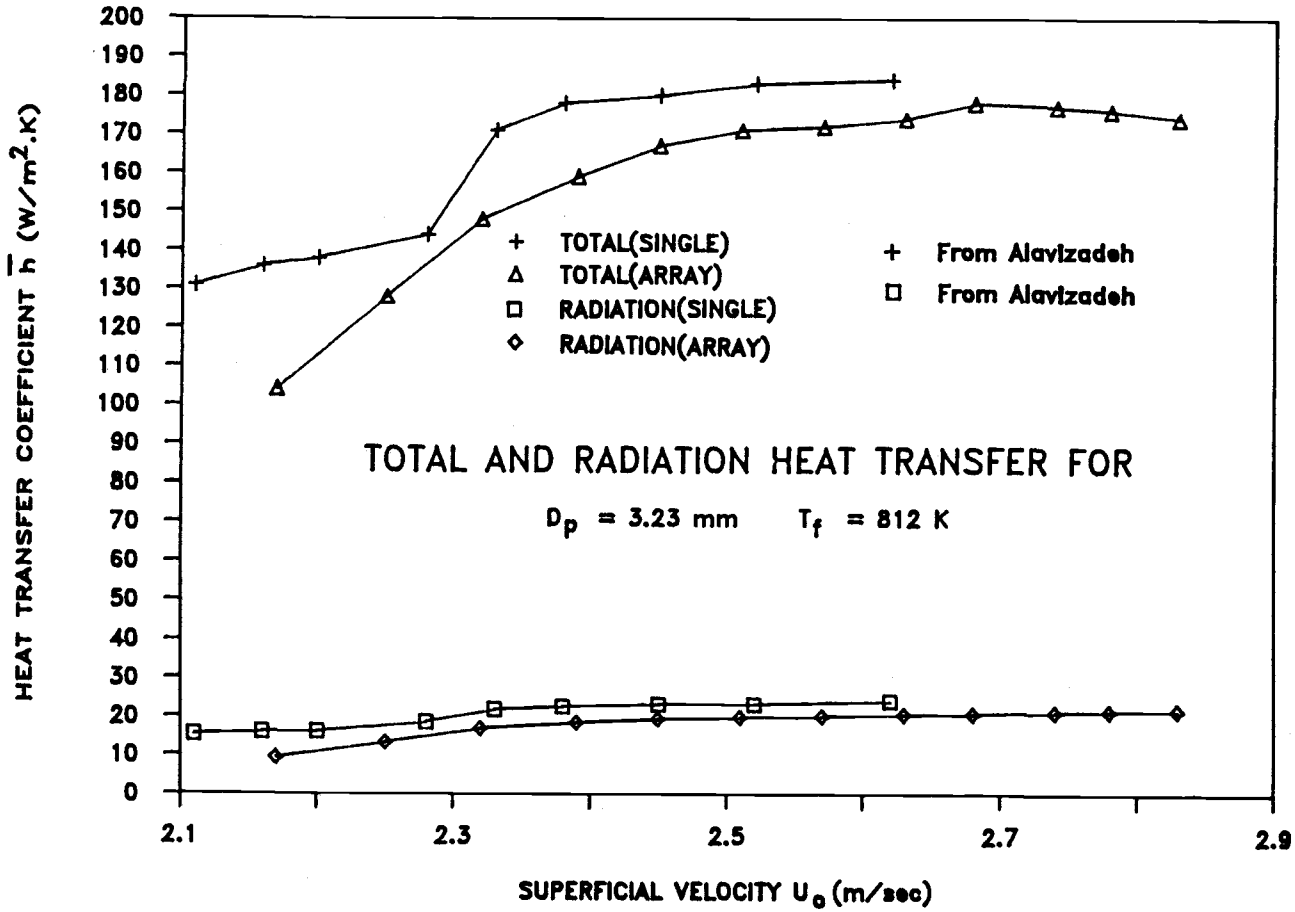

Figure 4.10 $\bar{h}_{rb}$ and $\bar{h}_t$ vs. U_o for D_p = 3.23 mm, T_f = 812 K.

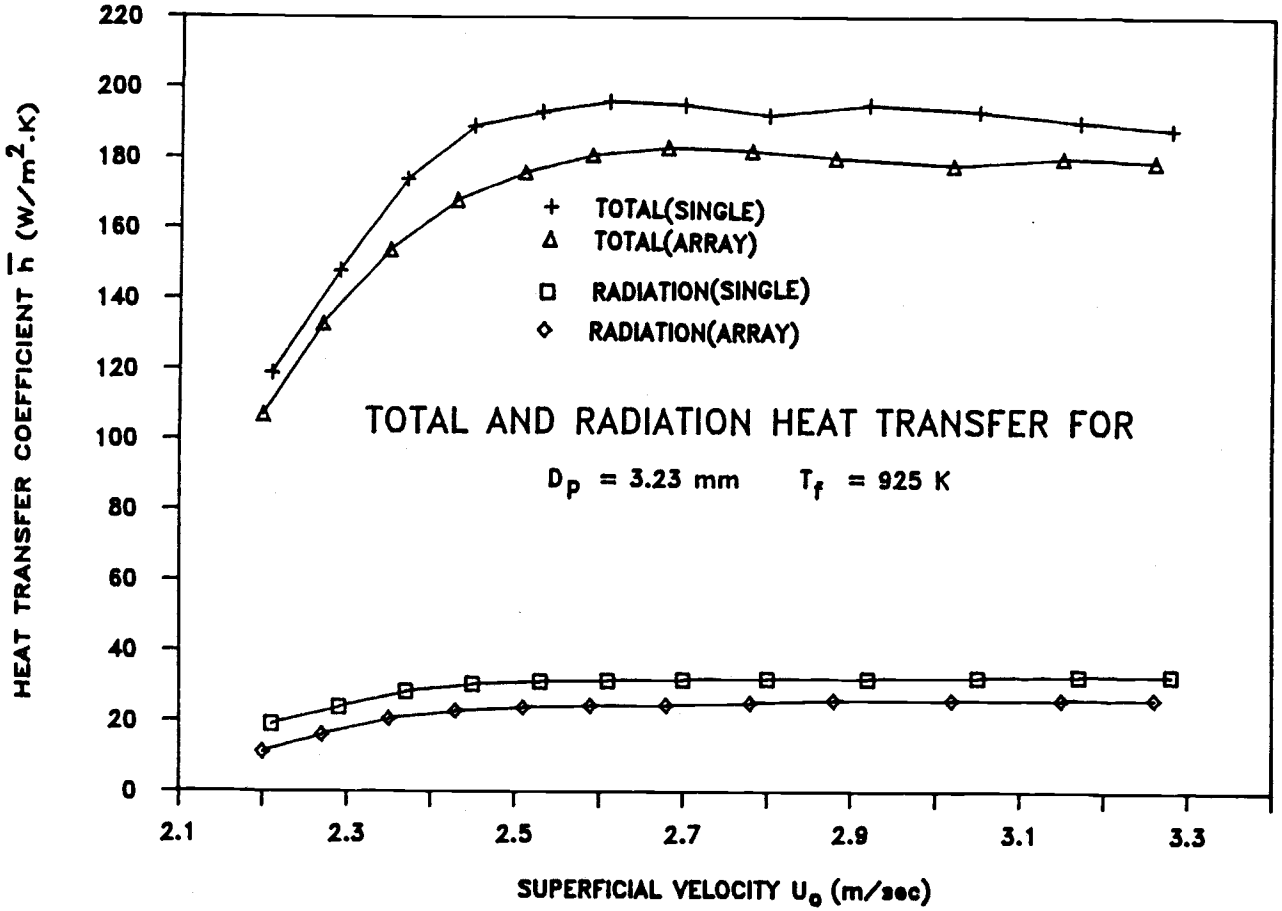

Figure 4.11 $\bar{h}_{rb}$ and $\bar{h}_t$ vs. U_o for D_p = 3.23 mm, T_f = 925 K.

The number of particles between adjacent tubes is about 30 for 3.23 mm particles and about 45 for 2.14 mm particles. At the same bed temperatures, values listed in Table 4.2 for an array, show the decrease in radiative heat transfer coefficient to be higher for larger particles than for small particles, when compared with a single tube. It is clear that the effective bed temperature is lower for the case of larger particles. Two effects contribute to this situation. On the one hand, bubbles sweep the cooler particles from the bottom row of the array upward. This bubble-induced particle motion decreases the surrounding temperature at upper levels in the tube arrays, and thus, will decrease the thermal radiation exchange. Also, larger particles offer greater "see through" effects from the neighboring "cool" tubes in a bubbly bed which further results in a lower surrounding temperature. The reduction will be even higher if bed operation is in the slugging or turbulent regimes.

Radiation Contribution

The radiation contributions (f) to total heat transfer rate, under different test conditions, are listed in Tables C.1 through C.10. The overall radiation contributions (f_{ave}) were computed as the average of f in the bubbly-bed state ($U_o > U_{mf}$). Values of f_{ave} for each test condition are listed in the last two rows of Table 4.2, also in Table C.1 through C.10.

Comparisons

The correlation proposed by Glicksman (70), equation (1.9), provides an upper limit for the radiation contribution in the emulsion phase. It was found that all values of the radiative heat transfer coefficient obtained in this work are within the limits predicted by equation (1.9).

No experimental data are available in the literature comparing radiation results for tube arrays. Results of the single tube case are in excellent agreement with those obtained by Alavizadeh (9). In light of the dependence of the radiation contribution on different test conditions, such as particle size, bed temperature, and particle and surface radiative properties, no further comparisons with other experimental investigations can be made for the single tube.

Alavizadeh (9) assumed the radiation in fluidized beds to be proportional to the fourth power of the bed temperature and compared his results with some other studies (16,22,37,89,112,114) by plotting $\bar{h}_{rb}$ vs. T_f^3, as shown in Figure 4.12. This might be useful since the single tube results of the present study are in good agreement with his.

A number of analytical models have been developed for radiation heat transfer in a fluidized bed, as described in section 1.3.1. No comparisons of the present study results can be made with existing models since they require special input parameters such as bubble contact fraction, bubble

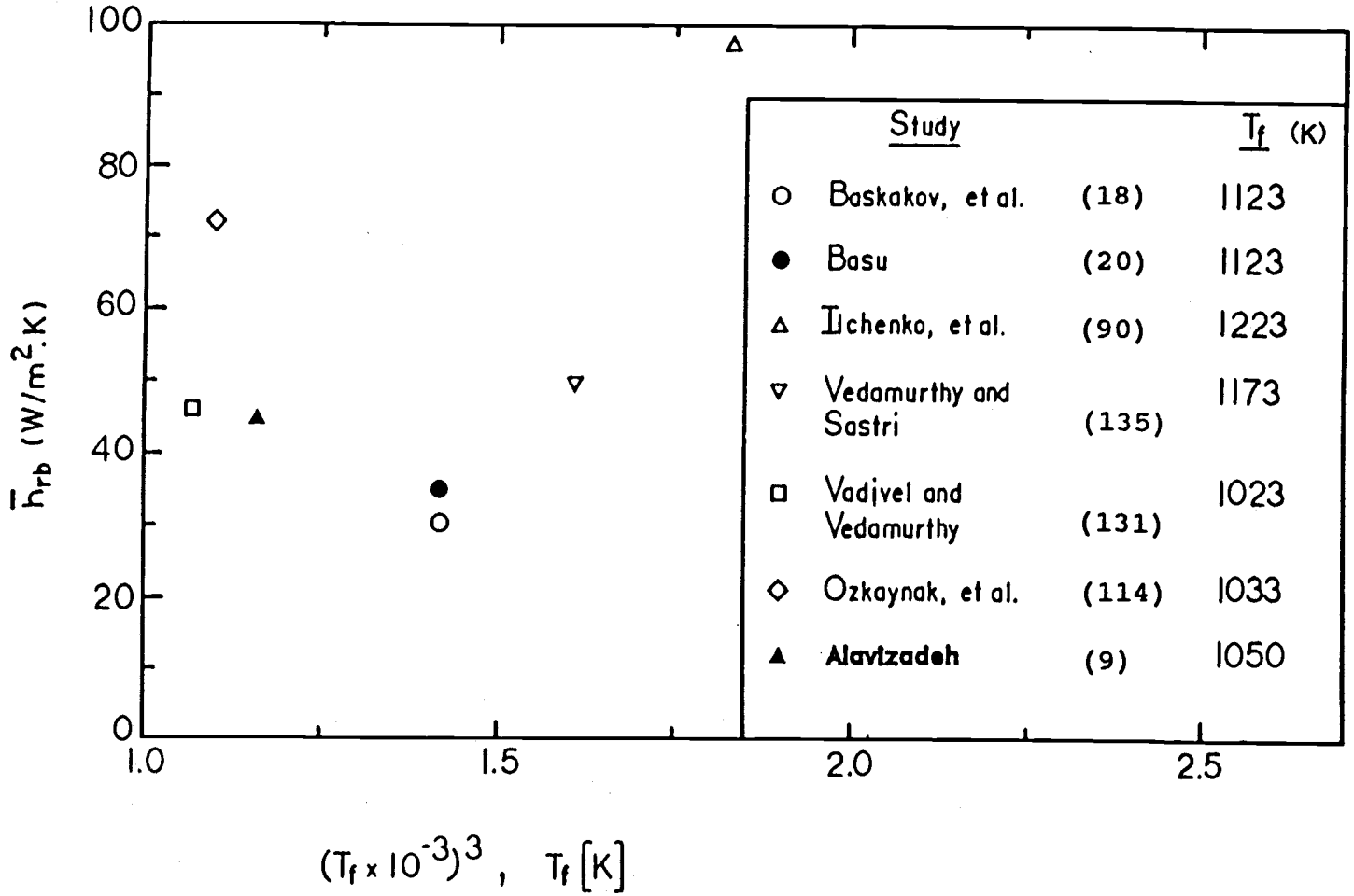

Figure 4.12 Radiative heat transfer coefficients obtained in different studies.

frequency, emulsion residence time, particle spacing, and transmission characteristics, which were not measured in this study.

4.1.2 Total Heat Transfer

Figures 4.1 through 4.4 show the spatial-averaged total heat transfer coefficient ($\bar{h}_t$) as a function of superficial velocity (U_o) under different test conditions. A close look at the total data is provided in Figures 4.13 and 4.14.

Effect of Superficial Velocity

When U_o approaches the minimum fluidizing velocity (U_{mf}), $\bar{h}_t$ increases sharply due to the gas-particle agitation as was explained in section 4.1.1. This sharp increase is followed by a short period of a more gradual increase, $\bar{h}_t$ reaching a maximum value for U_o somewhat greater than U_{mf}, and then shows a slow decrease. This behavior was noted by many other investigators for a wide range in particle sizes and bed temperatures. The slow decrease can be attributed to the decrease in bed density and also greater bubble contact fraction (f_o) at higher values of U_o.

Effect of Bed Temperature

The effect of bed temperature was not evaluated in most of the total heat transfer studied since they were conducted at low or ambient temperatures. Increases in $\bar{h}_t$ (Figures

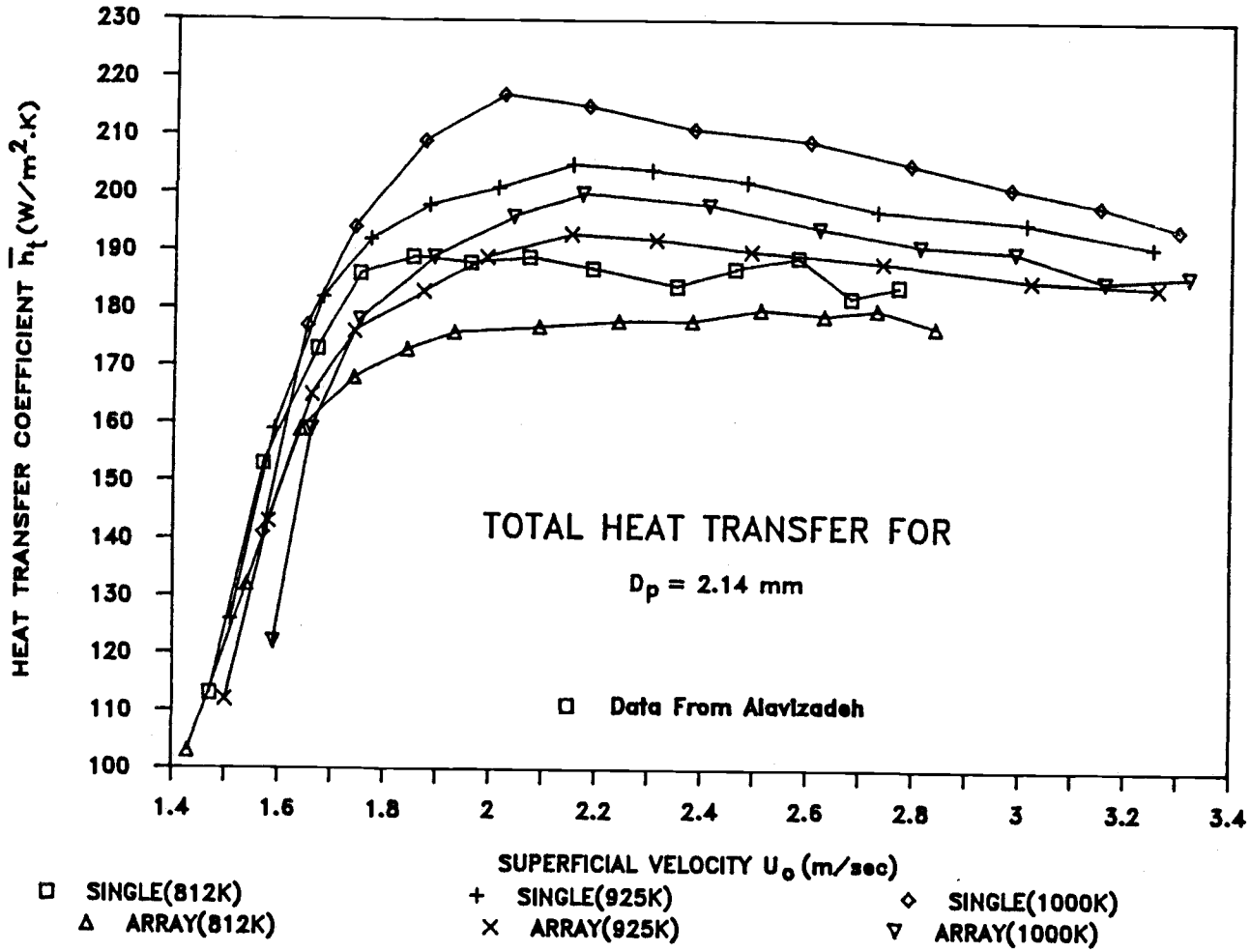

Figure 4.13 $\bar{h}_t$ vs. U_o for D_p = 2.14 mm.

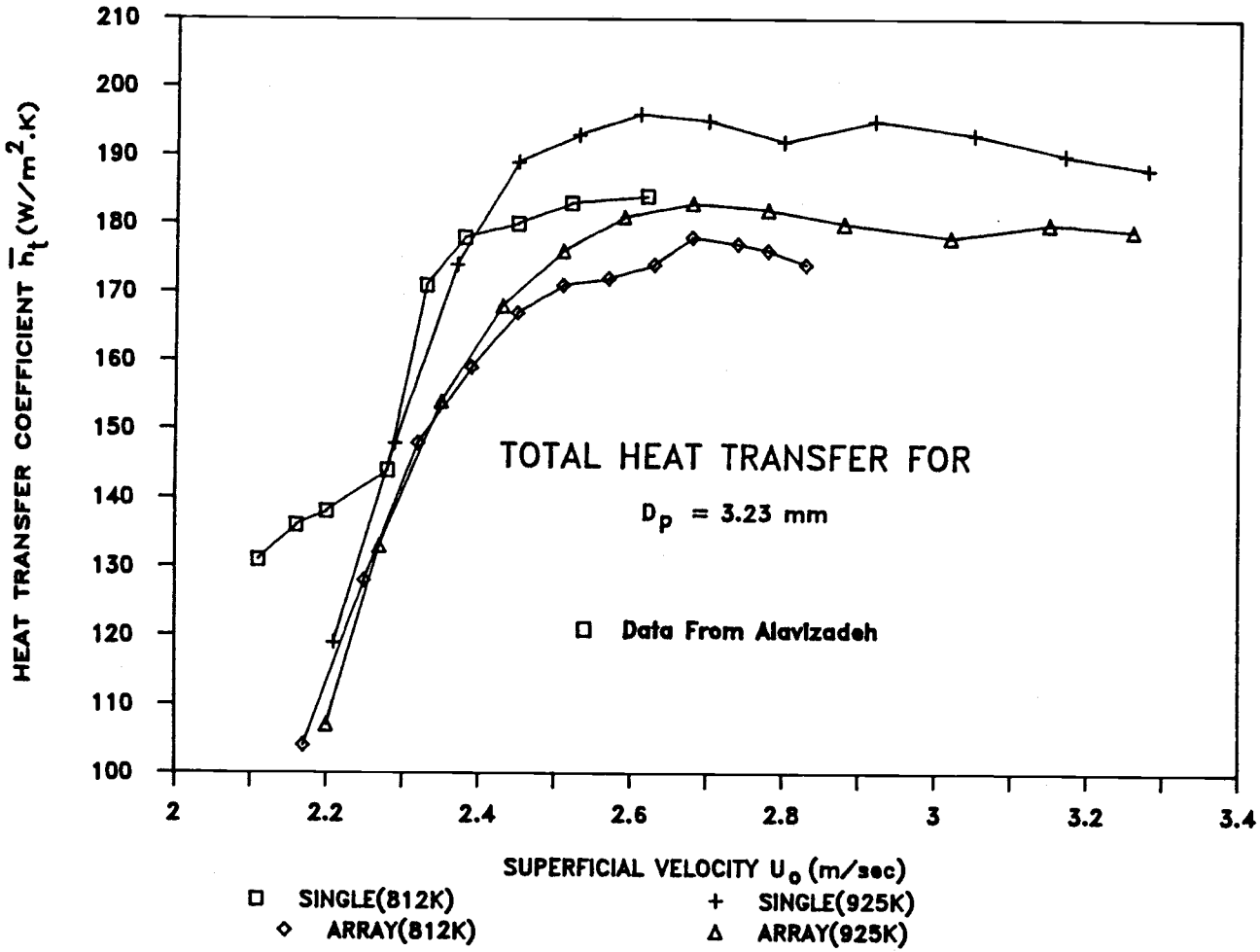

Figure 4.14 $\bar{h}_t$ vs. U_o for D_p = 3.23 mm.

4.13 and 4.14) and $\bar{h}_{max}$ (Table 4.1) for all test conditions were found as the bed temperature was increased, e.g. for the single tube case with 2.14 mm particles shown in Table 4.1, there was an increase, in $\bar{h}_{max}$, of 28 $W/m^2.K$ (15%) when the bed temperature was elevated from 812 K to 1000 K, and the increase was 19 $W/m^2.K$ (11%) for the tube arrays. Comparing the increase in $\bar{h}_{rb}$ under identical conditions (15 $W/m^2.K$ and 7 $W/m^2.K$), the change in $\bar{h}_{max}$ (or $\bar{h}_t$) cannot be explained solely by the additional radiative contribution, as suggested by some investigators (90,113,128).

Observed variations of $\bar{h}_{max}$ and $\bar{h}_t$ with T_f should not be quantitatively generalized here due to scattering in the radiation data. Reasons for the higher total heat transfer at elevated temperatures can be physically explained by both the greater radiation contribution and larger gas-solid convection, resulting from the increased gas thermal conductivity. Similar conclusions have been reached by other researchers (9,75,144). Alavizadeh (9) suggested this behavior to be due to the variation in thermophysical properties of the gas with bed temperature, i.e. a greater thermal conductivity at higher bed temperatures results in increased particle convection. Golan, et al. (75) concluded that gas and solid thermal properties play a role in the variation of total heat transfer with bed temperature. Yoshida, et al. (144) suggested that it is affected by the increase in both the thermal conductivity in the emulsion phase and the bubble frequency, rather than radiation.

Effect of Particle Size

Total heat transfer in beds over a wide range in particle sizes has been reported (18,95,109,113,133) and discussed (30,79,102,145) by various investigators. Results of such findings are illustrated in Figure 4.15, in which the maximum heat transfer coefficient is plotted against particle diameter. The decrease of $\bar{h}_{max}$ with D_p in the fine particle range (D_p < 0.02 mm) is due to poor fluidization characteristics (agglomeration and channeling) of such fine powder. In the small particle range (0.02 mm < D_p < 1 mm) where the particle convective component (h_{pc}) dominates, $\bar{h}_{max}$ decreases with increase in D_p caused by a greater thermal resistance between particles and heat transfer surfaces, a smaller particle surface area per unit volume of the bed, and a higher bubble contact fraction for larger particles. Further increases in D_p eventually result in a transition (1 mm < D_p < 2 mm) from small-particle to large-particle effects (D_p > 2 mm) in which the gas convective component (h_{gc}) becomes dominant. In this position of the size spectrum, $\bar{h}_{max}$ increases with D_p due to higher fluidization velocities and a corresponding increase in particle Reynolds number (Re_p).

In the present study small decreases (1% - 5%), in $\bar{h}_{max}$ with an increase in particle size from 2.14 mm to 3.23 mm, were noted for both tube arrays and a single tube at the same bed temperature, as shown in Table 4.1 and Tables C.1 through C.10. Decreases for tube arrays are relatively less

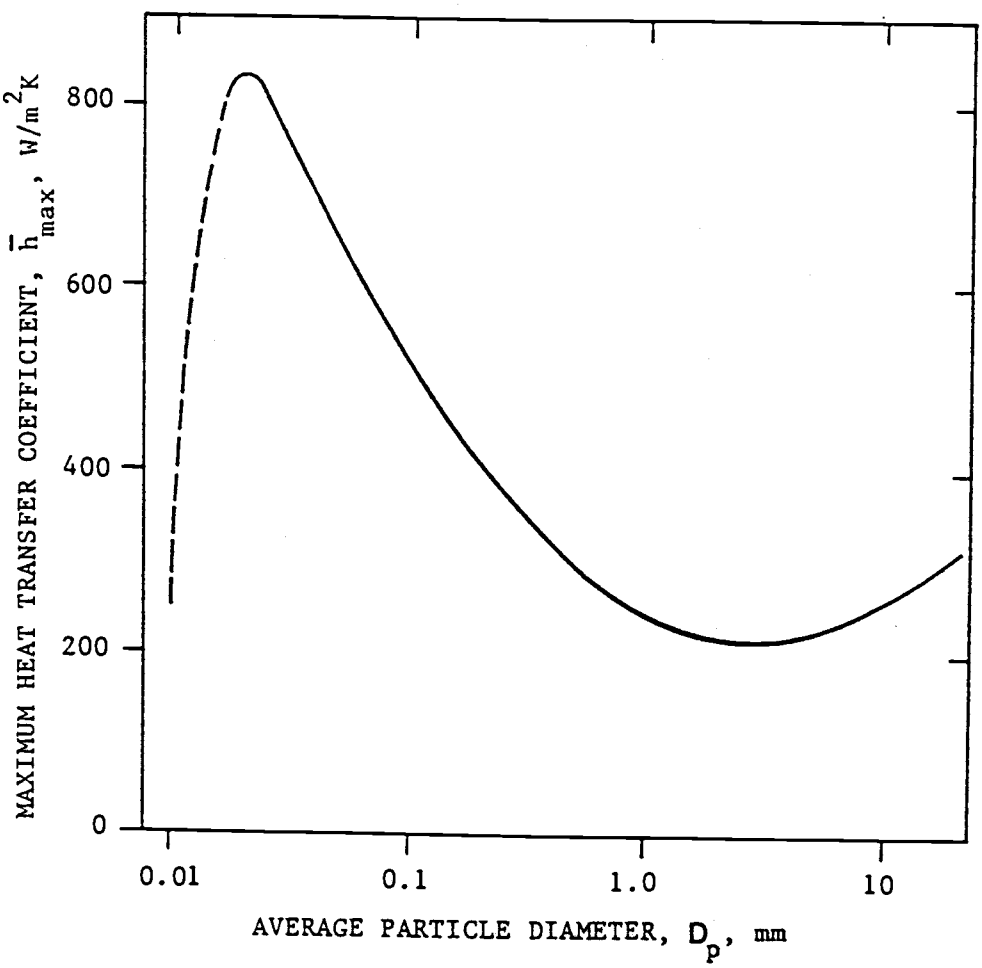

Figure 4.15 Dependence of the maximum heat transfer coefficient on mean particle diameter. [Adapted from Zabrodsky, S. S. (145)]

than for a single tube. Similar trends were found by Alavizadeh (9) and Goshayeshi (77) while the results of George (66) showed no significant difference for these two particle sizes. This is because the particle sizes employed fall into the transition region, as shown in Figure 4.15, with a corresponding small difference in magnitude for $\bar{h}_{max}$.

Effect of Adjacent Cool Tubes

The effect of adjacent-tube-spacing on total heat transfer was studied extensively for small particle beds at low temperatures, as summarized by Botterill (30), Grewal (79), and Saxena, et al. (122). The tube array arrangement was designed according to the studies by Welty (138), Catipovic (40), and others (25,64,127), as already discussed in section 3.2.

The relative decrease in $\bar{h}_t$ for the tube array relative to a single tube remained almost unchanged (6% - 8%) as the bed temperature was increased for both particle sizes, as shown in the third column of Table 4.2. The data obtained by Goshayeshi (77) under almost identical test condition showed about the same magnitude for the decrease in $\bar{h}_t$. Similar trends were also found in the experiments conducted by Catipovic (40) for a wide range of particle sizes (0.37 mm $\leq D_p \leq$ 6.6 mm) at ambient temperature. His suggested correlations, equations (1.2) through (1.6), also suggest such an invariance for low-temperature beds. When comparing the decrease in $\bar{h}_{rb}$, the indication is that the relative

decrease in $\bar{h}_t$ is less sensitive to the change in bed temperature than is $\bar{h}_{rb}$.

Comparison

Figure 4.16 shows the maximum Nusselt number ($\overline{Nu}_{max}$) as a function of Archimedes number (Ar) for the present tube-array case and for some other studies conducted by Alavizadeh, et al. (12), Goshayeshi (77), and Catipovic (40). The properties of air, evaluated at the bed temperature, were used in the calculations of $\overline{Nu}_{max}$ and Ar. Also shown are the correlations proposed by Maskaev and Baskakov (109) and Zabrodsky, et al. (147). For larger particles, Maskaev and Baskakov suggested the formula

$$\overline{Nu}_{max} = 0.21\ Ar^{0.32} \qquad 1.4 \times 10^5 < Ar < 3 \times 10^8 \qquad (4.1)$$

Zabrodsky, et al. (100) expressed their correlation as

$$\overline{Nu}_{max} = 0.88\ Ar^{0.213} \qquad 80 < Ar < 10^6 \qquad (4.2)$$

It is observed that equation (4.1) fits the tube array data of the present study at higher temperatures (925 K and 1000 K) quite well; it fits single tube data even better.

As described in section 1.3.2, different correlations have been proposed recently to estimate the total heat transfer for horizontal tubes immersed in large particle beds and their predictions agree reasonably well with most

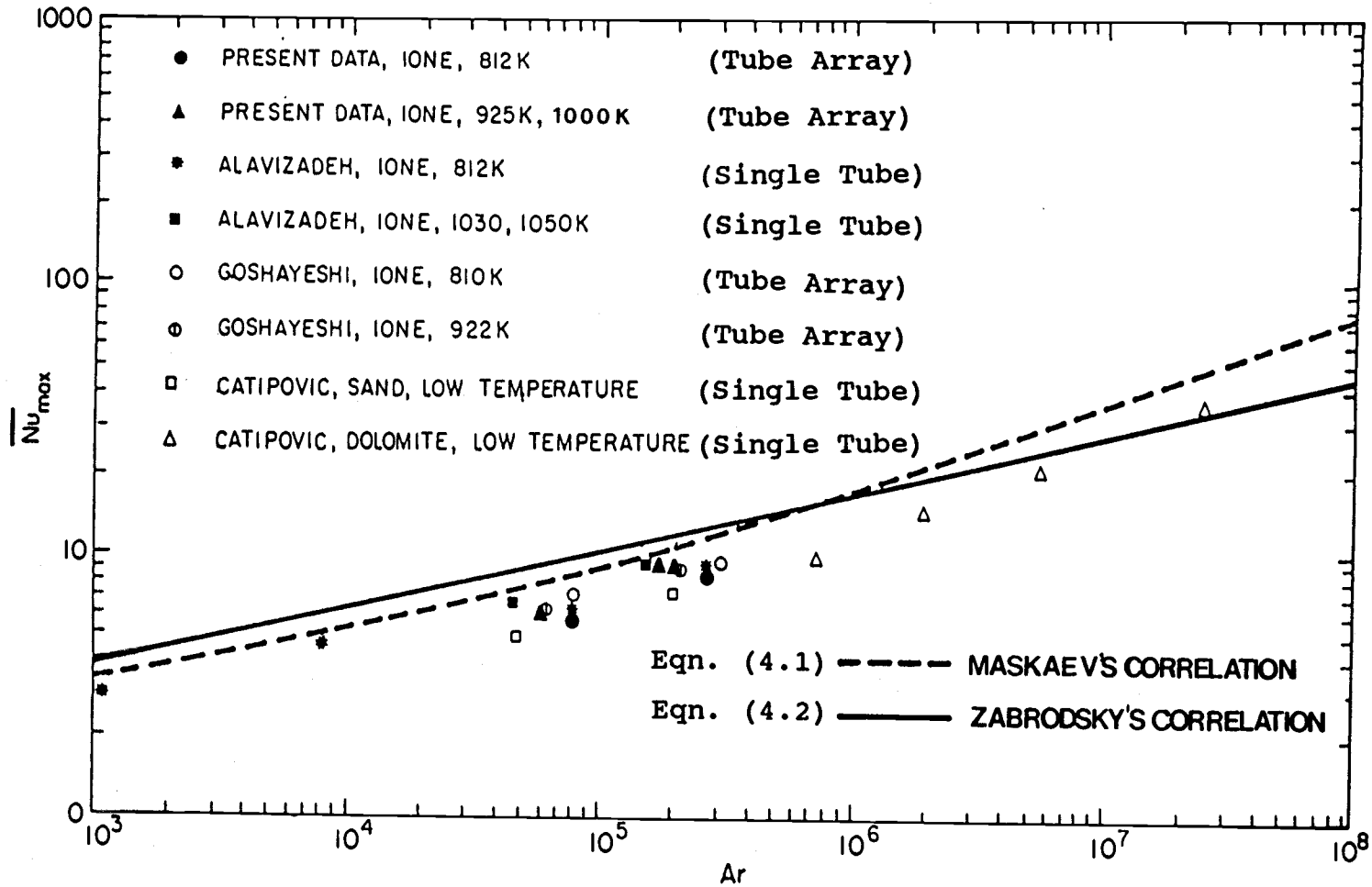

Figure 4.16 Maximum Nusselt number vs. Archimedes number in different studies. [Adapted from Alavizadeh, N. (9)]

of the existing data for low temperature beds. If the radiation contribution is neglected, however, these correlations tend to underestimate the convective heat transfer coefficients obtained in this work as well as those of Alavizadeh (9) obtained in a high-temperature bed. Specifically, the correlations suggested by Catipovic (40), equations (1.2) through (1.6), underestimate our results by approximately 15% at T_f = 812 K and 20% at T_f = 1000 K. This difference indicates that equation (1.3) underestimates the gas convective component at high temperature bubbly-bed conditions since it was obtained based on the minimum fluidization condition in a cold bed (19).

4.2 Local Heat Transfer

Tables C.1 through C.10, in Appendix C, list the complete results of the time-averaged local heat transfer measurements for both tube arrays and a single tube. Graphical results showing local heat transfer coefficients (h_{rb} and h_t) for the tube arrays are presented for a range of superficial velocities under each test condition. The effect of superficial velocity on local heat transfer performance will now be considered. Also to be considered is the effect of adjacent "cool" tubes by comparing the results of these two cases.

The distribution of local heat transfer coefficients (h_{rb} and h_t) for both cases was found to be invariant with a change in bed temperature for the particle sizes employed in

this study, although they do affect the magnitude of these local values, and thus special-averaged heat transfer performance, as discussed in section 4.1. Similar trends were shown in the experimental studies of Alavizadeh (9), Goshayeshi, et al. (78), and George (66). No further attempts will be made to discuss these effects.

4.2.1 Local Radiative Heat Transfer

Values for the local radiative heat transfer coefficient (h_{rb}) around the instrumented tube for tubes arrays are displayed in Figures 4.17 through 4.21. Each figure shows the results with a given particle size and bed temperature for six superficial velocities (U_o). Two values of velocity are below U_{mf}; the others are greater.

Effect of Superficial Velocity

Values of h_{rb} are relatively low at packed bed conditions ($U_o < U_{mf}$), particularly on the down stream side of the tube ($\alpha > 90^o$). As U_o reaches a value slightly higher than U_{mf}, a large increase in h_{rb} with U_o was observed over the upper half of the tube ($\alpha = 135^o$ and 180^o). A more uniform distribution of h_{rb} was established as higher values of U_o were reached. Values of h_{rb} on the lower half of the tube, however, were always higher for all tests conducted. Results of Alavizadeh (9) and Alavizadeh, et al. (12) displayed the same behavior for D_p = 0.5-3.23 mm.

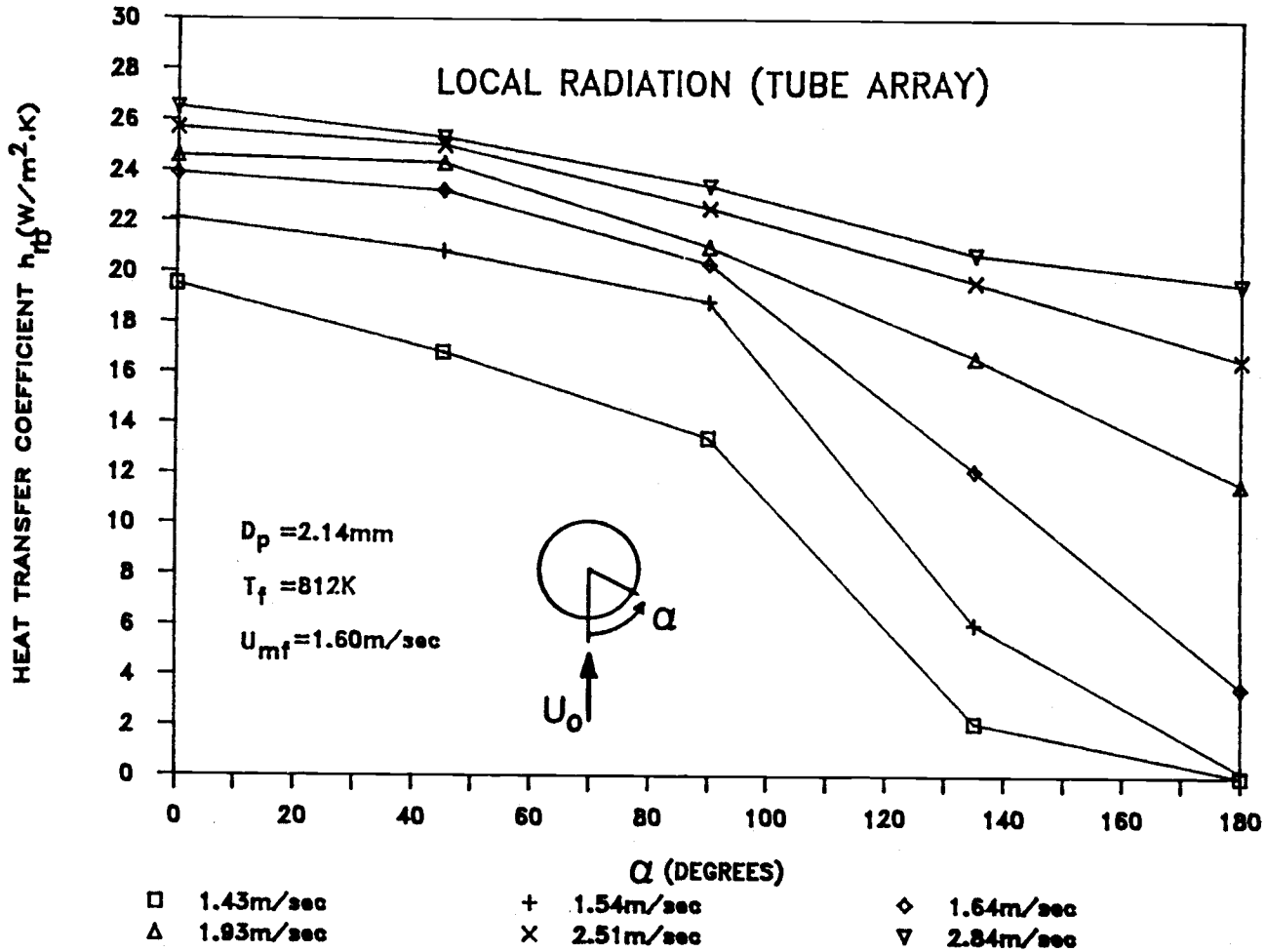

Figure 4.17 Local radiative heat transfer coefficient distribution for D_p = 2.14 mm, T_f = 812 K (Tube Array).

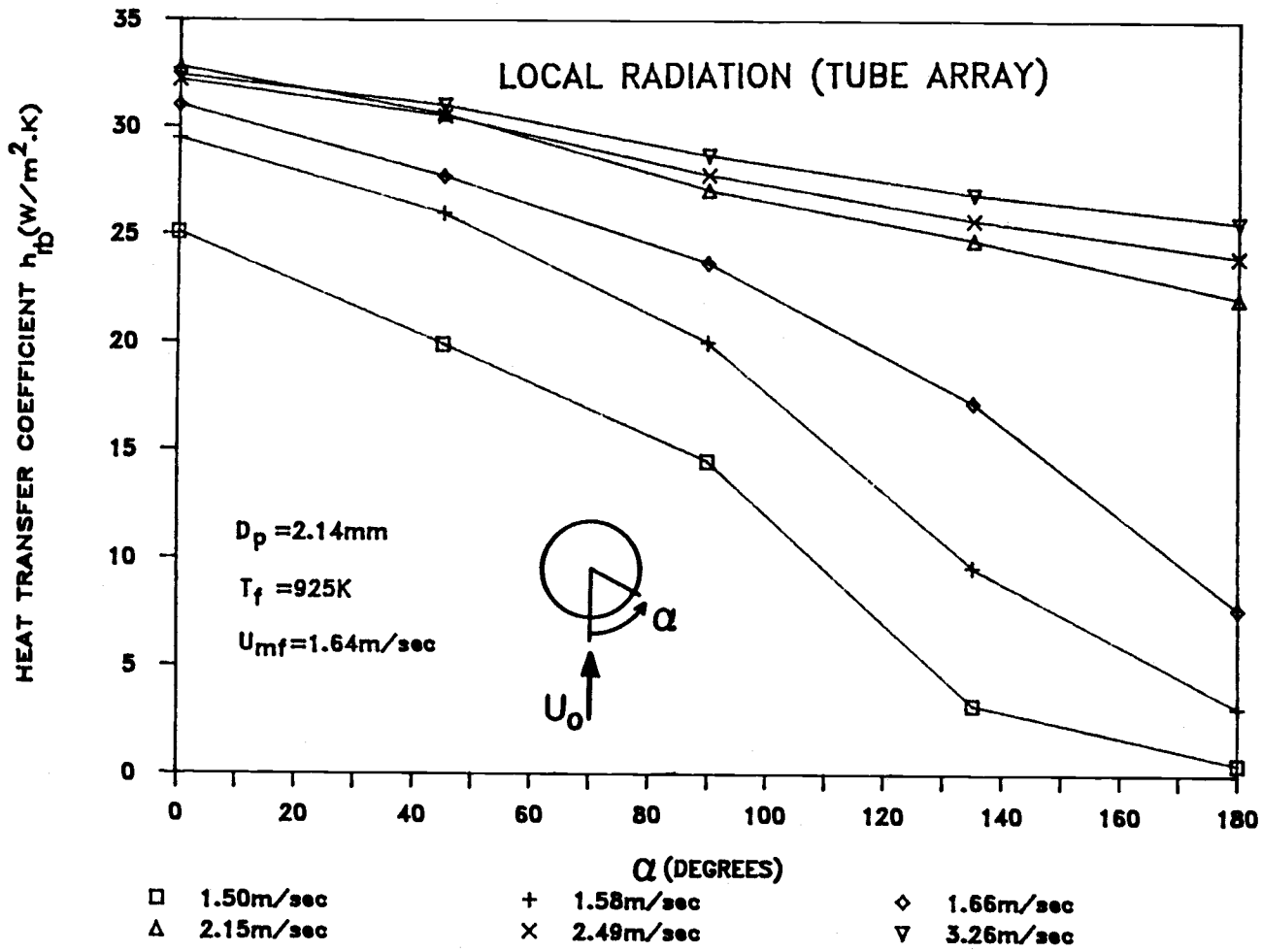

Figure 4.18 Local radiative heat transfer coefficient distribution for D_p = 2.14 mm, T_f = 925 K (Tube Array).

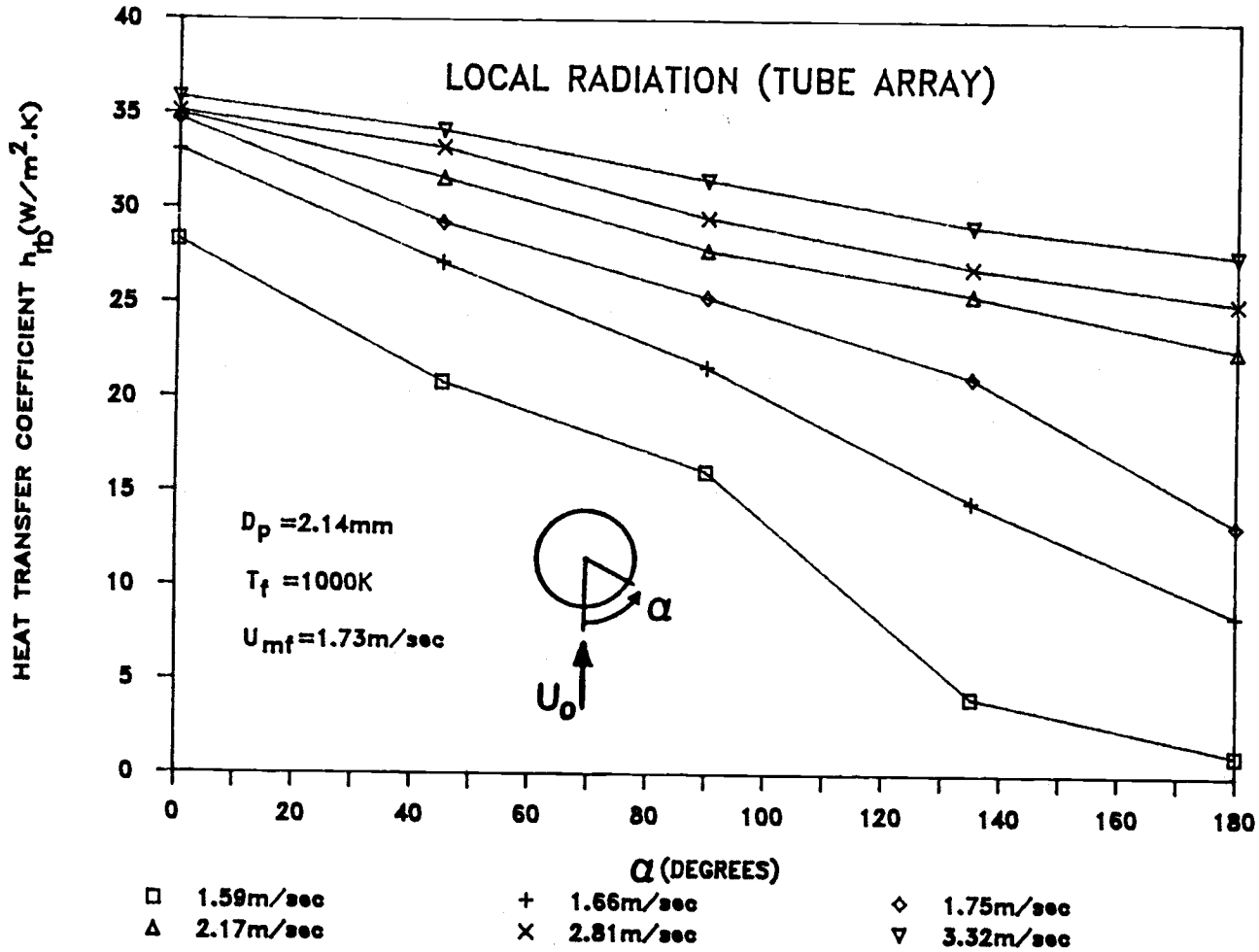

Figure 4.19 Local radiative heat transfer coefficient distribution for D_p = 2.14 mm, T_f = 1000 K (Tube Array).

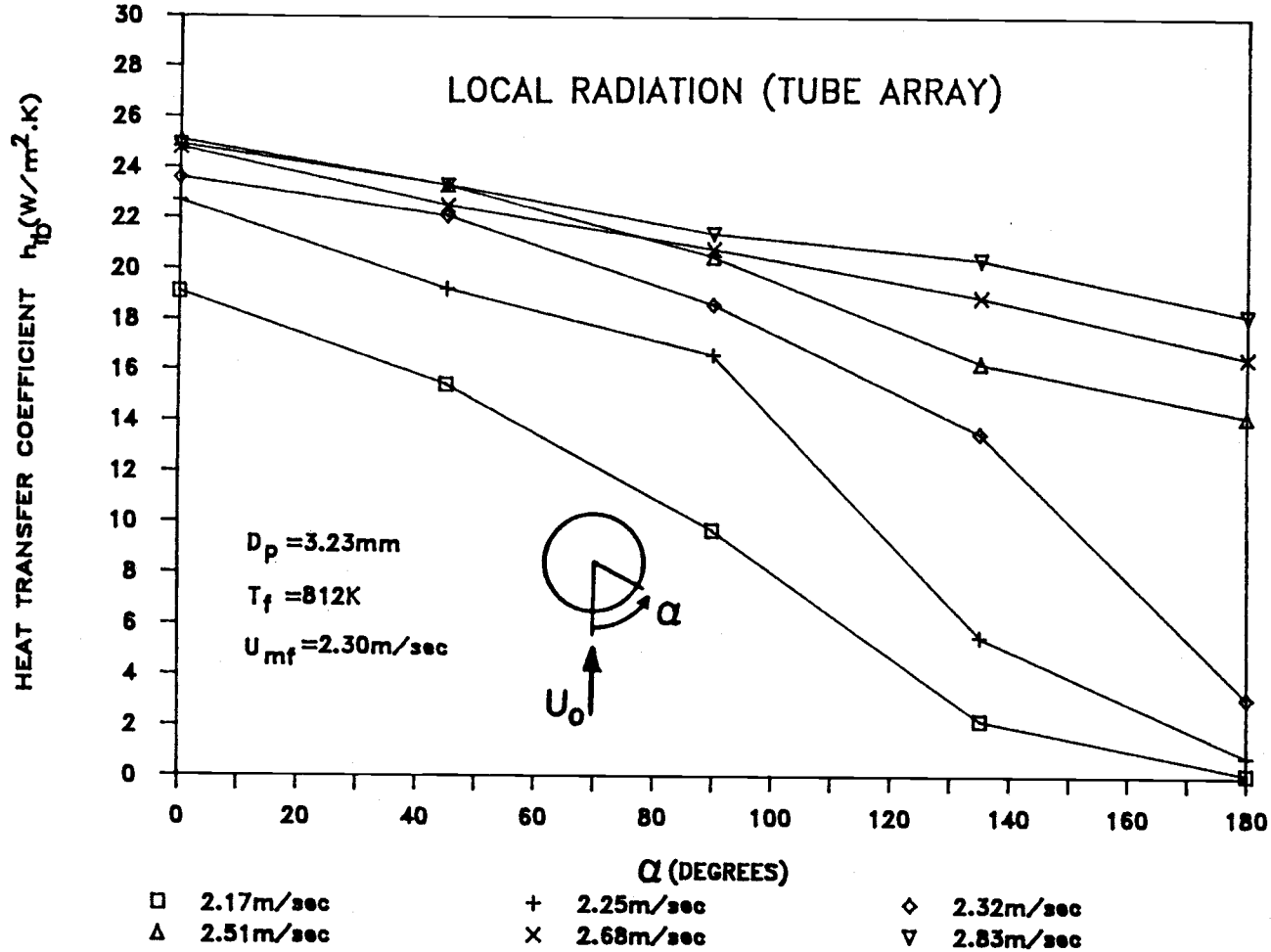

Figure 4.20 Local radiative heat transfer coefficient distribution for D_p = 3.23 mm, T_f = 812 K (Tube Array).

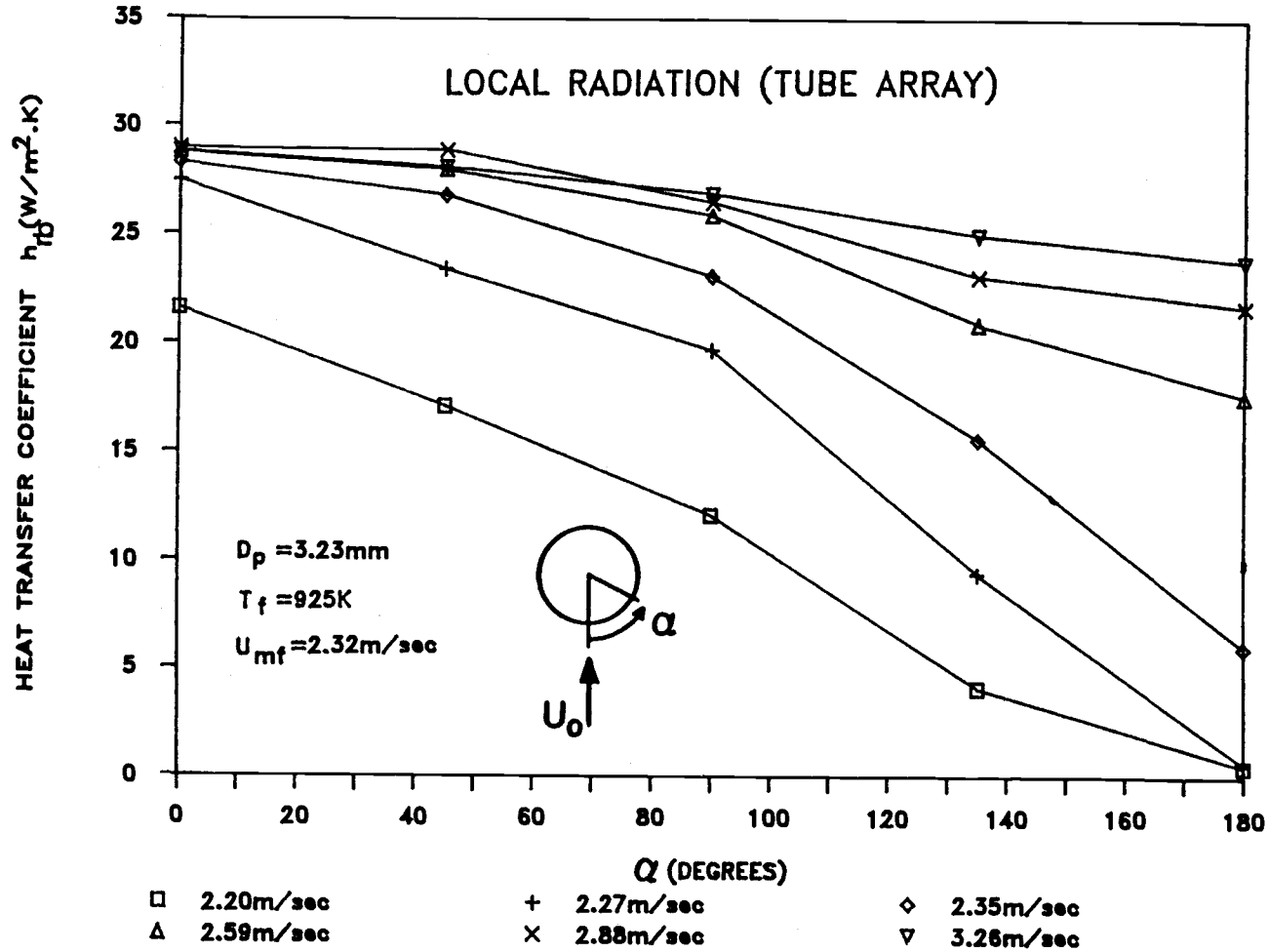

Figure 4.21 Local radiative heat transfer coefficient distribution for D_p = 3.23 mm, T_f = 925 K (Tube Array).

The relatively low radiation heat transfer values on the upper half of the tube at low U_o are caused by the "cool" stagnant defluidized particle "cap" formed on the top of the tube. The hydrodynamics of the so called "lee stack" region have been studied by various investigators (65,84,85), as described in section 2.1. As U_o is increased significantly above U_{mf}, the "cap" collapses due to the influence of rising bubbles, and the "long-staying and cooled" particles are replaced by fresh hot ones. Thus, the local radiation heat transfer is significantly increased. An increased particle mobility also produces a more uniform distribution of h_{rb} around the tube.

As noted earlier, values of h_{rb} on the lower half of the tube are insensitive to changes in U_o and remain higher than those for the upper half even for the bubbly-bed regime in which the lower portions of the tubes are generally shrouded by gas bubbles (85,120). This implies that, for the entire range of U_o, the radiation contribution due to the bubble phase compensates for the reduction in the emulsion phase which is caused by the low particle density adjacent to the lower half of the tube. In contrast, data, obtained by Vadivel and Vedamurthy (131) for a single horizontal tube with D_p = 0-6 mm and T_f = 1023 K, displayed an increase in h_r with U_o followed by a decrease as U_o approached $2U_{mf}$. The maximum local radiative heat transfer coefficient was observed to shift to the lateral position ($\alpha = 90^o$). This behavior is likely due to the inability of the bubble-phase

radiation to match the losses in the emulsion phase at very high superficial velocities. No other experimental data are available for analysis.

Effect of Adjacent Cool Tubes

Data for tube arrays show lower values at lateral positions, i.e. $\alpha = 45^{o}$, 90^{o}, and 135^{o}, compared with a single tube, due to the effect of adjacent "cool" tubes in a hot bed. These decreases are more pronounced at higher bed temperatures and for larger particles due to the sensitivity of the radiation to the drop in average bed temperature and the larger "see through" effect with larger particles, respectively. Further comparisons of h_{rb} with those in h_t show greater relative decreases in the local radiative heat transfer coefficient. This implies that the radiation contribution is more sensitive to bed temperature than is the total heat transfer. It further explains why the reduction in spatial-averaged radiative heat transfer coefficient ($\bar{h}_{rb}$) is larger than that of total value ($\bar{h}_t$), as discussed in section 4.1.

The maximum local radiative heat transfer coefficient with tube arrays always occurred at the stagnation point ($\alpha = 0$) for all test conditions. This was caused by the effect of adjacent "cool" tubes. An additional effect is the constant interchange of bubbles and particles at the stagnation point, as discussed by Keairns (94). For a single

tube, however, the maximum value still remained at the lower position of the tube ($\alpha = 0^{o}$, 45^{o}, and 90^{o}). This is because the regular replacement of cold particles by bubble action induced fresh hot ones in this region. This is consistent with observations by Peeler and Whitehead (115), Loew, et al. (103), and other (9,15,40).

Comparison

To our knowledge, the only other local radiative heat transfer measurements reported are those of Alavizadeh (9), Alavizadeh, et al. (12), and Vadivel and Vedamurthy (131). Local radiation values and their behavior in the present study, for a single tube, show excellent agreement with the results of Alavizadeh and fair agreement with those obtained by Vadivel and Vedamurthy. Results with tube array cases are the first of their kind.

Mahbod (104) developed a theoretical model for the radiative heat transfer to an immersed horizontal tube. He found the local radiative data of Alavizadeh to agree reasonably well with his analytical predictions. The information regarding emulsion residence time and bubble contact fraction were interpolated from measurements of Catipovic (40) for 1.3 mm and 4.0 mm particles in a two-dimensional cold bed.

4.2.2 Local Total Heat Transfer

Graphical results are included in Figures 4.22 through 4.26. Tabulated data for the single-tube case are listed in Tables C.6 through C.10.

Effect of Superficial Velocity

The effect of superficial velocity has been discussed by Goshayeshi, et al. (78), Alavizadeh (9), and George (66). The most obvious trend is a sharp increase in h_t at the downstream side of the tube as U_o approaches U_{mf}. This is known to be caused by the removal of the defluidized "cap" of particles, as described in section 4.2.1. The same behavior has been observed in previous local heat transfer studies in both high-(9,66,74,78) and low-(22,40,49) temperature beds.

The distribution of h_t around the surface of the tube tends to be more uniform as U_o is further increased. This distribution has been found (40) to be more uniform for large particles than for small particles (D_p < 1 mm) with the same value of U_o/U_{mf}. Thus, if there is concern for thermal stress in the tubes, operation with large particles at higher superficial velocities will provide less stressful conditions. Values of h_t display a small variation with U_o in an irregular manner at the lower stagnation point, as shown in the figures. Similar trends were observed by Goshayeshi, et al. (12), Alavizadeh (9), and Chandran, et al. (46).

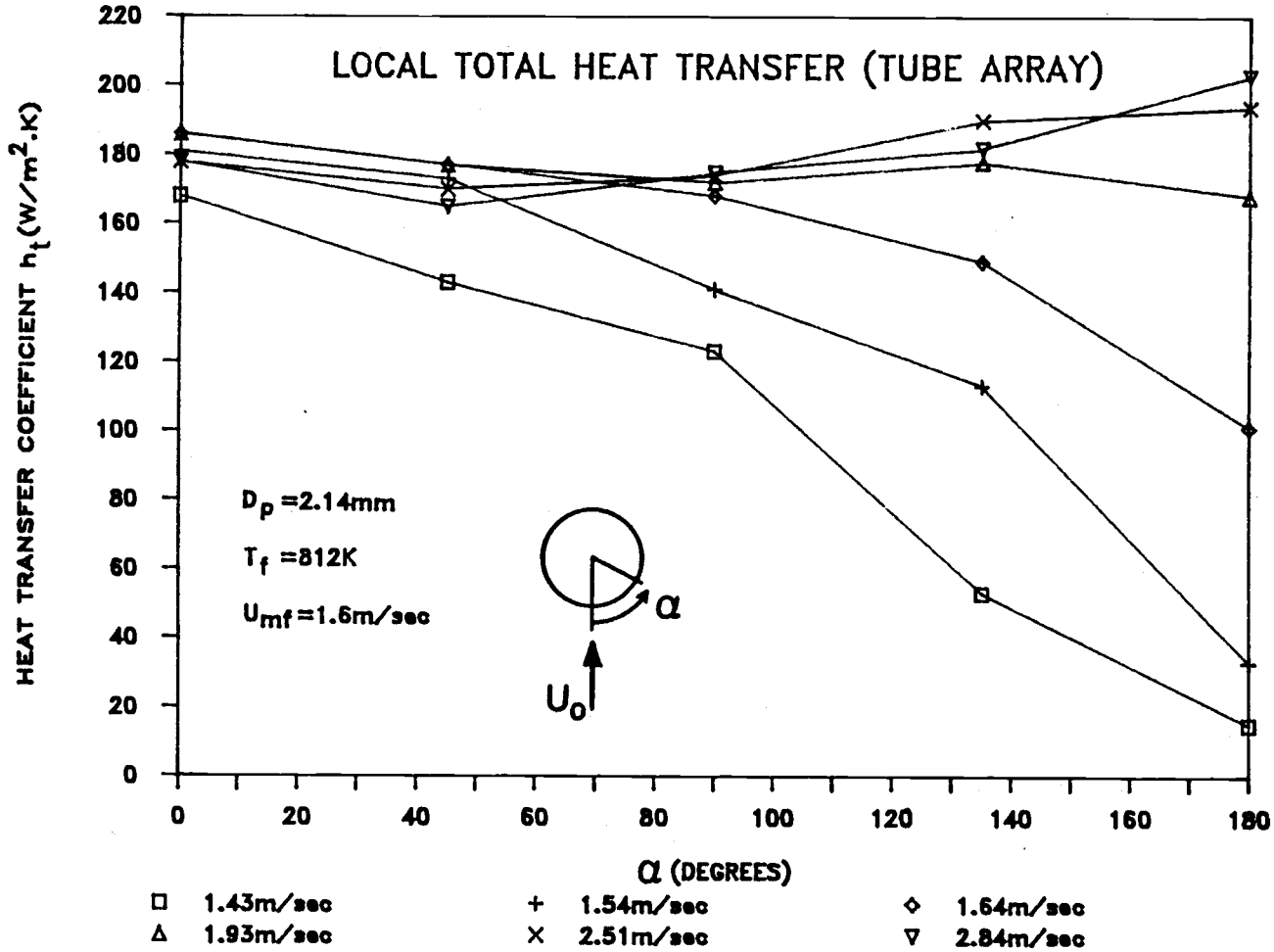

Figure 4.22 Local total heat transfer coefficient distribution for D_p = 2.14 mm, T_f = 812 K (Tube Array).

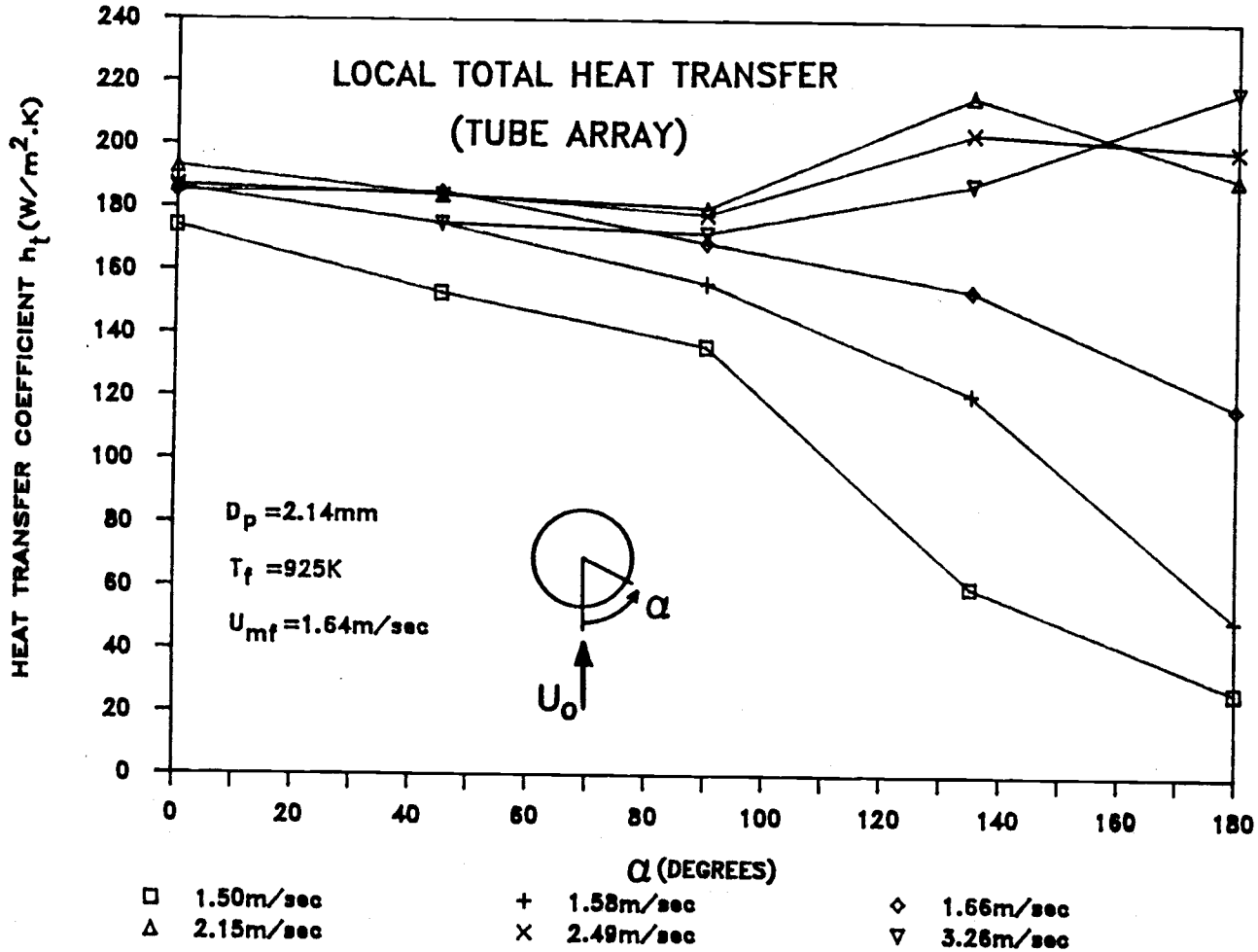

Figure 4.23 Local total heat transfer coefficient distribution for D_p = 2.14 mm, T_f = 925 K (Tube Array).

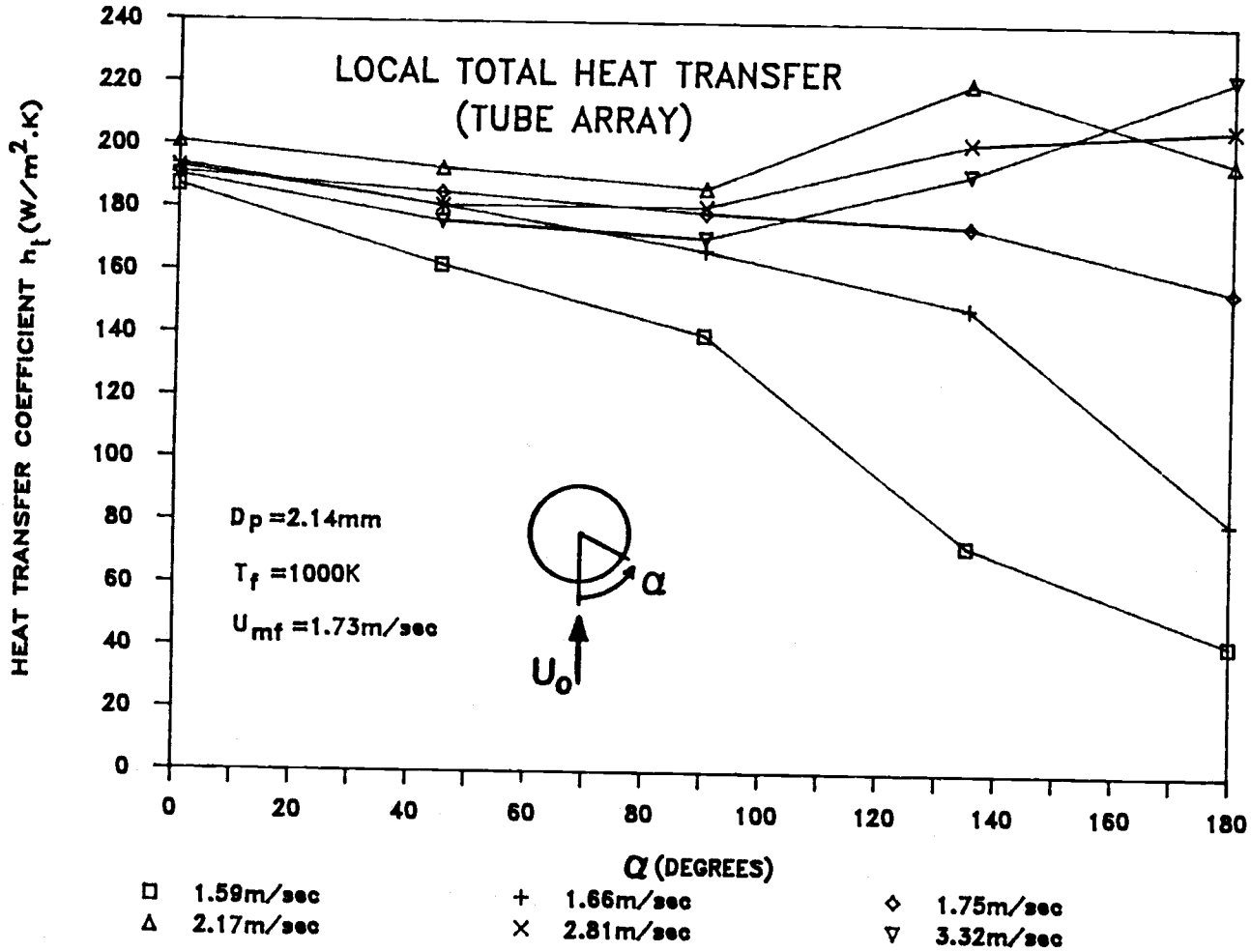

Figure 4.24 Local total heat transfer coefficient distribution for D_p = 2.14 mm, T_f = 1000 K (Tube Array).

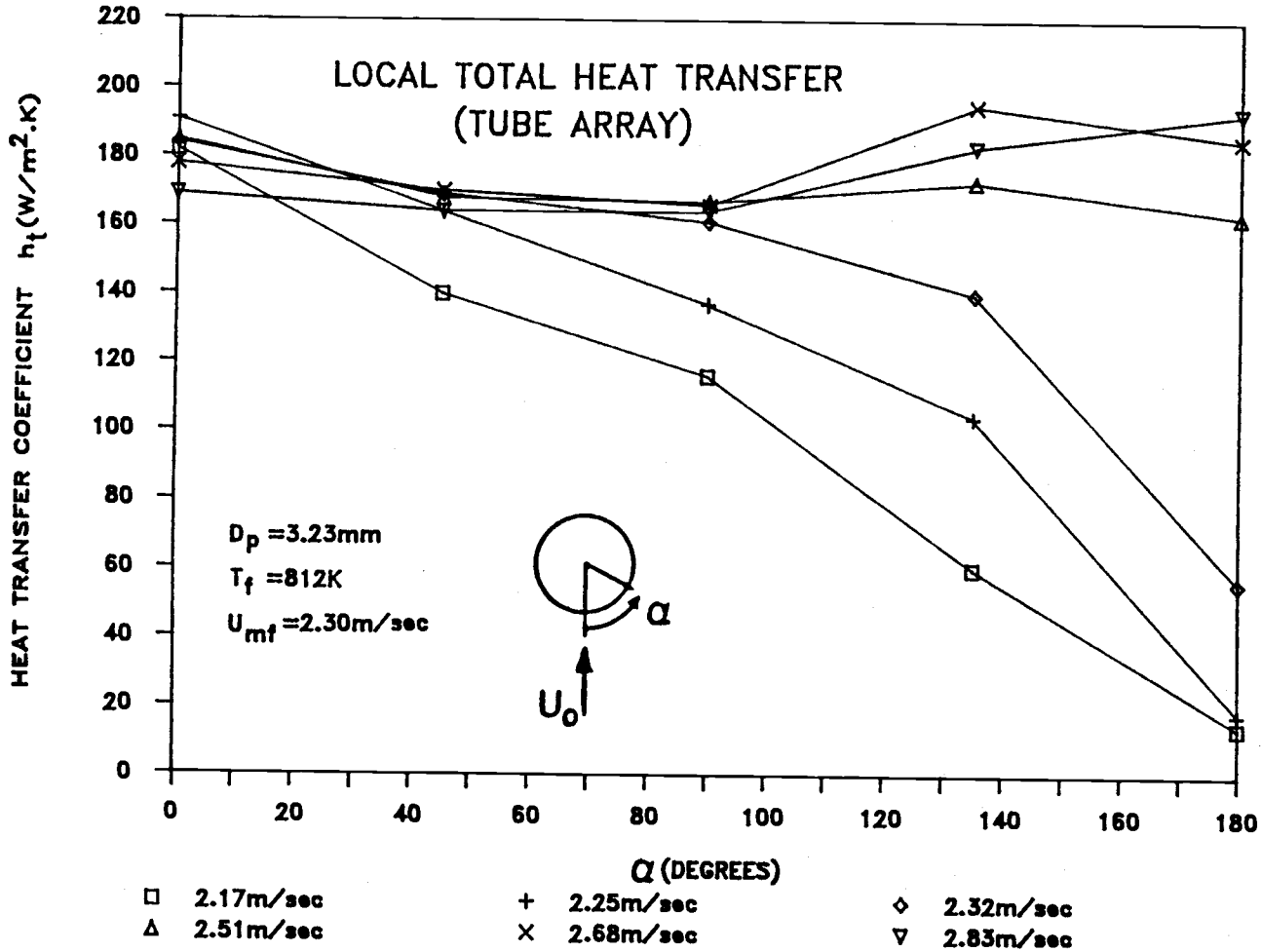

Figure 4.25 Local total heat transfer coefficient distribution for D_p = 3.23 mm, T_f = 812 K (Tube Array).

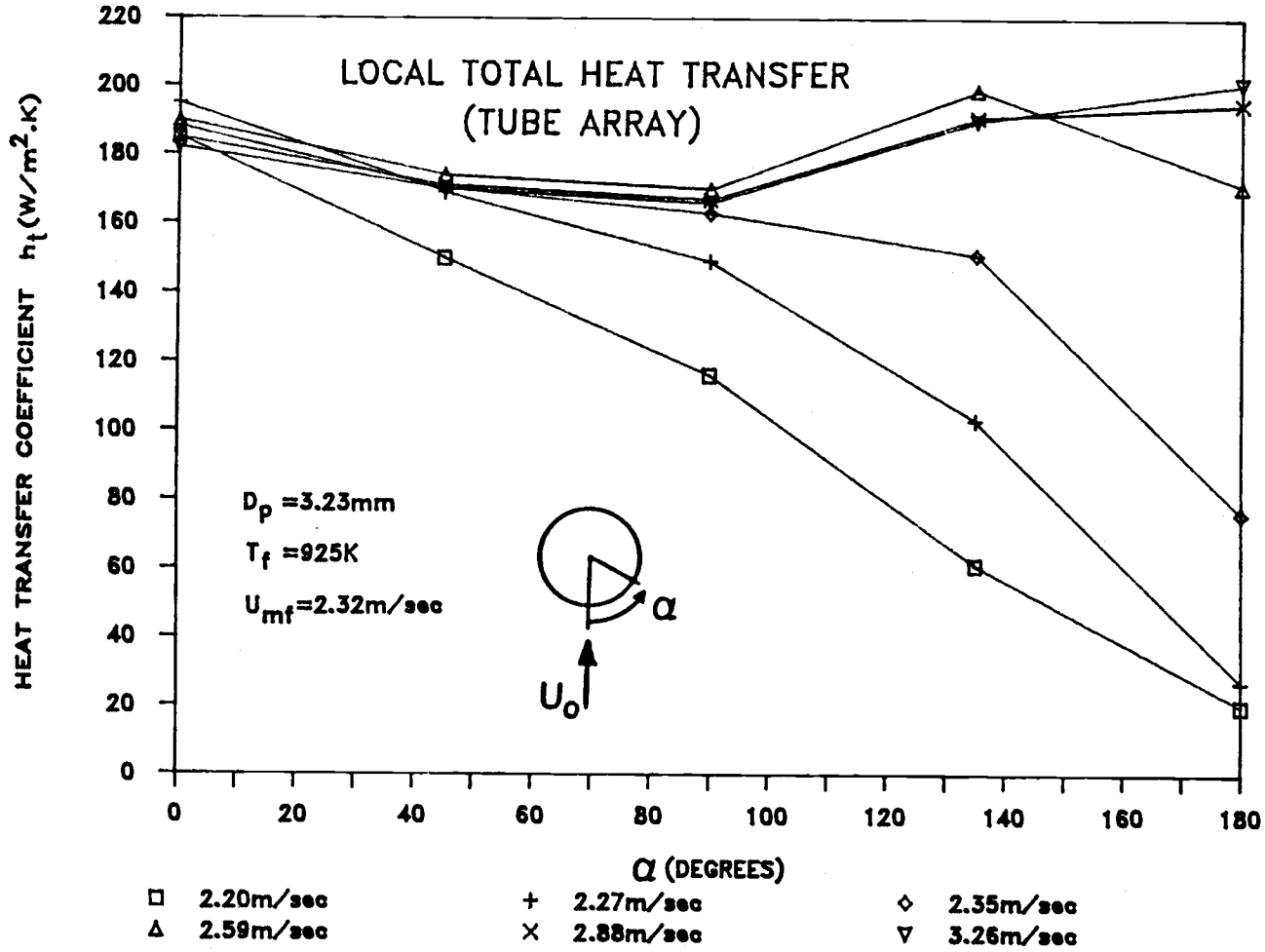

Figure 4.26 Local total heat transfer coefficient distribution for D_p = 3.23 mm, T_f = 925 K (Tube Array).

In the bubbly-bed regime ($U_o > U_{mf}$), the maximum local heat transfer coefficient ($h_{\alpha max}$) always occurred on the upper half of the tube, shifting from the equatorial lateral zone toward the downstream side of the tube at higher U_o. This observation is consistent with the results of many other investigations (9,23,46,49,66,74,78) under a variety of test conditions. As U_o reaches U_{mf}, the high rate of interaction of particles and bubbles at the lateral zone results in maximum local heat transfer (47,120). Bed porosity in this zone and the particle replacement rate in the high bed density region on the top of the tube increase significantly as U_o is raised. This behavior is responsible for the shift of $h_{\alpha max}$.

Effect of Adjacent Cool Tubes

Values of h_t for tube arrays are generally lower than for a single tube as expected although some discrepancies in the distribution of h_t were observed, which are discussed below.

The shift of $h_{\alpha max}$ is more pronounced for tube array due to the higher gas velocity between tubes in an array compared with a single tube at the same ratio of U_o/U_{mf}. Gelperin, et al. (65) noted that the "cap" of defluidized particles on top of the tubes in an array tend to become less stable, which results in $h_{\alpha max}$ being displaced more rapidly near the upper stagnation point.

Values of h_t at the lateral position for tube arrays apparently experience larger reductions due to the presence of adjacent "cool" tubes and increased bed porosity due to a higher local gas velocity in this region. The reductions are greater for smaller particles and higher temperatures.

It was also found that the distribution of h_t is more uniform for tube arrays than for a single tube, which suggests that tube arrays will provide lower thermal stress levels.

Comparison

Goshayeshi, et al. (78) conducted experiments to measure local total heat transfer coefficients (h_t) for tube arrays under the same test conditions as this study, D_p = 2.14 mm and 3.23 mm and T_f = 812 K, 922 K, and 1005 K. Experiments performed by Alavizadeh (9) and George (66) for a single tube also involved local total heat transfer measurements for D_p = 2.14 mm and 3.23 mm and T_f = 812 K and 1050 K. The range and behavior of the local total data of the present study for both the tube array and a single tube agree well with those obtained by Goshayeshi, et al. (78) and Alavizadeh (9), respectively. Similar behavior has been reported for large-particle low-temperature beds (40,46,49,66,74). For identical particle sizes, values obtained in a low-temperature bed are always lower.

V. CONCLUSIONS AND RECOMMENDATIONS

5.1 Conclusions

The time-averaged local radiative and total heat transfer coefficients have been obtained for an array of tubes as well as a single tube immersed in high-temperature large-particle beds. Experimental evidence shows that the radiative heat transfer detector employing a silicon window as a protective and transmitting medium will lead to accurate and reliable measurements of radiative heat transfer in fluidized bed.

The experimental results have been presented and discussed. It was found that the radiation heat transfer to a single tube case does not represent the results for tube arrays due to the presence of the adjacent "cool" tubes and the greater "see through" effect associated with large particles. However, the total heat transfer coefficient for tube arrays, compared with the single tube case, did decrease in the same relative amount (6% - 8%) for all the test conditions involved.

Superficial velocity had a significant effect on heat transfer coefficients measured or calculated for all cases included in this study. It was observed that the spatial-averaged heat transfer coefficients experienced a sharp increase when superficial velocity (U_o) was increased above the minimum fluidization velocity (U_{mf}) as a result of bubble-induced particle motion. The spatial-averaged total

heat transfer coefficient approached a maximum at U_o slightly above U_{mf}, and then experienced a slow decay with further increase in U_o while the spatial-averaged radiative heat transfer coefficient tended to reach an asymptotic value.

The local radiative and total heat transfer coefficients displayed more uniform distribution along the circumference of the tube at higher values of U_o. Both the radiative and total heat transfer rates at the upper half of the tube increased sharply as U_o approached U_{mf} while those at the lower stagnation point on the tube were observed to be relatively insensitive to U_o. The location of the maximum local total heat transfer coefficient shifted from the lateral zone to the downstream side as U_o was further increased. This behavior is more pronounced for tube arrays due to the higher local superficial velocity between tubes in an array.

At higher bed temperatures, the radiative heat transfer coefficient for tube arrays experienced a larger decrease than did the total heat transfer coefficient. This implies that the radiative component is more sensitive to a change in bed temperature. All heat transfer results obtained showed only minor variation with the particle sizes used in this study.

The conduction error inherent in different radiative heat transfer studies was quantified using results for local radiative heat transfer measurements employing quartz and

sapphire as window materials. Other conclusions obtained in present work are in the following:

1) The reduction in the radiation contribution with tube arrays relative to a single tube is more pronounced for larger particles and higher bed temperatures due to the greater "see through" effect of larger particles and the presence of neighboring "cool" tubes in a hot bed.
2) Local radiative heat transfer coefficients at lateral tube positions experienced a greater decrease than at other positions for tubes in an array.
3) The local radiative heat transfer coefficient was always a maximum at the lower stagnation point while values over the top half of the tube increased steadily as U_o was increased.
4) The increase in the total heat transfer coefficient with bed temperature, in large-particle beds, is due both to a greater radiation contribution and increased gas-solid convective heat transfer.
5) The distribution of local radiative and total heat transfer coefficients was insensitive to particle size, for the two sizes used in this study.
6) The shift of maximum local total heat transfer coefficient ($h_{\alpha max}$) toward the downstream side of the tube was more pronounced for tube arrays and for smaller particles.

7) Correlations based on the studies in large particle cold beds tend to underestimate the total heat transfer performance of high-temperature beds.
8) Tube emissivity plays an important role in determining the actual radiative heat transfer rate to tubes immersed in beds.

5.2 Recommendations

1) The present work could be extended to cover a wider range of particle sizes and bed temperatures, other bed materials, and different tube spacings.
2) Radiative heat transfer studies for turbulent bed conditions and/or in the free-board section are highly recommended for future work due to their practical importance in the area of circulating-fluidized-bed (CFB) combustion.
3) The effect of bed temperature on total heat transfer coefficients in large particle beds needs to be further investigated. This requires more theoretical information and experimental work about the different heat transfer mechanisms and bed hydrodynamics at elevated temperatures.
4) It is desirable to develop predictive correlations for the heat transfer to horizontal tubes immersed in large-particle high-temperature fluidized beds. However, there are many experimental studies of the effects such as tube spacing, tube size, particle

residence time, bubble contact fraction, and bubble frequency, remained to be performed in order to provide necessary information in the derivation of such correlations.

5) A radiative heat transfer study for an array of tubes immersed in small to intermediate-size particle beds (.1 mm < D_p < 2 mm) could be conducted as a continuation of the present work without difficulty. However, The fluidized bed facility used in this work precludes extension to larger particles (D_p > 4 mm) due to a limitation on the air blower capacity.

6) Some efforts should be directed toward a better understanding of radiation contributions in the bubble phase. This requires information on the radiative properties of the enclosure of a bubble and the bubble contact region.

7) It is suggested that the effect of tube spacing on local radiative heat transfer performance should be further investigated for a wider range of particle sizes and bed temperatures. Detailed physical insight of the bed hydrodynamics with immersed tubes are needed so that this effect can be theoretically and quantitatively determined.

8) The radiative detector used in this work offers the capability for fast sampling of radiation data due to its short response time (120 msec). Instantaneous

radiative heat transfer data can thus be obtained. Such information would likely provide some hydrodynamic information, such as particle residence time, bubble frequency, and bubble contact fraction, in high-temperature fluidized beds, which are needed for modeling the heat transfer mechanisms between a high-temperature fluidized bed and immersed surfaces.

9) Computers with larger memory, particular ROM space, are needed to handle the large amount of fast sampling data acquired in instantaneous measurements.

10) The effect of coolant flow rate in tubes on the total heat transfer coefficient is probably worth examining.

11) Calibration of the radiation detector should be done under a simulated bed condition to evaluate the possible errors associated with the procedure employed in this study.

12) Experimental results showed that a radiation detector employing a sapphire windows would also provide good measurements for the radiative heat flux. The use of sapphire as a window material is a possible alternative because it offers better mechanical properties than silicon. Extreme care must be used to minimize the thermal contact

resistance between this window and the tube wall due to its lower thermal conductivity (Table 2.2).

13) Some modifications of the fluidized bed facility are probably necessary so that its functions could be expanded. This includes increasing the air blower capacity, improving particle handling procedures, and an improved distributor plate design. The use of a ceramic distributor plate instead of inconel would likely solve the warping and leaking problems which occurred during this and previous studies.

BIBLIOGRAPHY

1. Adams, R. L., "An Analytical Model of Heat Transfer to a Horizontal Cylinder Immersed in a Gas Fluidized Bed," PhD Thesis, Dept. of Mech. Eng., Oregon State University, June 1977.

2. Adams, R. L., "A Gas Convection Model of Heat Transfer in Large Particle Fluidized Beds," AIChe J., Vol. 25, No. 3, May 1979, pp.395-405.

3. Adams, R. L., "An Approximate Formula for Gas Convection Dominant Heat Transfer in Large Particles Fluidized Beds," J. of Heat Transfer, Vol. 101, May 1981, pp.395-397.

4. Adams, R. L., "Extension of the Adams-Welty Fluid Bed Heat Transfer Model to the Packed Bed Case," J. of Heat Transfer, Vol. 103, Aug. 1981, pp.602-604.

5. Adams, R. L., "An Approximate Model of Bubble Phase Convective Heat Transfer to a Horizontal Tube in a Large Particles Fluidized Bed," J. of Heat Transfer, Vol. 104, Aug. 1982, pp.565-67.

6. Adams, R. L., "Coupled Gas Convection and Unsteady Conduction Effects in Fluid Bed Heat Transfer Based on a Single Particle Model," Int. J. of Heat and Mass Transfer, Vol 25, No. 12, 1982, pp.1819-28.

7. Adams, R. L., "Heat Transfer in Large Particle Bubbling Fluidized Beds," J. of Heat Transfer, Vol 106, Feb. 1984, pp.85-90.

8. Adolf Meller Company Catalog, Providence, RI, USA, 1984.

9. Alavizadeh, N., "An Experimental Investigation of Radiative and Total Heat Transfer Around a Horizontal Tube," Ph.D. Thesis, Dept. of Mech. Eng., Oregon State University, Aug. 1985.

10. Alavizadeh, N., "A Quick Reference User's Manual Guide for HP-3497A Data Logger and HP-85 Microcomputer," Dept. of Mech. Eng., Oregon State University, Corvallis, OR, 97331, 1985.

11. Alavizadeh, N., Adams, R. L., Welty, J. R. and Goshayeshi, A., "An Instrument for Local Radiative Heat Transfer Measurement in a Gas-Fluidized Bed at Elevated Temperatures," New Experimental Techniques in Heat Transfer, The 22nd National Heat Transfer Conf. and Exhibition, Niagara Falls, NY, Aug. 1984, pp.1-8.

12. Alavizadeh, N., Fu, Z., Adams, R. L., Welty J. R., and Goshayeshi, A., "Radiative Heat Transfer Measurement for a Horizontal Tube Immersed in Small and Large Particle Fluidized Beds," The 5th Int. Heat Transfer Sym., Beijing, China, Oct. 1985.

13. Analog Devices, Inc., Macsym ADIO Library, STB02 Termination Panel, Norwood, MI, 1980.

14. Babu, S. P., Shah, B. and Talwalker, A., "Fluidization Correlations for Coal Gasification Materials--Minimum Fluidization Velocity and Fluidized Bed Expansion Relation," AIChe Sym. Ser., Vol. 74, No. 176, 1978, pp.176-86.

15. Bakke, P. A., "A Simplified Model of Heat Transfer Between Large-Particles Gas-Fluidized Beds and Immersed Surfaces," MS Thesis, Dept. of Mech. Eng., Oregon State University, April, 1986.

16. Barnes Engineering Company, "Infrared Radiation Reference Source Model 11-210," Instruction Manual, Stamford, Connecticut.

17. Bartel, W. J. and Genetti, W. E., "Heat Transfer from a Horizontal Bundle of Bare and Finned Tubes in an Air Fluidized Bed," AIChe Sym. Ser., Vol. 69, No. 128, 1973, p.85.

18. Baskakov, A. P., Berg, B. V., Vitt, O. K., Filippovsky, N. F., Kirakosyan, V, A., Goldobin, J. M. and Maskaev, V. K., "Heat Transfer to Objects Immersed in Fluidized Beds," Powder Tech., Vol. 8, 1973, pp.273-82.

19. Baskakov, A. P. and Suprun, V. M., "Determination of the Convective Component of the Heat Transfer Coefficient to a Gas in a Fluidized Bed," Int. Chem. Eng., Vol. 12, 1972, p.324.

20. Basu, P., "Bed to Wall Heat Transfer in a Fluidized Bed Coal Combustor," AIChe Sym. Ser., Vol. 74, No. 176, 1978, pp.187-93.

21. Basu, P., Fluidized Bed Boilers: Design and Application, Pergamon Press, Canada Ltd., 1984.

22. Basu, P., "Circulating Fluidized Bed Technology," Proce. of First Int. Conf. on Circulating Fluidized Beds, Halifax, Nova Scotia, Canada, Nov., 1985, Pergamon Press Canada Ltd., 1986.

23. Berg, B. V. and Baskakov, A. P., "Investigation of Local Heat Transfer Between a Fixed Horizontal Cylinder and a Fluidized Bed," Int. Chem. Eng., Vol. 14, No.3, July 1974, pp.440-43.

24. Bhattacharya, S. C. and Harrison, D., "Heat Transfer in High Temperature Fluidized Beds," European Congress on Particle Technology, Nuremberg, 1977.

25. Borodulya, V. A., Ganzha, V. L., "Heat Transfer from In-Land and Staggered Horizontal Smooth Tube Bundles Immersed in a Fluidized Bed of Large Particles," Int. J. of Heat and Mass Transfer, Vol 23, 1980, pp.1602-04.

26. Borodulya, V. A., Ganzha, V. L. and Podberezsky, A. I., "High Pressure Heat Transfer Investigations for Fluidized Beds of Large Particles and Immersed Vertical Tube Bundles," Int. J. of Heat and Mass Transfer., Vol. 26, No. 11, 1983, pp.1577-84.

27. Borodulya, V. A., Ganzha, V. L., Podberezsky, A. I., Upadhyay, S. N., and Saxena, S. C., "Heat Transfer between Fluidized Beds of Large Particles and Horizontal Tube Bundles at High Pressure," Int. J. of Heat and Mass Transfer, Vol. 27, No. 8, 1984, pp.1219-25.

28. Borodulya, V. A. and Kovensky, V. I., "Radiative Heat Transfer Between a Fluidized Bed and a Surface," Int. J. of Heat and Mass Transfer, Vol 26, No. 2, 1983, pp.277-87.

29. Borodulya, V. A., Kovensky, V. I., and Makhorin, K., "Fluidized Bed Radiative Heat Transfer," Proc. of the 4th Int. Conf. on Fluidization, Japan, June, 1983, pp.379-88.

30. Botterill, J. S. M., Fluidized-Bed Heat Transfer, Academic Press, NY, 1975.

31. Botterill, J. S. M., and Denloye, A. O. O., "A Theoretical Model of Heat Transfer to a Packed or Quiescent Fluidized Bed," Chem. Eng. Sci., Vol.33, 1978, pp.509-15.

32. Botterill, J. S. M., and Denloye, A. O. O., "Gas Convective Heat Transfer to Packed and Fluidized Beds," AIChe Sym. Ser., Vol. 74, No. 176, 1978, pp.194-202.

33. Botterill, J. S. M. and Sealey, C. J., "Radiative Heat Transfer Between a Gas Fluidized Bed and an Exchange Surface," British Chem. Eng., Vol. 15, No. 2, 1970, pp.1167-68.

34. Botterill, J. S. M. and Williams, J. R., "The Mechanism of Heat Transfer to Gas Fluidized Bed," Trans. Inst. Chem. Engrs., Vol. 41, 1963, pp.217-30.

35. Brewster, M. Q., "Radiative Heat Transfer in Fluidized-Bed Combustors," ASME paper No. 83-WA/HT-82, 1982.

36. Brewster, M. Q. and Tien, C. L., "Radiative Transfer in Packed Fluidized Bed: Dependent Versus Independent Scattering," J. of Heat Transfer, Vol. 104, Nov. 1982, pp.573-79.

37. Brown, E. A., Charlson, R. J. and Johnson, D. L., "Steady-State Heat Flux Gauge," The Review of Scientific Instruments, Vol. 32, 1961, pp.984-85.

38. Canada, G. S. and Mclaughtin, M. H., "Large Particle Fluidization and Heat Transfer at High Pressures," AIChe Sym. Ser., Vol. 74, No. 176, 1978, pp.27-37.

39. Catipovic, N. M., "A Study of Heat Transfer to Immersed Tubes in Fluidized Beds," AIChe 71st Annual Meeting, Miami FL, Nov. 1978, 34p.

40. Catipovic, N. M., "Heat Transfer to Horizontal Tubes in Fluidized Beds," PhD. Thesis, Dept. of Chem. Eng., Oregon State University, March 1979.

41. Catipovic, N. M., Fitzgerald, T. J., George, A. H. and Welty, J. R., "Experimental Validation of the Adams-Welty Model for Heat Transfer in Large-Particle Fluidized Beds," AIChe J., Vol. 28, No. 5, 1982, pp.714-20.

42. Catipovic, N. M., Jovanovic, G. N., and Fitzgerald, T. J., "Regimes of Fluidization for Large Particles," AIChe J., Vol. 24, No. 3, May 1978, pp.543-47.

43. Chandran, R. and Chen, J. C., "Bed-Surface Contact Dynamics for Horizontal Tubes in Fluidized Beds," AIChe J., Vol. 28, No. 6, 1982 pp.907-12.

44. Chandran, R. and Chen, J. C., "A Heat Transfer Model for Tubes Immersed in Gas Fluidized Beds," AIChe J., Vol. 31, No. 2, 1985, p.244.

45. Chandran, R. and Chen, J. C., "Influence of the Wall on Transient Conduction into Packed Media," AIChe J., Vol. 31, No. 1, 1985, p.168.

46. Chandran, R., Chen, J. C. and Staub, F. W., "Local Heat Transfer Coefficient Around Horizontal Tubes in Fluidized Beds", J. of Heat Transfer, Vol. 102, Feb. 1980, pp.152-57.

47. Chen, J. C., "Heat Transfer to Tubes in Fluidized Beds," ASME National Heat Transfer Conf., Paper No. 76-HT-75, 1975.

48. Chen, J. C. and Chen, K. L., "Analysis of Simultaneous Radiative and Conductive Heat Transfer in Fluidized Beds," Chem. Eng. Commun., Vol. 9, No.1, 1981, pp.255-71.

49. Cherrington, D. C., Golan, L. P. and Hammitt, F. G., "Industrial Application of Fluidized Bed Combustion--Single Tube Heat Transfer Study,". Proc. of the 5th Int. Conf. on Fluidized Bed Combustion, Vol 3, Dec. 1977, pp.184-209

50. Chung, B. T. F., Fan, L. T. and Hwang, C. L., "A Model of Heat Transfer in Fluidized Beds," J. of Heat Transfer, Feb. 1972, pp.105-10.

51. Davidson, J. F. and Harrison, D., Fluidization, Academic Press, London, pp.517-540, 1971.

52. Decker, N. A. and Glicksman, L. R., "Conduction Heat Transfer at the Surface of Bodies Immersed in Gas Fluidized Beds of Spherical Particles,". AIChe Sym. Ser., Vol. 77, No. 208, 1981, pp.341-49.

53. Decker, N. A. and Glicksman, L. R., "Heat Transfer in Large Particle Fluidized Beds," Int. J. of Heat and Mass Transfer, Vol. 26, No. 9, 1983, pp.1307-20.

54. Denloye, A. O. O. and Botterill, J. S. M., "Bed to Surface Heat Transfer in a Fluidized Bed of Large Particle," Powder Tech., Vol. 19, 1978, pp.197-203.

55. Doebelin, E. O., Measurement systems Application and Design, Revised Edition, Mcgraw-Hill, NY, 1975.

56. Dow, W. M. and Jakob, M., "Heat Transfer Between an Vertical Tube and a Fluidized Air-Solid Mixture," Chem. Eng. Prog., Vol. 47, No. 12, 1951, p.637.

57. Dunsky, V. D. and Tamarin, A. I., "Heat and Mass Transfer in Disperse Systems," Nauka i Tekh., Minsk, 1965.

58. Fatani, A. A., "An Analytical Model of Radiative and Convective Heat Transfer in Small and Large Particle Gas Fluidized Beds," PhD Thesis, Dept. of Mech. Eng., Oregon State University, Oct. 1983.

59. Figliola, R. S. D., Beasley, D. E. and Subramaniam, C., "Instantaneous Heat Transfer Between an Immersed Horizontal Tube and a Gas fluidized Bed," ASME/AIChe Heat Transfer Conf., Paper No. 84-HT-111. Niagara Fall, NY, 1984.

60. Gabor, J. D., "Wall to Bed Heat Transfer in Fluidized Bed and Packed Bed," Chem. Eng. Prog. Sym. Ser., Vol. 66, No. 105, pp.76-86.

61. Galloway, T. R. and Sage, B. H., "A Model of the Mechanism of Transport in Packed Distended and Fluidized Bed," Chem Eng. Sci., Vol. 25, pp.495-516.

62. Ganzha, V. L., L'hpadhyay, S. N. and Saxena, S. C., "A Mechanistic Theory for Heat Transfer Between Fluidized Beds of Large Particles and Immersed Surfaces," Int. J. of Heat and Mass Transfer, Vol. 15, 1982, pp.1531-40.

63. Gelperin, N. I., Einshtein, V. G., "Heat Transfer in Fluidized Bed," in Fluidization, Editors, Davidson, J. F. and Harrison, D., Academic Press, London, 1971. pp.517-40.

64. Gelperin, N. I., Einshtein, V. G., and Korotyanskaya, L. A., "Heat Transfer Between a Fluidized Bed and Tube Bundles with Various Tube Arrangements," in Russian, Zh. Vses. Khim. Obshchest., Vol. 14, No. 1, 1969, p.120.

65. Gelperin, N. I., Einshtein, V. G., and Zaikovskii, A. V., "Hydraulic and Heat Transfer Characteristics of a Fluidized Bed with a Horizontal Tube Bundle," J. of Eng. Phy. Vol. 10, 1966, pp.473-75.

66. George, A. H., "An Experimental Study of Heat Transfer to a Horizontal Tube in a Large Particle Fluidized Bed at Elevated Temperature," PhD Thesis, Dept. of Mech. Eng., Oregon State University, June 1981.

67. George, A. H., "Documentation for the OSU High Temperature Fluidized Bed Facility," Dept of Mech. Eng., Oregon State University, Aug. 1981.

68. Ghafourian, M. R., "Determination of Thermal Conductivity, Specific Heat, and Emissivity of Ione Grain," MS Project, Dept. of Mech. Eng., Oregon State University, June 1984.

69. Glass, D. H. and Harrison, D., "Flow Patterns Near a Solid Obstacle in a Fluidized Bed," Chem. Eng. Sci., Vol. 19, 1964, pp.1001-02.

70. Glicksman, L. R., "Heat Transfer in Fluidized Bed Combustors," in Fluidized Bed Boilers: Design and Application, Editor, Basu, P., Pergamon Press, 1984, pp.63-100.

71. Glicksman, L. R. and Decker, N., "Design Relationships for Predicting Heat Transfer to Tube Bundles in Fluidized Bed Combustors," Proc. 6th Int. Conf. on Fluidized Bed Combustion, Atlanta, GA, April, 1980, Vol. 3, pp.1152-57.

72. Glicksman, L. R. and Decker, N. A., "Heat Transfer from an Immersed Surface to Adjacent Particles in a Fluidized Bed; the Role of Radiation and Particle Packing," Proc. of 7th Int. Heat Transfer Conf., Munich, Vol. 6, 1982, pp.45-50.

73. Goblirsch, G. and Vander, R. H., "Atmospheric Fluidized Bed Combustion Testing of North Dakota Lingnite," The 6th Int. Fluidized Bed Conf., Atlanta GE, April 1980, 13p.

74. Golan, L. P. and Cherrington, D, C., "Heat Transfer and Unit Response of a Large Fluidized Bed Combustor," AIChe Sym. Ser., Vol. 77, No. 208, 1981, pp.374-83.

75. Golan, L. P., Lalonde, G. V. and Weiner, S. C., "High Temperature Heat Transfer Studies in a Tube Filled Bed," Proc. 6th Int. Conf. on Fluidized Bed Combustion, Atlanta, GA, Vol. 3, April, 1980, pp.1173-85.

76. Gosmeyer, C. D., "An Experimental Study of Heat Transfer in a Large Particle Heated fluidized Bed," MS Thesis, Dept. of Chem. Eng., Oregon State University, Sept. 1979.

77. Goshayeshi, A., "An Experimental Study of Heat Transfer with an Array of Horizontal Tube Immersed in a High Temperature Fluidized Bed at Elevated Temperatures," PhD Thesis, (to be published), Dept. of Mech. Eng., Oregon State University, 1987.

78. Goshayeshi, A., Welty, J. R., Adams, R. L., Alavizadeh, N., "Local Heat Transfer Coefficients for Horizontal Tube Arrays in High Temperature Large Particle Fluidized Bed - An Experimental Study," 23rd ASME/AIChe National Heat Transfer Conference, Denver, CO. Aug. 1985.

79. Grewal, N. S., "Heat Transfer Between Tubes and Gas-Solid Fluid Beds," Dept. of Mech. Eng., University of North Dakota 58202, 1984.

80. Grewal, N. S. and Goblirsch, G., "Heat Transfer to Horizontal Tubes in a Pilot-Scale Fluidized-Bed Combustor Burning Low Rank Coals," ASME/AIChe National Heat Transfer Conf., Paper No. 83-HT-91, Dec. 1983.

81. Grewal, N. S. and Hajicek, D, R., "Experimental Studies of Heat Transfer from an Atmospheric-Fluidized Bed Combustor to an Immersed Array of Horizontal Tubes," The 7th Int. Heat Transfer Conf., Paper No. HX23, 1983, Munchen, Germany, pp. 295-300.

82. Grewal, N. S. and Saxena, S. C., "Experimental Studies of Heat Transfer between a Bundle of Horizontal Tubes and a Gas-Solid Fluidized Bed of Small Particles," Ind. Eng. Chem. Proc. Design and Development, Dec. 1983, Vol. 22, pp.367-76.

83. Hager, N. E., "Thin Foil Heat Meter," The Review of Scientific Instruments, Vol. 36, No. 11, Nov. 1965, pp. 1564-70.

84. Hager, W. R. and Schrag, S. D., "Particle Circulation Downstream from a Tube Immersed in a Fluidized Bed," Chem. Eng. Sci., Vol. 31, 1976, pp.657-59.

85. Hager, W. R. and Thomson, W. J., "Bubble Behavior Around Immersed Tubes in a Fluidized Bed," AIChe Sym. Ser., Vol. 69, No. 128, 1973, pp.68-77.

86. Harakas, N. K. and Beatty, Jr., K. O., "Moving Bed Heat Transfer : Effect of Interstitial Gas with Fine Particles," Chem. Eng. Prog. Sym. Ser., Vol. 59, No. 41, 1963, pp.122-28.

87. Hewlett Packard Co., Practical Temperature Measurement, Application Note 290, Aug. 1980.

88. Howard, J. R., Fluidized Bed: Combustion and Application, Applied Science Publishers Ltd., London, 1983.

89. Hy-Cal Engineering Co., Catalog No. CF-991.3, Santafa Spring, CA, 1981.

90. Ilchenko, A. I., Pikashov, V. S. and Makhorin, K. E., "Study of Radiative Heat Transfer in Fluidized Beds," J. of Eng. Physics, Vol. 14, 1968, pp.321-24.

91. Jovanovic, G. N., "Gas Flow in Fluidized Beds of Large Particles: Experiment and Theory," PhD Thesis, Dept. of Chem. Eng., Oregon State University, March 1979.

92. Jovanovic, G. N. and Catipovic, N. M., "A New Approach in Classifying Solids in Bubbling Gas-Fluidized Beds," in Fluidization, editor, Kunii, D. and Toei R., Proc. of the 4th Int. Conf. on Fluidization, United Eng. Trustees, Inc., 1984.

93. Junge, D. C., "Design and Operation of OSU High Temperature Fluidized Bed Facility," Dept. of Mech. Eng., Oregon State University, Aug. 1978.

94. Keairns, D. L., unpublished paper, Westinghouse Research Laboratory, Pittsburgh, Penn. USA, 1970.

95. Kharchenko, N. V. and Makhorin, K. E., "The Rate of Heat Transfer Between a Fluidized Bed and an Immersed Body at High Temperatures," Int. Chem. Eng., Vol. 4, No. 4, Oct. 1964, pp.650-54.

96. Kolar, A. K., Grewal, N. S. and Saxena, S, C., "Investigation of Radiative Contribution in a High Temperature Fluidized Bed Using the Alternate-Slab-Model," Int. J. Heat and Mass Transfer, Vol. 22, 1979, pp. 1695-1703.

97. Ku, A. C., Kuwata, M. and Staub, F. W., "Heat Transfer to Horizontal Tube Banks in a Turbulent Fluidized bed of Large Particles," AIChe Sym. Ser., Vol. 77, No. 208, 1981, pp.359-73.

98. Kubie, J. and Broughton, J., "A Model of Heat Transfer in Gas Fluidized Beds," Int. J. of Heat and Mass Transfer, Vol. 18, 1975, pp.289-99.

99. Kunii, D. and Levenspiel, O., Fluidization Engineering, John Wiley & Sons, 1969

100. Kunii, D. and Toei, R., Editors, Fluidization: Proc. of the 4th Int. Conf. on Fluidization, May 1983, Japan, Engineering Foundation, United Eng. Trustees, Inc., 1984.

101. Leon, A. M., Choksey, P. J. and Bunk, S. A., "Design, Construction, Operation, and Evaluation of a Prototype Culm Combustion Boiler/Heater Unit," Report FE 3269-9A, Dorr-Oliver, Inc., Stamford, Connecticut.

102. Levenspiel, O. and Walton, J. S., "Bed-Wall Heat Transfer in Fluidized Systems," Chem. Eng. Prog. Sym., Vol. 50, No. 9, pp.1-13.

103. Loew, O., Shmutter, B. and Resnick, W., "Particle and Bubble Behavior and Velocities in a Large-Particles Fluidized Bed with Immersed Obstacles," Powder Tech., Vol. 22, 1979, pp.45-57.

104. Mahbod, B., "A Theoretical Study of the Radiative Contribution to Heat Transfer Between a High Temperature, Large Particle Gas Fluidized Bed and an Immersed Tube", PhD Thesis, Dept. of Mech. Eng., Oregon State University, April 1984.

105. Mahbod, B. and Adams, R. L., "A Model of Radiative Contribution to Heat Transfer in a High-Temperature, Large-Particle Gas Fluidized Bed," ASME/AIChe National Heat Transfer Conf., Aug. 1984.

106. Mahbod, B., Tabesh, T. and Goshayeshi, A., "An Analytical Model for Prediction of Radiative Heat Transfer in Large-Particle Gas Fluidized Beds with an Embedded Horizontal Tube," AIChe Sym. Ser., Vol. 81, No. 245, 1985, p.26.

107. Makansi, J., Schwieger, R., "Fluidized Bed Boiler," Power, Vol. 131, No. 5, May 1987, pp.1-15.

108. Martin, H., "Heat & Mass Transfer in Fluidized Beds," Int. Chem. Eng., Vol. 22, No. 1, pp.30-43, 1982.

109. Maskaev, V. K. and Baskakov, A. P., "Features of External Heat Transfer in a Fluidized Bed of Coarse Particles," Int. Chem. Eng., Vol. 14, No. 1, Jan. 1974, pp.80-83.

110. McLaren, J. and Williams, D. F., "Combustion Efficiency, Sulphur Retention and Heat Transfer in Pilot-Plant Fluidized-Bed Combustors," J. of the Institute of Fuel, Vol. 42, 1969, pp.303-08.

111. Mickley, H. S. and Fairbanks, D. F., "Mechanism of Heat Transfer to Fluidized Beds," AIChe J., Vol. 1, Sept. 1955, pp.374-84.

112. Neter, J., Wasserman, W., and Kutner, M. H., Applied Linear Regression Models, Richard D. Irwin, Inc., Homewood, IL, 1983.

113. Newby, R. A., Keairns, D. L. and Ahmed, M. M., "The Selection of Design and Operations for Industrial AFBC to Meet Environmental Constraints," Proc. of DOE/WYU Conf. on Fluidized Bed Combustion System Design and Operation, 1980, pp.59-133.

114. Ozkaynak, T. F., "An Experimental Investigation of Radiation Heat Transfer in a High Temperature Fluidized Bed," Proce. of 4th Int. Conf. on fluidization, Japan, May 1983, pp.371-78.

115. Peeler, J. P. K. and Whitehead, A. B., "Solids Motion at Horizontal Tube Surfaces in a Large Gas-Solid Fluidized Bed," Chem. Eng. Sci., Vol. 17, No. 1, 1982, pp.77-82.

116. Petrie, J. C., Freeby, W. A. and Buckham, J. A., "In Bed Heat Exchangers," Chem. Eng. Prog, Vol. 64, No. 7. July 1968, pp.45-51.

117. Pikashov, V. S., Zabrodsky, S. S., Makhorin, K. E., and Ilchenko, A. I., "On the Experimental Study of the Fluidized Bed Effective Emissivity," Heat and Mass Transfer, Vol. 5, Nauka i Teckhn. Minsk. 1968.

118. Pikashov, V. S., Zabrodsky, S. S., Makhorin, K. E., and Ilchenko, A. I., Bulletin of BSSR., Academy of Science, Physical Energetics, Series 100, No. 2, 1969, p.100.

119. Pillai, K. K., "A Radiative Packet Model for Heat Transfer in Fluidized Beds," The 6th Int. Conf. on Fluidized Bed Combustion, Vol. 3, April, 1980, pp.1081-91.

120. Rowe, P. N., "Prediction of Bubble Size in a Gas Fluidized Bed," Chem. Eng. Sci., Vol. 31, 1976, pp.285-288.

121. Samson, T., "Heat Transfer to Objects in Fluidized Beds," Congress International Fluidization and Its Application, Vol. 1, Toulouse, France, Oct. 1973.

122. Saxena, S. C., Grewal, N. S. and Gabor, J. D., "Heat Transfer Between a Gas Fluidized Bed and Immersed Tubes," Advances in Heat Transfer, Vol. 14, 1978, Academic Press, pp.149-247.

123. Schlunder, E. V., "Heat Transfer to Moving Spherical Packings at Short Contact Times," Int. Chem. Eng., Vol. 20, No. 4, 1980, p.550.

124. Schwieger, R. G., Editor, "Fluidized Bed Combustion and Applied Technology," First Int. Fluidization Sym., Beijing, China, Aug. 1983, Mcgraw Hill, NY, 1984.

125. Siegel, R. and Howell, J. R., Thermal Radiation Heat Transfer, 2nd Edition, Hemisphere, NY,1981.

126. Staub, F. W., "Solids Circulation in Turbulent Fluidized Beds and Heat Transfer to Immersed Tube Banks," ASME J. of Heat Transfer, Vol. 101, 1979, pp.391-96.

127. Strom, S. S., Dowdy, T. E., Lapple, W. C., Kitto J. B., Stanoch, T. P., Boll, R. H., and Sage, W. L., "Preliminary Evaluation of Atmospheric Pressure Fluidized Bed Combustion Applied to Electric Utility Large Steam Generators," EPRI Report No. RP 412-1, Electric Power Research Institute, Palo Alto, CA, Feb. 1977.

128. Szekely, J. and Fisher, R. J., "Bed to Wall Radiation Heat Transfer in a Gas-Solid Fluidized Bed," Chem. Eng. Sci., Vol. 24, 1969, pp.833-49.

129. Tang, J. T. and Howe, W., "Heat Transfer Analysis for the 6'x6' Atmospheric Fluidized Bed Development Facility," ASME/AIChe National Heat Transfer Conf., Paper No. 80-HT-128, Orlando, Florida, July, 1980.

130. Temperature Measurement Handbook 1985, Omega Engineering, Stamford, Connecticut, 1985.

131. Vadivel, R. and Vedamurthy, V. N., "An Investigation of the Influence of Bed Parameters on the Variation of the Local Radiative and Total Heat Transfer Around an Embedded Horizontal Tube in a Fluidized Bed Combustor," Proc. of 6th Int. Conf. on Fluidized Bed Combustion, Vol. 3, Atlanta GA, USA, April 1980.

132. Van Heerden, C., Nobel, P. and Van Krevelen, D. W., "Mechanism of Heat Transfer in Fluidized Beds," Ind. Eng. Chem., Vol. 45, 1953, pp.1237-42.

133. Varygin, N. N. and Martyushin, I. G., "A Calculation of Heat Transfer Surface Area in Fluidized Bed Equipment," Khim, Mashinostinostroenie, No. 5, 1959, pp.6-9.

134. Vedamurthy, V. N. and Sastri, V. M. K., "An Analysis of the Conductive and Radiative Heat Transfer to the Walls of Fluidized Bed Combustors," Int. J. of Heat and Mass Transfer, Vol. 17, No. 1, 1974, pp.1-9.

135. Vedamurthy, V. N. and Sastri, V. M. K., "An Experimental Study of the Influence of Bed Parameters on Heat Transfer in a Fluidized Bed Combustor," Fluidized Bed Library, New York University, pp.589-97.

136. Wen, C. Y. and Leva, M., "Fluidized Bed Heat Transfer: A Generalized Dense-Phase Correlation," AIChe. J., Vol. 2, No. 4, Dec. 1956.

137. Welty, J. R., "Heat Transfer in High Temperature Fluidized Beds with Immersed Tubes of Coal Combustion Service," Annual Report to US Dept. of Energy, No. FE-2714-5, 1978.

138. Welty, J. R., "Heat Transfer in Large Particle Fluidized Beds," US/CHINA Binational Heat Transfer Workshop, Editors, Wu, Z., Wand, B., Tien, C. L., and Yang, K. T., Oct., 1983. pp.148-62.

139. Welty, J. R., Adams, R. L., Lei, D. H. S. and Bakke, P. A., "A Study of the Radiative Contribution to Heat Transfer Between a High-Temperature Fluidized Bed and an Array of Immersed Tube," Final Report to NSF, Dept. of Mech. Eng., Oregon State University, July 1986.

140. Welty, J. R., Wicks, C. E., and Wilson, R. E., Fundamental of Momentum, Heat , and Mass Transfer, 3rd Edition, John Wiley & Sons, Inc., 1984.

141. Wright, S. J., Hickman, R. and Ketley, H. C., "Heat Transfer in Fluidized Beds of Wide Size Spectrum at Elevated Temperatures," British Chem. Eng., Vol. 15, No. 12, 1970, pp.1551-54.

142. Wright, S. J., Ketley, H. C. and Hickman, R. G., "The Combustion of Coal in Fluidized Beds for Firing Shell Boiler," J. of the Institute of Fuel, June 1969, pp.235-40.

143. Yoshida, K., Kunii, D. and Levenspiel, O., "Heat Transfer Mechanisms Between Wall Surface and Fluidized Bed," Int. J. of Heat and Mass Transfer, Vol. 12, 1969, pp.529-31.

144. Yoshida, K., Ueno, T. and Kunii, D., "Mechanism of Bed-Wall Heat Transfer in a Fluidized Bed at High Temperatures," Chem. Eng. Sci., Vol. 29, 1974, pp.77-82.

145. Zabrodsky, S. S., Hydrodynamics and Heat Transfer in Fluidized Beds, Translation Editor, Zenz, F. A., The MIT Press, MA, USA. 1966.

146. Zabrodsky, S. S., "Compound Heat Exchange Between a High Temperature Gas-Fluidized Bed and a Solid Surface," Int. J. of Heat and Mass Transfer, Vol. 16, 1973, pp.241-48.

147. Zabrodsky, S. S., Antonishin, N. V., Vasiliev, G. M., and Paranas, A. L., "The Choice of Design Correlation for the Estimation of the High-Temperature Fluidized Bed-to-Immersed Body Heat Transfer Coefficient," Vestn. Akad. Nank. USSR, Ser. Fiz-Energ. Nauk No. 4, 1974, pp.103-07.

148. Zabrodsky, S. S., Epanov, Y. G. and Galershtein, D. M., "Heat Transfer in a Large Particle Fluidized Bed with Immersed In-Line and Staggered Bundles of Horizontal Smooth Tubes," Int. J. of Heat and Mass Transfer, Vol. 24, No. 4, Nov. 1981, pp.571-79.

149. Ziegler, E. N. and Brazelton, W. T., "Mechanism of Heat Transfer to Fixed Surfaces in Fluidized Beds," Ind. Engr. Chem. Fundamentals, Vol. 3, 1964, pp.94-98.

150. Ziegler, E. N., Koppel, L. B. and Brazelton, W. T., "Effects of Solid Thermal Properties on Heat Transfer to Gas Fluidized Beds," Ind. Engr. Chem. Fundamentals, Vol. 3, No.4, Nov. 1964, pp.324-28.

APPENDICES

APPENDICES

Appendix A. Temperature and Heat Flux Conversion

The heat flux sensors (No. 204551-1, RdF, Inc.) employed in this study are self-generating transducers, requiring no reference junction, signal conditioning, or special wiring. The use of a HP-3497A high precision data logger also aided in obtaining maximum resolution. Each heat flux sensor was furnished with a ANSI type T (copper-constantan) thermocouple and two multi-junction thermopiles. A discussion of the conversion of voltage reading to temperature and heat flux follows.

A.1 Sensor Surface Temperature

A software compensation (87) was used in the sensor surface temperature (T_s) measurements. The temperature-voltage relationship of any type of thermocouple is nonlinear. Better conversion accuracy can be obtained by storing the thermocouple table provided by National Bureau of Standards (130) in the computer (87). A more viable approach is to approximate the table values using a power series polynomial. The voltage readings were converted to temperature employing a polynomial fit for the type T thermocouple in the heat flux sensor (9). In equation (A.1), V_t is the thermocouple voltage reading, and V_{ref} is the reference voltage obtained by converting reference temperature to equivalent thermocouple voltage (82).

$$T_s\ (^oC) = C_1E + C_2E^2 + C_3E^3 + C_4E^4 \qquad (A.1)$$

Where $C_1 = 2.56613 \times 10^{-2}$

$C_2 = -6.19549 \times 10^{-7}$

$C_3 = 2.21816 \times 10^{-11}$

$C_4 = -3.55009 \times 10^{-16}$

$E = (V_t + V_{ref}) \times 10^{6}$ (E in μV)

This polynomial fit has an accuracy of ±0.5 ^oC for temperatures between 0 ^oC and 200 ^oC, which is within the range of the sensor surface temperatures encountered in this study.

A.2 Heat Flux

The heat transfer rate detected by the heat flux sensor, Q_d, is calculated from the following voltage-to-heat flux conversion equation:

$$Q_d = \frac{F(T_s) \times V_d}{C_s} \qquad (A.2)$$

Where Q_d : Detected heat flux (W/m^2)

F_s : Multiplication factor

V_d : Detected thermopile voltage (μV)

C_s : Sensitivity constant ($\mu V.m^2/W$)

The multiplication factor, $F(T_s)$, is a compensation for the change of thermopile conductivity with heat flux sensor surface temperature (T_s). It is supplied by the manufacture in a plot of F vs. T_s. A second-order polynomial fit was performed to approximate $F(T_s)$ between 50 ^{o}C and 180 ^{o}C. The result is

$$F(T_s) = E_o + E_1 T_s + E_2 T_s^2 \qquad (A.3)$$

Where $E_o = 1.062806$

$E_1 = -2.794375 \times 10^{-3}$

$E_2 = 5.144126 \times 10^{-6}$

The constant of sensitivity (C_s) is a calibration constant given by the manufacturer at 21 ^{o}C (70 ^{o}F). The value of C_s for each heat flux sensor is listed in Table A.1.

Table A.1 Heat flux sensor sensitivity constant

Probe No.	#1	#2	#3
Radiation	0.17	0.20	0.18
Total	0.198	0.206	0.207

Appendix B Error Estimation

B.1 Total Heat Flux Gauge

Three sources of error, as previously identified by George (66), were presented in the total heat flux measurements

(a) error due to heat conduction along the stainless steel shim surface.

(b) error caused by nonuniform surface temperature in the bubble contact region.

(c) calibration and data collection RSS (Root-Sum-Square) error.

The first two are inherent errors of the gauges. George (66) analyzed these two errors. The temperature drop across the high thermal conductivity thin shim was found to be less than 1.8 K at T_w = 478 K. By neglecting the temperature difference, a two-dimensional steady state heat conduction analysis was performed to assess the ratio of heat flux transmitted to the sensor to that absorbed at the upper surface of the shim. It was found that about 2% of the heat flux absorbed at the shim's upper surface was not conducted to the sensor's active area.

A laminar thermal boundary layer analysis was conducted to investigate the effect of (b) on the performance of the total heat flux gauge. Note that this analysis applies only when the gauge is covered by gas bubbles, i.e. heat is transferred by pure gas convection. A reduction of about 4%

in the total heat flux measurement was found using the data of bubble contact fraction suggested by Catipovic (5,104), equation (1.5).

RSS Random Error

The errors in (c), which are of primary concern in terms of error estimation, are caused by operations in calibration and in data collection. The local total heat transfer coefficient (h_t) is calculated from

$$h_t = \frac{Q_t}{T_f - T_w} = \frac{C_c\ V_d}{T_f - T_w} \qquad \text{(B.1)}$$

where

C_c = heat flux sensor calibration constant [= $F(T_s)/C_s$]

V_d = detected thermopile voltage

The Root-Sum-Square (RSS) random error for calibration and data collection is given by Doebelin (55) as:

$$\left(\frac{\Delta h_t}{h_t}\right)_{ran} = \pm \left[\left(\frac{\Delta C_c}{C_c}\right)^2 + \left(\frac{\Delta V_d}{V_d}\right)^2 + \frac{(\Delta T_f)^2+(\Delta T_w)^2}{(T_f-T_w)^2}\right]^{1/2} \qquad \text{(B.2)}$$

RSS random error is then calculated using the uncertainty in each quantity based on the manufacturer's specifications and the author's operating experience. The maximum possible random error for the experiments was found to be

$$\left(\frac{\Delta h_t}{h_t}\right)_{ran} = \pm \left[(0.05)^2 + (0.05)^2 + \frac{(12)^2 + (4)^2}{(812 - 420)^2}\right]^{1/2}$$

$$= \pm \left[(0.05)^2 + (0.05)^2 + (0.041)^2\right]^{1/2}$$

$$\simeq \pm 0.08$$

Overall Error

The inherent errors in (a) and (b) are next added to the random error to obtain the overall error

$$\left(\frac{\Delta h_t}{h_t}\right)_{overall} = (+0.08, -0.08) + (0, -0.02) + (0, -0.04)$$

$$= (+0.08, -0.14)$$

It is concluded that the values of local total heat transfer coefficients reported in this study are within the range of (+0.08, -0.14) of actual values.

B.2 Radiation Detector

There are two inherent errors in the radiation detector itself, as described in section 2.2.3. The worst, ± 2.5% variation in radiation heat transfer measurements, was estimated due to the possibility of a nonuniform heat flux. An overestimation of 1% was found due to conduction error associated with the silicon window.

RSS Random Error

The black-tube local radiative heat transfer coefficient (h_{rb}) is calculated from

$$h_{rb} = \frac{Q_{rb}}{T_f - T_w} = \frac{C_d\, Q_d}{T_f - T_w} = \frac{C_d\, C_c\, V_d}{T_f - T_w} \qquad (B.3)$$

where

C_d = radiation detector calibration constant

C_c = heat flux sensor calibration constant

V_d = detected thermopile voltage

Note that an extra calibration constant (C_d), which is caused by the locally conducted calibration for the radiative detector, is involved in the calculation of the RSS random errors. The RSS random error becomes

$$\left(\frac{\Delta h_{rb}}{h_{rb}}\right)_{ran} = \pm \left[\left(\frac{\Delta C_d}{C_d}\right)^2 + \left(\frac{\Delta C_c}{C_c}\right)^2 + \left(\frac{\Delta V_d}{V_d}\right)^2 + \left(\frac{\Delta T_f^{\,2} + \Delta T_w^{\,2}}{(T_f - T_w)^2}\right)\right]^{1/2} \qquad (B.2)$$

Again, the maximum possible random error is calculated employing the uncertainties in each term.

$$\left(\frac{\Delta h_{rb}}{h_{rb}}\right)_{ran} = \pm \left[(0.05)^2 + (0.05)^2 + (0.05)^2 + \frac{(12)^2 + (2)^2}{(812 - 368)^2}\right]^{1/2}$$

$$= \pm \left[(0.05)^2 + (0.05)^2 + (0.05)^2 + (0.033)^2\right]^{1/2}$$

$$\simeq \pm 0.09$$

Overall Error

The estimation of overall error in local radiative heat transfer coefficient values reported in this study is obtained by adding all of these errors together

$$\left(\frac{\Delta h_{rb}}{h_{rb}}\right)_{overall} = (+0.09, -0.09) + (+0.025, -0.025) + (+0.01, 0)$$

$$= (+0.125, -0.115)$$

Appendix C. Tabulated Data

Experimental results for all test conditions are presented in Tables C.1 through C.10, which list the time-averaged local radiative (h_{rb}) and total (h_t) heat transfer coefficients at different locations (α = 0^o, 45^o, 90^o, 135^o,and 180^o measured from the lower stagnation point of the tube) and superficial velocities (U_o). Also listed are the spatial-averaged radiative values ($\bar{h}_{rb}$), total values ($\bar{h}_t$), and radiation contribution (f). Note that the data in Table C.6 and C.9 are adapted from Alavizadeh (9).

Data for the experimental verification conducted for the three window materials are listed in Tables C.11 and C.12 in the form of local radiative heat transfer coefficients (h_{rb}) at two locations (α = 0^o and 90^o) for two particle sizes (2.14 mm and 3.23 mm) and bed temperatures (900 K and 1080 K).

Table C.1

Results for D_p = 2.14 mm and T_f = 812 K (Tube Array)

	U_o	2.84	2.73	2.63	2.51	2.38	2.24	2.09
α = 0	h_{rb}	26.5	26.3	25.8	25.7	25.2	24.9	24.7
	h_t	178	177	179	178	181	180	189
α = 45	h_{rb}	25.3	25.1	25.2	25.0	25.2	24.9	24.7
	h_t	165	168	167	170	168	173	176
α = 90	h_{rb}	23.4	23.2	22.8	22.5	22.1	21.9	21.4
	h_t	175	177	173	174	173	171	178
α = 135	h_{rb}	20.7	20.4	19.9	19.6	18.7	18.4	18.0
	h_t	182	188	188	190	185	188	186
α = 180	h_{rb}	19.5	18.2	17.5	16.5	16.2	15.7	14.8
	h_t	203	199	196	194	189	180	180
Spatial Average	$\bar{h}_{rb}$	23.1	22.8	22.4	22.0	21.7	21.4	21.0
	$\bar{h}_t$	177	180	179	180	178	178	181
	f	13.2	12.8	12.7	12.5	12.4	12.3	11.8
	U_o	1.93	1.84	1.74	1.64	1.54	1.43	
α = 0	h_{rb}	24.6	24.7	24.3	23.9	22.1	19.5	
	h_t	186	182	183	186	181	168	
α = 45	h_{rb}	24.3	24.2	23.8	23.2	20.8	16.8	
	h_t	176	178	181	177	173	143	
α = 90	h_{rb}	21.1	21.0	20.8	20.3	18.8	13.4	
	h_t	172	173	170	168	141	123	
α = 135	h_{rb}	17.4	16.6	16.2	12.1	6.0	2.1	
	h_t	178	173	162	149	113	53	
α = 180	h_{rb}	13.6	11.6	9.4	3.5	.2	.0	
	h_t	168	156	133	101	33	15	
Spatial Average	$\bar{h}_{rb}$	20.5	20.0	19.1	17.4	14.2	10.5	
	$\bar{h}_t$	176	173	168	159	132	103	
	f	11.8	11.8	11.6	11.2	11.0	10.5	

U_{mf} = 1.60 m/sec f_{ave} = 12.2

Table C.2

Results for D_p = 2.14 mm and T_f = 925 K (Tube Array)

	U_o	3.26	3.02	2.74	2.49	2.31	2.15
α = 0	h_{rb}	32.4	32.1	32.5	32.2	32.4	32.8
	h_t	186	191	189	187	191	193
α = 45	h_{rb}	31.0	30.8	30.2	30.5	30.4	30.6
	h_t	175	176	180	184	181	184
α = 90	h_{rb}	28.7	28.1	28.3	27.8	27.7	27.1
	h_t	172	173	180	178	179	180
α = 135	h_{rb}	26.9	26.5	26.0	25.7	25.0	24.8
	h_t	188	189	195	204	214	216
α = 180	h_{rb}	25.6	25.0	24.9	24.0	23.2	22.1
	h_t	218	212	206	199	196	190
Spatial Average	$\bar{h}_{rb}$	28.9	28.5	28.3	28.0	27.7	27.5
	$\bar{h}_t$	184	185	188	190	192	193
	f	14.9	14.8	14.5	14.4	14.2	13.5
	U_o	1.99	1.87	1.74	1.66	1.58	1.50
α = 0	h_{rb}	33.0	32.5	31.7	31.0	29.5	25.1
	h_t	192	186	188	185	186	174
α = 45	h_{rb}	30.1	29.8	29.3	27.7	26.0	19.9
	h_t	182	188	191	185	175	153
α = 90	h_{rb}	27.0	26.7	25.4	23.7	20.0	14.5
	h_t	177	175	172	169	156	136
α = 135	h_{rb}	24.3	24.1	22.5	17.2	9.6	3.2
	h_t	208	190	172	154	121	60
α = 180	h_{rb}	20.0	17.4	13.3	7.7	3.1	.5
	h_t	188	172	150	117	50	27
Spatial Average	$\bar{h}_{rb}$	27.0	26.4	25.1	22.6	18.0	12.6
	$\bar{h}_t$	189	183	176	165	143	112
	f	13.7	13.8	13.8	13.0	12.1	10.9

U_{mf} = 1.64 m/sec f_{ave} = 14.1

Table C.3

Results for D_p = 2.14 mm and T_f = 1000 K (Tube Array)

	U_o	3.32	3.16	2.99	2.81	2.62	2.41
α = 0	h_{rb}	35.8	35.6	35.9	35.1	36.2	35.3
	h_t	190	191	193	193	196	198
α = 45	h_{rb}	34.1	33.3	33.5	33.2	33.5	32.5
	h_t	176	177	182	181	184	186
α = 90	h_{rb}	31.5	31.3	30.9	29.5	28.3	28.0
	h_t	171	167	175	181	183	189
α = 135	h_{rb}	29.1	28.8	28.0	26.9	26.7	26.2
	h_t	192	194	199	202	208	218
α = 180	h_{rb}	27.6	26.8	26.4	25.1	24.6	24.1
	h_t	223	215	213	207	205	201
Spatial Average	$\bar{h}_{rb}$	31.6	31.1	30.9	29.8	29.7	29.1
	$\bar{h}_t$	186	185	190	191	194	198
	f	16.4	16.1	15.7	15.1	14.8	14.4
	U_o	2.17	2.04	1.89	1.75	1.66	1.59
α = 0	h_{rb}	35.0	34.5	34.8	34.7	33.1	28.3
	h_t	201	199	193	191	194	187
α = 45	h_{rb}	31.6	30.8	29.7	29.2	27.1	20.8
	h_t	193	192	195	185	181	162
α = 90	h_{rb}	27.8	27.9	27.1	25.3	21.6	16.1
	h_t	171	167	175	181	183	189
α = 135	h_{rb}	25.5	25.4	25.0	21.1	14.5	4.1
	h_t	221	219	195	175	149	73
α = 180	h_{rb}	22.6	22.1	18.9	13.3	8.5	1.1
	h_t	196	189	179	155	81	42
Spatial Average	$\bar{h}_{rb}$	28.4	28.1	27.2	24.9	21.0	13.9
	$\bar{h}_t$	200	196	189	178	159	122
	f	14.3	13.9	13.7	13.4	13.0	11.4

U_{mf} = 1.73 m/sec f_{ave} = 14.8

Table C.4

Results for D_p = 3.23 mm and T_f = 812 K (Tube Array)

	U_o	2.83	2.78	2.74	2.68	2.63	2.57
α = 0	h_{rb}	24.9	24.4	24.5	24.8	24.5	24.4
	h_t	169	173	175	178	178	184
α = 45	h_{rb}	23.3	23.2	23.1	22.5	23.2	22.1
	h_t	164	169	169	170	166	167
α = 90	h_{rb}	21.4	21.5	21.6	20.8	21.1	20.9
	h_t	164	166	165	166	163	163
α = 135	h_{rb}	20.4	19.5	19.3	18.9	18.1	17.6
	h_t	183	189	192	195	188	181
α = 180	h_{rb}	18.2	18.0	17.3	16.5	15.9	15.1
	h_t	193	190	186	185	179	171
Spatial Average	$\bar{h}_{rb}$	21.7	21.4	21.2	20.7	20.6	20.1
	$\bar{h}_t$	174	176	177	178	174	172
	f	12.7	12.4	12.2	11.9	12.0	12.0
	U_o	2.51	2.45	2.39	2.32	2.25	2.17
α = 0	h_{rb}	25.1	24.3	24.5	23.6	22.7	19.1
	h_t	185	184	185	184	191	182
α = 45	h_{rb}	23.3	22.9	22.8	22.1	19.2	15.4
	h_t	168	174	175	169	164	140
α = 90	h_{rb}	20.5	20.0	19.4	18.6	16.6	9.7
	h_t	167	168	169	161	137	116
α = 135	h_{rb}	16.3	15.7	15.0	13.5	5.5	2.2
	h_t	173	165	150	140	104	60
α = 180	h_{rb}	14.2	13.9	9.1	3.1	.8	.1
	h_t	163	148	102	56	18	14
Spatial Average	$\bar{h}_{rb}$	19.9	19.4	18.5	16.9	13.4	9.4
	$\bar{h}_t$	171	167	159	148	128	104
	f	11.9	11.9	11.9	11.7	10.8	9.4

U_{mf} = 2.30 m/sec f_{ave} = 12.0

Table C.5

Results for D_p = 3.23 mm and T_f = 925 K (Tube Array)

	U_o	3.26	3.15	3.02	2.88	2.78	2.68
α = 0	h_{rb}	28.8	28.5	29.1	29.0	29.6	29.1
	h_t	182	178	180	185	186	189
α = 45	h_{rb}	28.1	27.8	27.8	28.9	28.3	27.9
	h_t	170	171	174	171	172	174
α = 90	h_{rb}	26.9	26.7	26.3	26.5	26.4	25.7
	h_t	166	169	166	167	170	168
α = 135	h_{rb}	25.0	24.5	24.1	23.1	21.9	21.4
	h_t	190	193	188	191	198	204
α = 180	h_{rb}	23.8	23.1	22.3	21.7	19.5	17.9
	h_t	201	196	189	195	192	183
Spatial Average	$\bar{h}_{rb}$	26.6	26.2	26.0	26.1	25.3	24.6
	$\bar{h}_t$	179	180	178	180	182	183
	f	14.5	14.3	14.4	14.1	13.6	13.5
	U_o	2.59	2.51	2.43	2.35	2.27	2.20
α = 0	h_{rb}	28.8	29.0	28.7	28.3	27.5	21.6
	h_t	190	187	184	188	195	185
α = 45	h_{rb}	28.0	28.2	27.8	26.8	23.4	17.1
	h_t	174	175	178	170	169	150
α = 90	h_{rb}	25.9	25.3	24.6	23.1	19.7	12.1
	h_t	170	173	171	163	149	116
α = 135	h_{rb}	20.9	20.7	19.1	15.6	9.4	4.1
	h_t	199	187	170	151	103	61
α = 180	h_{rb}	17.6	14.3	11.3	6.0	.6	.5
	h_t	171	152	121	76	27	20
Spatial Average	$\bar{h}_{rb}$	24.5	24.0	22.9	20.7	16.2	11.3
	$\bar{h}_t$	181	176	168	154	133	107
	f	13.3	13.5	13.6	13.2	12.0	10.6

U_{mf} = 2.32 m/sec f_{ave} = 13.8

Table C.6

Results for D_p = 2.14 mm and T_f = 812 K (Single Tube)

	U_o	2.77	2.68	2.58	2.46	2.35	2.19	2.07
α = 0	h_{rb}	27.5	26.8	26.6	26.3	26.0	25.9	25.4
	h_t	169	166	175	174	174	177	175
α = 45	h_{rb}	27.2	26.9	26.9	26.1	26.0	25.5	25.8
	h_t	176	182	185	190	189	186	190
α = 90	h_{rb}	24.8	24.7	24.4	24.2	24.1	24.1	23.7
	h_t	188	179	189	193	182	188	183
α = 135	h_{rb}	23.6	23.3	22.9	22.9	23.0	22.3	21.2
	h_t	186	183	190	177	177	182	190
α = 180	h_{rb}	21.4	20.1	20.3	19.8	19.3	18.1	18.4
	h_t	201	204	205	204	205	206	207
Spatial Average	$\bar{h}_{rb}$	25.0	24.6	24.4	24.1	23.9	23.5	23.1
	$\bar{h}_t$	184	182	189	187	184	187	189
	f	14.2	14.2	13.5	13.5	13.6	13.3	12.8
	U_o	1.96	1.85	1.75	1.67	1.57	1.47	
α = 0	h_{rb}	25.6	25.1	25.0	25.3	25.4	21.8	
	h_t	173	173	173	174	177	173	
α = 45	h_{rb}	25.3	25.2	25.4	25.5	26.5	18.6	
	h_t	185	187	191	178	178	143	
α = 90	h_{rb}	24.1	23.4	23.5	24.1	24.4	18.5	
	h_t	184	194	194	184	173	144	
α = 135	h_{rb}	19.9	19.9	19.5	16.4	9.8	3.3	
	h_t	194	197	196	182	135	69	
α = 180	h_{rb}	16.4	13.2	8.9	5.0	.7	0	
	h_t	207	186	156	122	76	19	
Spatial Average	$\bar{h}_{rb}$	22.6	21.9	21.3	20.3	18.4	12.8	
	$\bar{h}_t$	188	189	186	173	153	113	
	f	12.7	12.3	11.9	12.2	12.4	11.5	

U_{mf} = 1.62 m/sec f_{ave} = 13.1

Table C.7

Results for D_p = 2.14 mm and T_f = 925 K (Single Tube)

	U_o	3.25	3.01	2.73	2.48	2.30	2.15
α = 0	h_{rb}	35.1	35.3	35.8	35.5	35.3	36.0
	h_t	179	183	185	191	183	185
α = 45	h_{rb}	35.5	35.0	35.7	36.4	35.4	36.4
	h_t	183	192	191	197	201	198
α = 90	h_{rb}	34.3	34.2	33.8	34.7	34.1	33.6
	h_t	194	203	209	211	215	219
α = 135	h_{rb}	32.6	31.9	31.4	31.2	30.8	29.9
	h_t	202	200	201	209	213	215
α = 180	h_{rb}	28.3	27.9	26.5	25.0	23.8	21.3
	h_t	193	189	185	191	193	189
Spatial Average	$\bar{h}_{rb}$	33.5	33.2	33.0	33.0	32.5	32.1
	$\bar{h}_t$	191	195	197	202	204	205
	f	17.1	16.6	16.3	16.0	15.8	15.5
	U_o	2.01	1.88	1.77	1.68	1.59	1.51
α = 0	h_{rb}	36.3	35.8	34.7	35.1	33.4	31.9
	h_t	180	183	181	177	175	173
α = 45	h_{rb}	36.6	36.2	35.5	35.9	33.5	29.2
	h_t	194	189	187	185	179	165
α = 90	h_{rb}	33.4	33.0	32.9	32.1	28.1	22.0
	h_t	216	214	209	201	188	157
α = 135	h_{rb}	29.5	29.3	28.5	24.3	17.5	5.4
	h_t	210	205	195	184	141	77
α = 180	h_{rb}	19.8	18.6	16.4	13.1	8.6	3.1
	h_t	187	184	171	141	79	37
Spatial Average	$\bar{h}_{rb}$	31.9	31.5	30.6	29.1	25.0	18.5
	$\bar{h}_t$	201	198	192	182	159	126
	f	15.7	15.8	16.0	16.1	15.7	14.7

U_{mf} = 1.65 m/sec f_{ave} = 16.1

Table C.8

Results for D_p = 2.14 mm and T_f = 1000 K (Single Tube)

	U_o	3.30	3.15	2.98	2.79	2.60	2.38
α = 0	h_{rb}	41.3	40.9	41.9	42.1	41.8	41.5
	h_t	185	183	180	185	189	188
α = 45	h_{rb}	41.7	41.6	42.1	42.0	42.3	41.6
	h_t	182	189	185	194	198	197
α = 90	h_{rb}	40.5	39.2	40.6	40.0	40.4	40.1
	h_t	196	202	209	210	216	218
α = 135	h_{rb}	38.8	38.0	37.8	37.7	37.1	36.4
	h_t	204	212	216	217	222	230
α = 180	h_{rb}	34.4	33.6	31.4	29.9	28.9	28.6
	h_t	200	198	208	213	212	211
Spatial Average	$\bar{h}_{rb}$	39.7	39.0	39.3	38.9	38.8	38.3
	$\bar{h}_t$	194	198	201	205	209	211
	f	19.2	18.8	18.6	18.3	18.0	17.6
	U_o	2.18	2.02	1.87	1.74	1.65	1.57
α = 0	h_{rb}	41.9	40.8	41.2	40.3	39.5	38.1
	h_t	195	192	188	183	184	179
α = 45	h_{rb}	41.1	41.3	41.5	41.2	40.1	33.2
	h_t	197	195	194	192	185	173
α = 90	h_{rb}	39.9	39.4	38.3	37.9	32.5	26.3
	h_t	224	221	218	212	203	165
α = 135	h_{rb}	35.6	35.1	33.9	31.1	22.9	7.7
	h_t	240	256	233	201	176	104
α = 180	h_{rb}	27.4	26.1	23.5	19.2	12.5	4.5
	h_t	205	201	193	159	104	62
Spatial Average	$\bar{h}_{rb}$	37.8	37.3	36.6	35.0	30.4	22.1
	$\bar{h}_t$	215	217	209	194	177	141
	f	17.4	17.2	17.3	17.4	16.5	15.1

U_{mf} = 1.71 m/sec f_{ave} = 18.0

Table C.9

Results for D_p = 3.23 mm and T_f = 812 K (Single Tube)

	U_o	2.62	2.52	2.45	2.38	2.33
α = 0	h_{rb}	25.0	24.8	25.2	25.2	25.1
	h_t	168	172	171	174	179
α = 45	h_{rb}	25.6	25.2	25.9	25.3	25.8
	h_t	182	179	176	175	175
α = 90	h_{rb}	24.7	24.3	24.5	24.4	24.5
	h_t	196	196	195	195	192
α = 135	h_{rb}	22.9	22.1	21.9	21.3	20.7
	h_t	193	198	196	196	190
α = 180	h_{rb}	21.1	17.6	16.2	13.8	8.3
	h_t	160	148	134	119	78
Spatial Average	$\bar{h}_{rb}$	24.0	23.2	23.2	22.6	21.9
	$\bar{h}_t$	184	183	180	178	171
	f	13.8	13.4	13.5	13.4	13.5
	U_o	2.28	2.20	2.16	2.11	
α = 0	h_{rb}	22.9	23.6	23.2	23.3	
	h_t	191	222	228	235	
α = 45	h_{rb}	25.5	23.8	24.0	23.6	
	h_t	163	150	145	150	
α = 90	h_{rb}	23.7	19.3	19.6	18.2	
	h_t	160	149	148	137	
α = 135	h_{rb}	13.5	9.6	8.6	8.2	
	h_t	145	133	126	111	
α = 180	h_{rb}	.3	.0	.3	.1	
	h_t	23	20	19	19	
Spatial Average	$\bar{h}_{rb}$	18.6	16.1	16.0	15.4	
	$\bar{h}_t$	144	138	136	131	
	f	13.2	12.1	12.1	12.1	

U_{mf} = 2.31 m/sec f_{ave} = 13.5

Table C.10

Results for D_p = 3.23 mm and T_f = 925 K (Single Tube)

	U_o	3.28	3.17	3.05	2.92	2.80	2.70
α = 0	h_{rb}	34.2	34.0	34.1	34.0	34.3	34.5
	h_t	174	172	175	180	181	180
α = 45	h_{rb}	34.3	34.1	33.8	33.6	34.3	34.1
	h_t	188	191	195	198	196	199
α = 90	h_{rb}	34.1	33.5	33.0	32.7	32.4	32.7
	h_t	195	200	205	208	204	210
α = 135	h_{rb}	32.4	31.9	31.7	31.3	30.6	30.2
	h_t	191	195	199	201	195	197
α = 180	h_{rb}	29.9	29.1	28.4	27.7	26.9	25.8
	h_t	178	174	169	164	166	167
Spatial Average	$\bar{h}_{rb}$	33.1	32.8	32.4	32.0	32.0	31.8
	$\bar{h}_t$	188	190	193	195	192	195
	f	17.6	17.3	17.2	16.9	17.1	16.9
	U_o	2.61	2.53	2.45	2.37	2.29	2.21
α = 0	h_{rb}	34.3	34.4	33.8	33.1	32.9	31.7
	h_t	183	181	183	184	182	177
α = 45	h_{rb}	34.3	34.6	34.7	34.5	33.5	30.4
	h_t	200	195	191	189	184	171
α = 90	h_{rb}	32.4	32.9	32.5	31.4	28.4	21.1
	h_t	209	210	205	191	181	131
α = 135	h_{rb}	30.0	29.3	27.9	24.2	17.1	8.0
	h_t	203	200	197	181	121	75
α = 180	h_{rb}	24.1	22.3	19.3	13.5	1.3	.8
	h_t	159	151	137	97	31	23
Spatial Average	$\bar{h}_{rb}$	31.5	31.3	30.4	28.4	24.0	19.1
	$\bar{h}_t$	196	193	189	174	148	119
	f	16.4	16.7	16.5	16.6	16.5	16.3

U_{mf} = 2.33 m/sec f_{ave} = 16.9

Table C.11

Local radiative heat transfer coefficient (h_{rb}) for D_p = 2.14 mm (Single Tube)

		T_f = 900 K			U_{mf} = 1.67 m/sec			
	U_o	.96	1.17	1.34	1.49	1.63	1.75	1.86
α = 0	Si*	20.6	21.9	23.0	23.8	25.9	26.4	26.8
	Sa#	21.7	22.3	24.6	24.4	28.3	27.8	28.1
	Qz+	44.2	48.1	45.9	47.8	51.3	47.2	46.5
α = 90	Si	7.9	12.1	16.2	18.9	20.7	24.9	26.0
	Sa	8.5	13.4	15.9	19.5	21.5	26.2	27.8
	Qz	20.8	27.6	29.2	39.1	49.8	45.8	47.4
	U_o	1.97	2.06	2.24	2.41	2.55	2.68	2.80
α = 0	Si	27.6	28.9	29.8	30.6	30.9	31.1	31.2
	Sa	29.2	29.8	32.7	31.6	33.1	34.5	33.8
	Qz	51.8	52.3	50.6	53.1	52.5	50.7	52.6
α = 90	Si	26.6	26.8	26.6	27.0	27.2	27.5	27.6
	Sa	28.8	27.6	29.4	28.2	29.5	28.9	29.9
	Qz	46.3	45.9	47.8	46.9	50.5	47.2	50.2
		T_f = 1080 K			U_{mf} = 1.67 m/sec			
	U_o	1.15	1.40	1.61	1.80	1.95	2.10	2.24
α = 0	Si	31.2	36.8	40.9	44.7	47.1	47.8	48.1
	Sa	32.5	38.9	44.1	46.2	49.8	51.1	50.4
	Qz	59.4	68.5	65.6	75.1	70.1	73.1	65.2
α = 90	Si	11.4	18.6	25.7	37.8	45.1	45.9	46.3
	Sa	12.1	18.9	27.4	41.2	45.9	48.4	49.8
	Qz	24.5	36.7	55.6	69.4	65.3	71.5	67.5
	U_o	2.37	2.48	2.70	2.89	3.07	3.22	3.36
α = 0	Si	48.3	48.5	48.2	48.7	47.7	47.1	47.0
	Sa	50.8	51.4	49.9	50.6	52.1	48.8	50.0
	Qz	68.3	68.5	72.4	69.0	64.0	62.8	69.5
α = 90	Si	46.7	46.9	47.6	47.3	47.4	46.8	46.2
	Sa	50.3	47.9	50.8	50.6	51.3	49.4	50.1
	Qz	69.0	68.2	71.3	74.1	72.5	69.4	68.6

* Stands for silicon
\# Stands for sapphire
\+ Stands for quartz

Table C.12

Local radiative heat transfer coefficient (h_{rb}) for D_p = 3.23 mm (Single Tube)

		T_f = 900 K			U_{mf} = 2.48 m/sec			
	U_o	1.20	1.38	1.53	1.67	1.80	1.92	2.03
α = 0	Si*	18.1	18.8	19.9	20.3	20.8	21.4	21.9
	Sa#	19.3	18.1	20.5	22.7	21.3	22.6	24.3
	Qz+	41.2	40.7	43.2	42.8	45.3	46.9	45.4
α = 90	Si	6.5	7.5	10.4	11.2	12.8	14.1	15.9
	Sa	6.9	8.6	9.8	11.6	13.5	14.3	16.9
	Qz	22.3	26.4	25.2	29.7	32.6	37.4	39.8
	U_o	2.11	2.29	2.45	2.59	2.66	2.73	2.85
α = 0	Si	22.2	22.8	23.5	23.8	24.7	25.7	27.0
	Sa	23.2	24.6	25.2	25.4	25.6	26.3	27.4
	Qz	48.8	44.8	44.4	47.1	48.6	48.3	50.2
α = 90	Si	18.2	32.7	22.1	22.9	23.0	24.2	25.3
	Sa	18.7	23.0	23.4	22.9	24.2	25.1	26.6
	Qz	41.5	39.9	45.7	44.4	47.5	46.9	48.7
		T_f = 1080 K			U_{mf} = 2.25 m/sec			
	U_o	1.19	1.45	1.67	1.86	2.03	2.19	2.32
α = 0	Si	27.2	29.6	31.8	33.0	35.1	38.9	42.5
	Sa	29.8	33.6	33.7	34.6	37.6	40.2	44.3
	Qz	51.1	49.3	60.2	64.4	65.5	71.2	69.4
α = 90	Si	7.3	7.9	10.8	13.2	19.7	24.8	32.8
	Sa	8.2	8.1	10.5	13.9	18.8	25.6	32.7
	Qz	20.7	29.6	28.1	36.7	47.3	59.8	57.1
	U_o	2.57	2.79	2.99	3.17	3.33	3.48	
α = 0	Si	46.2	47.0	49.3	50.4	49.7	49.1	
	Sa	46.9	48.4	50.6	53.0	52.5	51.8	
	Qz	67.9	68.6	69.8	73.4	71.2	71.0	
α = 90	Si	44.3	45.0	45.9	46.5	45.8	45.2	
	Sa	46.0	49.0	48.1	49.3	48.6	48.1	
	Qz	62.4	69.5	67.4	70.2	72.2	70.1	

* Stands for silicon
\# Stands for sapphire
\+ Stands for quartz